Fall 2020

Improved attenuation and crosstalk modeling techniques for high-speed channels

Shaohui Yong

IMPROVED ATTENUATION AND CROSSTALK MODELING TECHNIQUES FOR

HIGH-SPEED CHANNELS

by

SHAOHUI YONG

A DISSERTATION

Presented to the Graduate Faculty of the

MISSOURI UNIVERSITY OF SCIENCE AND TECHNOLOGY

In Partial Fulfillment of the Requirements for the Degree

DOCTOR OF PHILOSOPHY

in

ELECTRICAL ENGINEERING

2020

Approved by:

Dr. DongHyun Kim, Advisor
Dr. Jun Fan, Co-Advisor
Dr. Victor Khilkevich
Dr. James Drewniak
Dr. Chulsoon Hwang
Dr. Xiaoning Ye

PUBLICATION DISSERTATION OPTION

This dissertation consists of the following three articles, formatted in the style used by the Missouri University of Science and Technology:

Paper I, found on pages 3–45, "Dielectric Loss Tangent Extraction Using Modal Measurements and 2-D Cross-sectional Analysis for Multilayer PCBs", has been published in *IEEE Transactions on Electromagnetic Compatibility*, 2020, vol. 62, no. 4, pp. 1278-1292, Aug 2020

Paper II, found on pages 46–67, "Resistance Modeling for Striplines with Different Surface Roughness on the Planes" has been published in the proceedings of *2020 IEEE International Symposium on Electromagnetic Compatibility & Signal/Power Integrity (EMCSI)*, Reno, NV, USA, 2020.

Paper III, found on pages 68–93, "Prepreg And Core Dielectric Permittivity Extraction for Fabricated Striplines' Far-end Crosstalk Modeling", is intended for submission to *IEEE Transactions on Electromagnetic Compatibility*.

ABSTRACT

As digital systems are moving in the direction of faster data transmission rate and higher density of circuits, the problem of the far-end crosstalk (FEXT) and frequency-dependent attenuation are becoming the major factors that limit signal integrity performance. This research is focusing on providing several more comprehensive and accurate modeling approaches for striplines on fabricated printed circuit board (PCB). By characterizing the dielectric permittivity of prepreg and core, dielectric loss tangent, and copper foil surface roughness using measurement data, a better agreement between the stripline model and measurement is achieved. First, a method is proposed to extract dielectric loss tangent using coupled striplines' measured S-parameters and cross-section geometry. By relating modal attenuation factors to the ratio between the differential and common mode per-unit-length resistances, the unknwon surface roughness contribution is eliminated and the contributions of dielectric and conductor loss are separated. In addition, an improved surface roughness modeling approach is proposed by analyzing the microscopical cross-sectional image of the stripline. By combining the characterized surface roughness information and the extracted dielectric properties, the modeled attenuation factor is match with the measurement data. At last, an approach is introduced to extract the dielectric permittivity of prepreg and core. Using known cross-sectional geometry and measured phase of the coupled stirplines under test, the capacitance components in prepreg and core are separated using 2D solver models. Using the stripline model with inhomogeneous dielectric material, more accurate FEXT modeling results are obtained.

ACKNOWLEDGMENTS

I would like to take this opportunity to express my sincere gratitude to Dr. Jun Fan, Dr. James Drewniak, Dr. David Pommerneke, Dr. Vcitor Khilkevich and Dr. DongHyun Kim for the valuable help in recent years. They put a lot of time and effort into my training, and I really appreciate their instructions, guidance and encouragement. They also offered me the amazing opportunities and paved my future professional career path.

I would like to thank Dr. Chulsoon Hwang and Dr. Daryl Beetner for broaden my research perspectives and teaching me great skills. I also would also like to thank to Dr. Xiaoning Ye for giving me insightful comments and and brilliant ideas for my research. I feel very grateful to the EMC Lab faculty members, students and MUELAN alumnus for the warm-hearted support.

Finally, I thank my parents, whose unconditional love made my PhD study possible.

This dissertation is based upon work supported partially by the National Science Foundation under Grant No. IIP-1916535, Intel Corporation, and Cisco Systems, Inc.

TABLE OF CONTENTS

LIST OF ILLUSTRATIONS

PAPER II

LIST OF TABLES

SECTION

1. INTRODUCTION

As data rate of high-speed channels are getting higher, the signal and power integrity performance of morden digital systems often relies on the dielectric material, copper foil surface roughness, and the noise coupling among channels [1-6].

Because of the uncertainty or inaccuracy of dielectric material after printed circuit boards (PCB) fabrication, sometimes engineers have to use conservative estimations and choose expensive high-performance materials to meet design specifications, which causes over-design and cost rise [7-10]. A new dielectric material property (permittivity ε_r, and loss tangent $\tan\delta$) extraction approach is proposed [11]. By relating modal attenuation factors to the ratio between the differential and common mode per-unit-length resistances, the unknown surface roughness contribution is eliminated and the contributions of dielectric and conductor loss are separated. This method can achieve better roughness immunity and extract $\tan\delta$ from the perspective of physics, without any *a priori* assumptions about the $\tan\delta$ behavior. The uncertainty of the extraction is also provided after some investigations on the de-embedding algorithms [12-14].

In terms of the attenuation due to lossy conductor, it has been quite evident that the skin-effect formulas ignoring foil surface roughness underestimate attenuation as frequency goes up to tens of gigahertz [15-18]. A more comprehensive surface roughness modeling approach is proposed by analyzing the scanning electron microscope (SEM) cross-sectional images of the transmission line. Also, a technique is developed to model the realistic stripline structures consisting of four rough planes with different surface roughness (the upper and lower sides of the traces, and the upper and lower reference planes).

As the size of electronic device getting smaller, there are plenty potential noise sources can degrade the performance of modern digital system [19-22]. The crosstalk noise among high-speed channels is one of the major factors that bottlenecks the signal integrity performance due to the increasing trace density on PCB. To avoid failure to meet the far-end crosstalk (FEXT) noise margin specifications, it is critical for engineers to characterize the FEXT on fabricated PCB. Recently, several FEXT models [23-25] for fabricated striplines were proposed, however the modeling of the inhomogenerity of stripline is not modeled very well. In one of the models a new concept called FEXT-due-to-lossy-conductors was proposed [26], which can be one of the major FEXT contributors in high-speed striplines. However, as far as the authors know, there has been no published approaches for the characterization of the FEXT due to inhomogeneous dielectric material in striplines. As the examples shown in later in this thesis, obvious discrepancy can be observed by comparing the measurement and modeled FEXT assuming homogeneous dielectric material [27-30]. An approach is proposed to extract the permittivity of prepreg and core using measured S-parameters and known cross-sectional geometry of coupled striplines. Improved modeling results will be presented by comparing measurements with modelling results obtained using the extracted dielectric parameters.

PAPER

I. DIELECTRIC LOSS TANGENT EXTRACTION USING MODAL MEASUREMENTS AND 2-D CROSS-SECTIONAL ANALYSIS FOR MULTILAYER PCBS

ABSTRACT

Frequency-dependent electrical properties of dielectric materials are one of the most important factors for high-speed signal integrity (SI) design. To accurately characterize material's dielectric loss tangent (tanδ) after multilayer printed circuit board (PCB) fabrication a novel method was proposed recently to extract tanδ using coupled striplines' measured S-parameters and cross-section geometry. By relating modal attenuation factors to the ratio between the differential and common mode per-unit-length resistances, the surface roughness contribution is eliminated and the contributions of dielectric and conductor loss are separated. Here, we specifically decided to avoid using any physical dielectric model in the extraction algorithm in order to eliminate a need for any a priori information about dielectric behavior. Further analysis and improvement of the tanδ extraction approach is presented in this paper. To evaluate the accuracy of the extraction, the impact of errors due to de-embedding, vector network analyzer (VNA) measurement, and 2D solver's calculation are taken into account by a statistical error model. A confidence interval of extracted tanδ is provided. To describe the frequency dependence of tanδ, a two-term Djordjevic model is proposed to fit the extracted tanδ curve, which guarantees causality and gives better agreement with measured insertion loss compared to the traditional Djordjevic model.

Keywords: Conductor surface roughness, confidence interval, de-embedding method, error analysis, fabricated printed circuit board (PCB), frequency-dependent dielectric behavior, stripline.

1. INTRODUCTION

Adequate wideband characterization of PCB dielectric substrates is critical in high-speed signal and power integrity design. Traditional approximations using frequency-independent dielectric constant (ε_r) and loss tangent (tanδ), may be applicable for low-speed transmission lines, but do not properly account for the extra attenuation caused by energy consumption due to dielectrics polarization at higher frequencies and cannot model phase-delay responses correctly, producing underestimated dielectric loss and non-causality. Nowadays, as serializer/deserializer (SerDes) channels having pulse rise time reduced to only several pico-seconds, availability of frequency-dependent dielectric material parameters up to 40+ GHz plays an important role in predicting signal degradation. Inaccurate frequency-dependence will cause significant uncertainty for modern high-speed PCB design, leading to failure to meet required specifications or costly overdesign.

A traditional dielectric material properties extraction method using a split post dielectric resonator (SPDR) [1-3] is widely adopted by material vendors to provide nominal ε_r and tanδ values at certain frequency points. A dielectric material sample of required size and shape should be provided for the resonator measurement. ε_r and tanδ are calculated using measured resonance frequency shift and decrease of the Q-factor.

However, the SPDR measurement is an inherently narrow-band method. To cover a certain frequency band, multiple SPDRs are needed. Also, the required dielectric sample cannot contain any metallization layers, which often requires the fabrication of dedicated samples with potentially different properties compared to the multilayer PCB fabrication process [4-6]. The "Root-Omega" transmission-line-based extraction method [7-9] was developed to overcome drawbacks of the SPDR method. It assumes that the frequency dependencies of conductor (α_C) and dielectric (α_D) attenuation factors obey different laws, approximated by power functions, such that they can be separated from the total attenuation (α_T) directly obtained from measured S-parameters. However as demonstrated in [10], "Root-Omega" method cannot separate conductor attenuation factor (α_C) influenced by unknown surface roughness very well. Relatively accurate results can only be achieved for very smooth copper surfaces. Besides that, the power functions adopted to fit attenuation factors do not take into account possible loss dispersion of the dielectric. In addition, the values of ε_r and $\tan\delta$ obtained by the SPDR or "Root-Omega" methods are routinely approximated by using a Djordjevic model [11] assuming PCB dielectrics with very low dispersion, which provides causality but may not be able to model extra insertion loss (S_{21}) above tens of gigahertz due to practically constant $\tan\delta$ in the frequency band of interest [11-13].

Recently, a new dielectric characterization method using physics-based principle to exclude the influence of foil surface roughness is proposed in [10]. It does not require any *a priori* assumptions about the $\tan\delta$ frequency-dependent behavior. As a follow-up work on the new method, this paper offers a more comprehensive analysis of the extraction procedure along with the error analysis.

This paper is arranged as follows. In Section 2, the core algorithm of the extraction method is introduced. Section 3 investigates the influence of potential inhomogeneity of the PCB dielectric on the extraction performance. In Section 4, analysis on the impact of errors due to de-embedding, VNA measurement and 2D solver on the extracted $\tan\delta$ accuracy is presented. The confidence interval of extracted $\tan\delta$ curve is calculated. Section 5 provides a discussion about the frequency behavior of $\tan\delta$. A two-term Djordjevic model is proposed to fit the extraction results within the confidence interval. Comparison between the proposed approach and a conventional one-term Djordjevic model is given.

2. LOSS TANGENT EXTRACTION METHODOLOGY

Before describing the extraction method, we would like to define the necessary parameters. Let us assume a three-conductor transmission line. One of the conductors is treated as a reference, and the nodal voltages ($\mathbf{V}$) are defined as the voltages in two remaining conductors relative to the reference. Similarly, the nodal currents ($\mathbf{I}$) are defined as the currents in the two conductors (the return currents are flowing in the reference conductor).

$$\mathbf{V} = \begin{bmatrix} v_1 \\ v_2 \end{bmatrix}.$$

$$\mathbf{I} = \begin{bmatrix} i_1 \\ i_2 \end{bmatrix}.$$

The nodal parameters ($\mathbf{V}$ and $\mathbf{I}$) can be related to the modal ones ($\mathbf{V}_m$ and $\boldsymbol{I}_m$) through the transformations [14] shown in (1).

As (3) shown, the nodal voltages and currents in the transmission lines are described by the telegrapher's equations [15]:

$$\begin{aligned} \mathbf{V} &= \mathbf{T}_v \begin{bmatrix} v_{m1} \\ v_{m2} \end{bmatrix} = \mathbf{T}_v \mathbf{V}_m \,, \\ \mathbf{I} &= \mathbf{T}_i \begin{bmatrix} i_{m1} \\ i_{m2} \end{bmatrix} = \mathbf{T}_i \mathbf{I}_m \,, \end{aligned} \tag{1}$$

where $\mathbf{T}_v$ and $\mathbf{T}_i$ are transformation matrices. If the matrices are defined as:

$$\begin{aligned} \mathbf{T}_v &= \begin{bmatrix} 1 & -0.5 \\ 1 & 0.5 \end{bmatrix}, \\ \mathbf{T}_i &= \begin{bmatrix} 0.5 & -1 \\ 0.5 & 1 \end{bmatrix}, \end{aligned} \tag{2}$$

the modal parameters will correspond to the common and differential modes:

$$\mathbf{V}_m = \begin{bmatrix} v_{cc} \\ v_{dd} \end{bmatrix} = \mathbf{T}_v^{-1} \mathbf{V} = \begin{bmatrix} 0.5(v_1 + v_2) \\ v_2 - v_1 \end{bmatrix},$$

$$\mathbf{I}_m = \begin{bmatrix} i_{cc} \\ i_{dd} \end{bmatrix} = \mathbf{T}_i^{-1} \mathbf{I} = \begin{bmatrix} i_1 + i_2 \\ 0.5(i_2 - i_1) \end{bmatrix}.$$

$$\begin{aligned} d\mathbf{V}/dz &= -\mathbf{Z} \cdot \mathbf{I} \,, \\ d\mathbf{I}/dz &= -\mathbf{Y} \cdot \mathbf{V} \,, \end{aligned} \tag{3}$$

where $\mathbf{Z} = \mathbf{R} + j\omega\mathbf{L}$ and $\mathbf{Y} = \mathbf{G} + j\omega\mathbf{C}$ are nodal PUL impedance and admittance matrices of the transmission line.

$$d\mathbf{V}_m/dz = -\mathbf{Z}_m \cdot \mathbf{I}_m \,, \tag{4}$$

$$d\mathbf{I}_m/dz = -\mathbf{Y}_m \cdot \mathbf{V}_m$$

$$d\mathbf{V}_m/dz = -\mathbf{Z}_m \cdot \mathbf{T}_i^{-1}\mathbf{I} \,, \tag{5}$$

$$d\mathbf{I}_m/dz = -\mathbf{Y}_m \cdot \mathbf{T}_v^{-1}\mathbf{V} \tag{6}$$

$$d\mathbf{V}/dz = -\mathbf{T}_v \, \mathbf{Z}_m \mathbf{T}_i^{-1}\mathbf{I} \,, \tag{7}$$

$$d\mathbf{I}/dz = -\mathbf{T}_i \, \mathbf{Y}_m \mathbf{T}_v^{-1}\mathbf{I} \,. \tag{8}$$

Equation (3) can be generalized for modal cases. By plugging (1) into (3), the equations for the modes can be written as (5) amd (6). Multiplying both sides of (5) by $\mathbf{T}_v$

and (6) by $\mathbf{T}_i$ gives (7) and (8). Finally, by comparing (3) with (7) and (8) the modal PUL matrices are obtained:

$$\begin{aligned}\mathbf{Z}_m &= \mathbf{T}_v^{-1}\mathbf{Z}\mathbf{T}_i\,,\\ \mathbf{Y}_m &= \mathbf{T}_i^{-1}\mathbf{Y}\mathbf{T}_v\,.\end{aligned} \tag{9}$$

It is easy to see that the transformation matrices defined as (2) diagonalize the impedance and admittance matrices (9) such that:

$$\begin{aligned}\mathbf{Z}_m &= \mathbf{R}_m + j\omega\mathbf{L}_m = \begin{bmatrix} Z_{cc} & 0 \\ 0 & Z_{dd}\end{bmatrix} = \begin{bmatrix} R_{cc} + j\omega L_{cc} & 0 \\ 0 & R_{dd} + j\omega L_{dd}\end{bmatrix},\\ \mathbf{Y}_m &= \mathbf{G}_m + j\omega\mathbf{C}_m = \begin{bmatrix} Y_{cc} & 0 \\ 0 & Y_{dd}\end{bmatrix} = \begin{bmatrix} G_{cc} + j\omega C_{cc} & 0 \\ 0 & G_{dd} + j\omega C_{dd}\end{bmatrix}.\end{aligned} \tag{10}$$

The transformation matrices (2) together with (9) will be used henceforth to convert the nodal PUL matrices to the modal ones (10). The propagation constant for each mode is related to the modal PUL parameters as:

$$\gamma_{cc,dd} = \sqrt{\left(R_{cc,dd} + j\omega L_{cc,dd}\right)\left(G_{cc,dd} + j\omega C_{cc,dd}\right)}\ . \tag{11}$$

The real part of the propagation constant, i.e. the modal attenuation factor can be approximately (but with high degree of accuracy for practical low-loss transmission lines with $R \ll \omega L$ and $G \ll \omega C$) calculated as [16]:

$$\alpha_{cc,dd} \approx 0.5\left(R_{cc,dd}\sqrt{C_{cc,dd}/L_{cc,dd}} + G_{cc,dd}\sqrt{L_{cc,dd}/C_{cc,dd}}\right). \tag{12}$$

Information about the dielectric loss in (12) is contained in the PUL conductance G (see below, Equation (24)), so the extraction of the dielectric loss from the attenuation factors (12) would require to determine all other parameters in the formula. The attenuation factors (α_{cc} or α_{dd}) of striplines can be relatively easily determined in the measurement, and the PUL capacitances and inductances can be calculated if the geometry of the stripline and the permittivity of the dielectric are known. However, it is very difficult to determine the PUL resistance R because it is affected by the surface roughness of the transmission line conductors.

Existing roughness models have limited accuracy and rely on numerous roughness parameters which are usually not known and need to be tuned. Thus, the per-unit-length (PUL) resistance of a transmission line (R) can never be calculated accurately. To exclude the impact of foil roughness on the loss tangent extraction accuracy, direct usage of the PUL R of the transmission line should be avoided. The new approach proposed here turns to use a pair of coupled traces allowing to relate the $\tan\delta$ to the ratio of modal PUL resistances (K), which is (as will be shown later) largely independent from foil roughness. Coefficient K is defined here as the ratio between differential and common mode PUL R:

$$K = R_{dd}/R_{cc}\,. \tag{13}$$

Let us analyze the parameter K. For translationally uniform weakly coupled striplines (i.e., in the case when the proximity effect [17-19] is negligible), the matrix $\mathbf{R}$ is given as Equation (14) according to [15]. Here, r_0 is the resistance of the ground planes, and r_1 is the resistances of traces (this assumes a symmetrical line). In this case, the modal resistance matrix calculated according to (9) is expressed using (14) and (15).

$$\mathbf{R} = \begin{bmatrix} R_{11} & R_{12} \\ R_{12} & R_{11} \end{bmatrix} = \begin{bmatrix} r_1 + r_0 & r_0 \\ r_0 & r_1 + r_0 \end{bmatrix}, \tag{14}$$

$$\mathbf{R}_m = \begin{bmatrix} r_0 + \frac{1}{2}r_1 & 0 \\ 0 & 2r_1 \end{bmatrix} = \begin{bmatrix} R_{cc} & 0 \\ 0 & R_{dd} \end{bmatrix}. \tag{15}$$

Let us assume that the resistances r_0 and r_1 correspond to perfectly smooth conductors. Therefore, the parameter K for a smooth transmission line can be calculated using (16). The effect of foil roughness on resistance is usually modeled by applying a correction coefficient to the PUL resistance [20-22]. The correction coefficients for the traces K_{Ht} and ground planes K_{Hg} can be added to (16) to obtain the value of K for a rough transmission line as (17).

$$K_{smooth} = R_{dd}/R_{cc} = 2r_1(r_0 + 0.5r_1)^{-1} . \tag{16}$$

$$K_{rough} = R_{dd}/R_{cc} = 2r_1 \cdot K_{Ht} \cdot (r_0 \cdot K_{Hg} + 0.5 \cdot r_1 \cdot K_{Ht})^{-1} . \tag{17}$$

It is obvious that when the roughness of trace and ground conductors is equal, i.e. when $K_{Ht} = K_{Hg}$, the correction coefficients in (17) are eliminated and $K_{smooth} = K_{rough}$. Therefore, the ratio K in this case (i.e. when all conductors have equal roughness) is independent of roughness.

It should be noted here that the roughness of traces and ground planes is not always equal. In that case, the ratio K can still be estimated using (17) with the correction coefficients calculated according to Huray (or other) model. However, in this study the tanδ extraction was performed on the PCBs with comparable roughness in ground and trace conductors. Feasibility of extracting tanδ in lines with different trace/ground plane roughness requires additional investigation.

The analysis above assumed no proximity effect in the transmission line. In strongly coupled lines, which are ultimately needed for the tanδ extraction (see below), the proximity effect cannot be neglected. A general formulation of the resistance matrix with proximity effect in the form similar to (13) is difficult, so to demonstrate the roughness independence of K, a numerical simulation was performed using Ansys Q2D. During the simulation the roughness of the conductors of the strongly coupled stripline was varied, and the value of K was calculated for each roughness value. As can be seen from Figure 1, the value of K changes very insignificantly when the foil roughness changes in a wide range – i.e. from a smooth (0.0 μm RMS roughness) to a relatively rough case (0.8 μm RMS roughness), and the condition $K_{smooth} = K_{rough}$ can still be used.

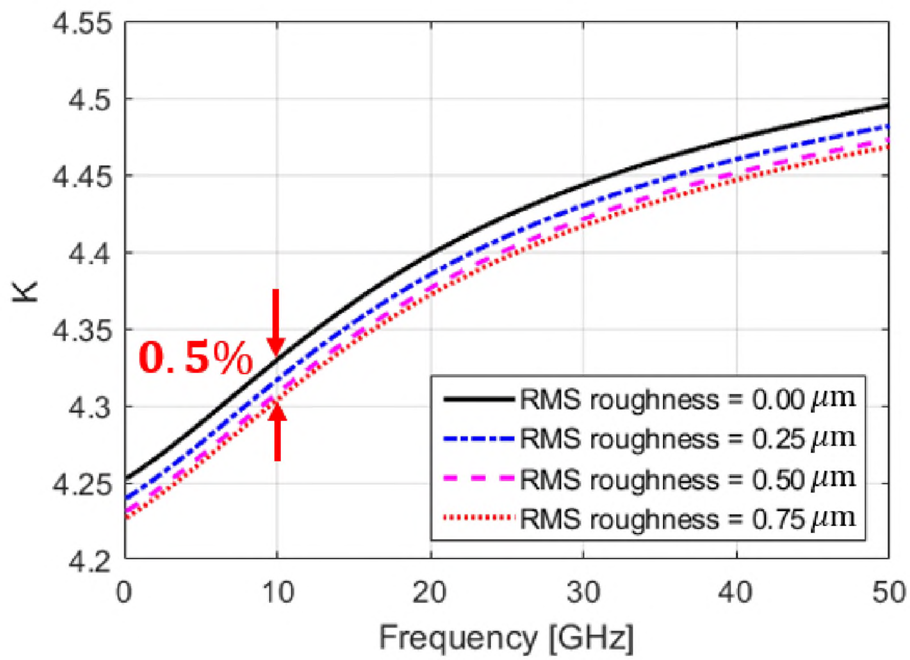

Figure 1. Resistance ratio K for coupled striplines with different conductor surface roughness. The curves are calculated by Ansys Q2D. The cross-section geometry of the coupled striplines is illustrated in Figure 3. The dielectric constant $\varepsilon_r = 3.4$.

The modal attenuation factors are related to the modal transmission coefficients:

$$\alpha_{cc,dd} = -\ln[|S_{cc21,dd21}|]/l, \tag{18}$$

where S_{cc21} and S_{dd21} are the de-embedded modal transmission coefficients (i.e. normalized to the modal characteristic impedances), and l is the length of the transmission line after de-embedding.

Any suitable de-embedding procedure can be used to obtain the modal transmission coefficients (for example a TRL calibration). In the presented implementation we used a variant of the 2x thru de-embedding technique known as 'Eigen-value de-embedding' [23-26]. The choice was made primarily because it is a precise de-embedding technique for translationally uniform transmission lines and uses minimal number of standards (just two lines of different length). The procedure is designed for single-ended lines; therefore, it is necessary to explained here how it can be applied to coupled striplines. To apply the de-embedding the VNA is calibrated first to remove all asymmetries between the ports, and hence additional mode conversion. Then the single-ended S-parameters ($\mathbf{S}'$) of the 4-port standards are measured and converted to the modal ones ($\mathbf{S}'_M$) by the following transformation:

$$\mathbf{S}'_M = \mathbf{M}\mathbf{S}'\mathbf{M}^{-1}, \tag{19}$$

where $\mathbf{M}$ is the transformation matrix (the prime symbols in the formula indicate raw, non-de-embedded S-parameters). To obtain common and differential S-parameters the transformation matrix is defined as [14] (the definition reflects the port numbering convention):

$$\mathbf{M} = 2^{-0.5} \cdot \begin{bmatrix} 1 & -1 & 0 & 0 \\ 0 & 0 & 1 & -1 \\ 1 & 1 & 0 & 0 \\ 0 & 0 & 1 & 1 \end{bmatrix}. \tag{20}$$

$$\mathbf{S}'_M = \begin{bmatrix} S'_{dd11} & S'_{dd12} & S'_{dc11} & S'_{dc12} \\ S'_{dd21} & S'_{dd22} & S'_{dc21} & S'_{dc22} \\ S'_{cd11} & S'_{cd12} & S'_{cc11} & S'_{cc12} \\ S'_{cd21} & S'_{cd22} & S'_{cc21} & S'_{cc22} \end{bmatrix}. \tag{21}$$

The structure of $\mathbf{S}'_M$ in general is presented in (21). Assuming that the transmission line is perfectly symmetrical, i.e. all conversion terms are zero (see Figure 11 below as a practical illustration of this condition), the modal S-parameter matrix can be separated into two modal sub-matrices as (22). Since there is no energy exchange between the modes in

(22), they can be treated as separate (uncoupled) transmission lines with S-parameter matrices (23).

$$\mathbf{S}'_M = \begin{bmatrix} S'_{dd11} & S'_{dd12} & 0 & 0 \\ S'_{dd21} & S'_{dd22} & 0 & 0 \\ 0 & 0 & S'_{cc11} & S'_{cc12} \\ 0 & 0 & S'_{cc21} & S'_{cc22} \end{bmatrix} = \begin{bmatrix} \mathbf{S}'_{dd} & 0 \\ 0 & \mathbf{S}'_{cc} \end{bmatrix}. \tag{22}$$

$$\begin{aligned} \mathbf{S}'_{dd} &= \begin{bmatrix} S'_{dd11} & S'_{dd12} \\ S'_{dd21} & S'_{dd22} \end{bmatrix}, \\ \mathbf{S}'_{cc} &= \begin{bmatrix} S'_{cc11} & S'_{cc12} \\ S'_{cc21} & S'_{cc22} \end{bmatrix}. \end{aligned} \tag{23}$$

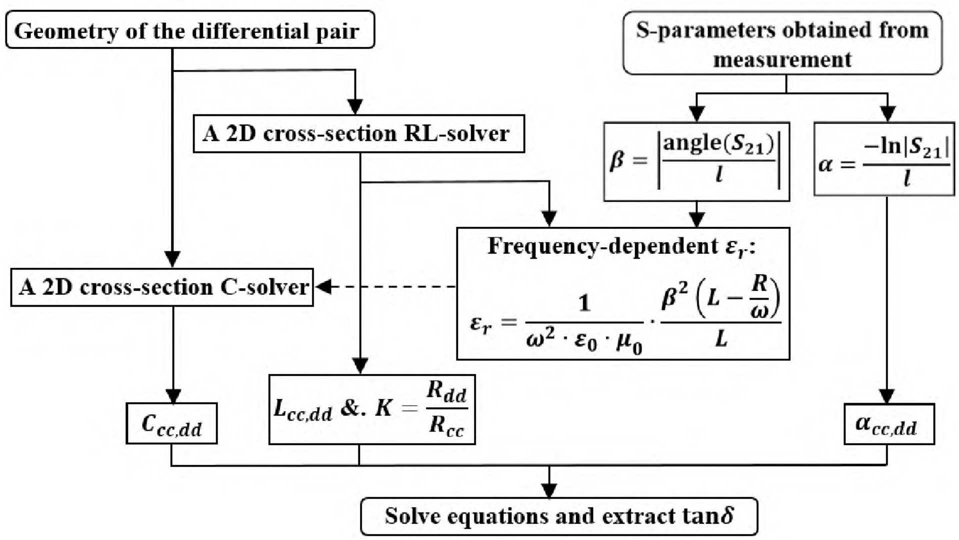

Figure 2. The flow chart of the proposed $\tan\delta$ extraction method.

After matrices (23) are calculated (for two standards needed for de-embedding), the Eigen-value de-embedding procedure is applied as described in [23] to obtain de-embedded modal transmission coefficients S_{cc21} and S_{dd21} to be used in (18).

Under the homogeneous dielectric assumption, the PUL modal conductances (G) are related to the modal dielectric loss tangents as Equation (24). If the stripline dielectric is uniform (a non-uniform case is discussed in Section 3), the common and differential loss tangents are equal, such that $\tan\delta_{cc} = \tan\delta_{dd} = \tan\delta$.

$$G_{cc,dd} = \tan\delta_{cc,dd} \cdot \omega \cdot C_{cc,dd} \,. \tag{24}$$

Taking this into account and by combining (12), (13) and (24) the following system of equations can be written:

$$\begin{cases} \alpha_{dd} = 0.5\left(R_{dd}\sqrt{C_{dd}/L_{dd}} + G_{dd}\sqrt{L_{dd}/C_{dd}}\right) \\ \alpha_{cc} = 0.5\left(R_{cc}\sqrt{C_{cc}/L_{cc}} + G_{cc}\sqrt{L_{cc}/C_{cc}}\right) \\ G_{dd} = \omega \cdot C_{dd} \cdot \tan\delta \\ G_{cc} = \omega \cdot C_{cc} \cdot \tan\delta \\ K = R_{dd}/R_{cc} \end{cases} . \tag{25}$$

Finally, by solving (25) with respect to $\tan\delta$ the following expression can be obtained [10]:

$$\tan\delta = \frac{2}{\omega} \cdot \frac{\alpha_{dd}\sqrt{\frac{C_{cc}}{L_{cc}}} - \alpha_{cc} \cdot K \cdot \sqrt{\frac{C_{dd}}{L_{dd}}}}{\sqrt{\frac{C_{cc}}{L_{cc}}} \cdot \sqrt{C_{dd}L_{dd}} - \sqrt{\frac{C_{dd}}{L_{dd}}} \cdot \sqrt{C_{cc}L_{cc}} \cdot K} \tag{26}$$

This formula relates the dielectric dissipation factor to the modal attenuation factors, modal PUL inductances (L), capacitances (C), and the ratio of modal resistances (K). The PUL capacitances and inductances, as well as K are calculated using a 2D cross-sectional solver for a known geometry of the transmission line. The real part of the dielectric permittivity needed to perform the 2D analysis is extracted from the phase constant of the transmission line, which is calculated using the de-embedded transmission coefficients as follows:

$$\beta = |\arg S_{21}/l|\,, \tag{27}$$

The phase constant depends on the per-unit-length capacitance and inductance of a transmission line. Besides the transmission line geometry, the PUL capacitance depends on the permittivity of the medium, while the PUL inductance depends on the permeability.

Since the PCB conductors and dielectric materials usually are non-magnetic, the permeability is known (equal to the permeability of vacuum) and the PUL inductance of the TL can be calculated before the permittivity extraction. The PUL inductance is the superposition of internal inductance due to lossy conductors' skin effect (L_{int}) and external inductance (L_{ext}) and the total phase constant β can be expressed as:

$$\beta = \omega\sqrt{LC} = \omega\sqrt{(L_{int} + L_{ext}) \cdot C} \ , \tag{28}$$

By introducing a phase constant depending on the external inductance only (i.e. the phase constant due to the TL dielectric),

$$\beta_{diel} = \omega\sqrt{L_{ext} \cdot C} \, , \tag{29}$$

the total phase constant can be rewritten as:

$$\beta = \beta_{diel}\sqrt{L \cdot (L - L_{int})^{-1}} \, , \tag{30}$$

The constant β_{diel} in turn is related to the relative permittivity of the dielectric:

$$\beta_{diel} = \omega\sqrt{\varepsilon_r \varepsilon_0 \mu_0}. \tag{31}$$

By combining (29) with (30) and (31) the relative permittivity can be found as:

$$\varepsilon_r = {\beta_{diel}}^2 \cdot (\omega^2 \cdot \varepsilon_0 \cdot \mu_0)^{-1} = \beta^2 \cdot (L - L_{int}) \cdot (\omega^2 \cdot \varepsilon_0 \cdot \mu_0 \cdot L)^{-1}. \tag{32}$$

According to [22, Ch. 5] the internal inductance L_{int} is related to the PUL resistance of the transmission line:

$$L_{int} = R/\omega. \tag{33}$$

By combining (32) and (33) the permittivity is finally extracted as (34). where L and R are calculated by using a 2D cross-sectional analysis, and β is obtained from the measurement using (27). The entire dielectric loss tangent extraction procedure is illustrated in the flow chart in Figure 2.

$$\varepsilon_r = \beta^2 \cdot (L - R/\omega) \cdot (\omega^2 \cdot \varepsilon_0 \cdot \mu_0 \cdot L)^{-1}, \tag{34}$$

3. NUMERICAL VALIDATION OF THE PROPOSED METHOD

To illustrate the feasibility of the proposed method it is first applied to the simulated transmission line. Two aspects are investigated primarily in this section: the accuracy of ε_r extraction (34), and the influence of possible dielectric inhomogeneity on the $\tan\delta$ extraction accuracy.

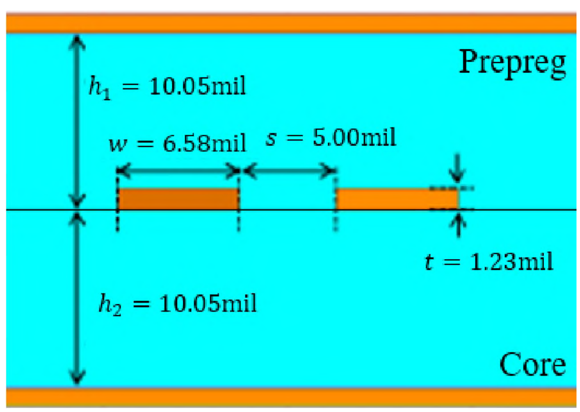

Figure 3. Cross-section of the stripline model used for loss tangent extraction.

A 2D model of the coupled stripline with the cross-sectional dimensions indicated in Figure 3 was created. The nodal PUL matrices of the model were calculated by solving a 2D cross-sectional problem using Ansys Q2D. The PUL matrices are converted to modal form by using (9). The modal attenuation coefficients are calculated according to (18) and the parameter K – according to (13). Finally, the loss tangent is calculated by (26) and compared to the actual value. To illustrate the extraction accuracy the model in Figure 3 was filled with the uniform dielectric material with frequency-independent parameters $\varepsilon_r = 3.4$ and $\tan\delta = 0.003$.

The ε_r extracted using (34) is shown in Figure 4 along with the actual value as well as the permittivity extraction error. The extraction results are practically operlapping with the acutal value, validating the permittivity extraction method.

Next the loss tangent was extracted according to (26) using actual and extracted (according to (34)) values of the dielectric permittivity. The results are presented in Figure 5 in comparison to the actual value of loss tangent. The extraction errors are also shown.

As can be seen by comparing curves in Figure 5 (b), the error in permittivity has a minimal impact on the loss tangent extraction. The extracted $\tan\delta$ curve is overlapping with the extraction result obtained using the actual ε_r which illustrates insignificance of the observed permittivity extraction error. At the same time both curves diverge from the actual value below 5 GHz which indicates other sources of errors (besides the error in ε_r) affecting the accuracy of the $\tan\delta$ extraction at low frequencies (see Section 5 for details and analysis. A two term Djordjevich model is proposed in Section 6 which essentially extrapolates the permittivity onto the low frequencies). For striplines in manufactured PCB, slightly inhomogeneous dielectric material is almost unavoidable because of the fabrication process, glass fiber effect, etc [4-6]. Up to 10% differences in ε_r or $\tan\delta$ between Prepreg and Core dielectric material may happen in multilayer PCBs [27]. The proposed material extraction method assumes ideally homogeneous dielectric material, which potentially might lead to errors in the extracted tanδ.

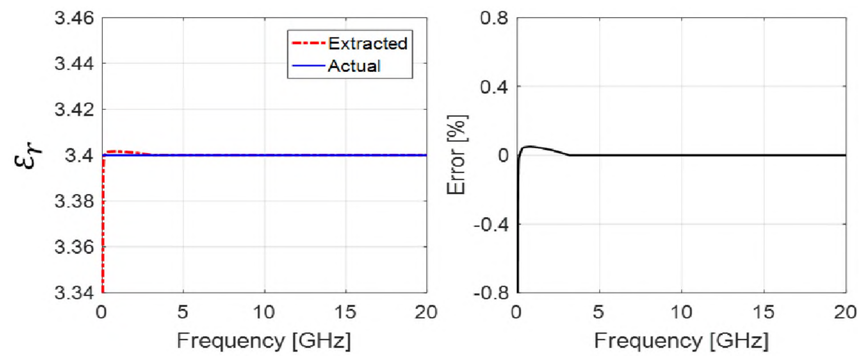

(a) (b)

Figure 4. Extracted dielectric permittivity (a) and the extraction error (b).

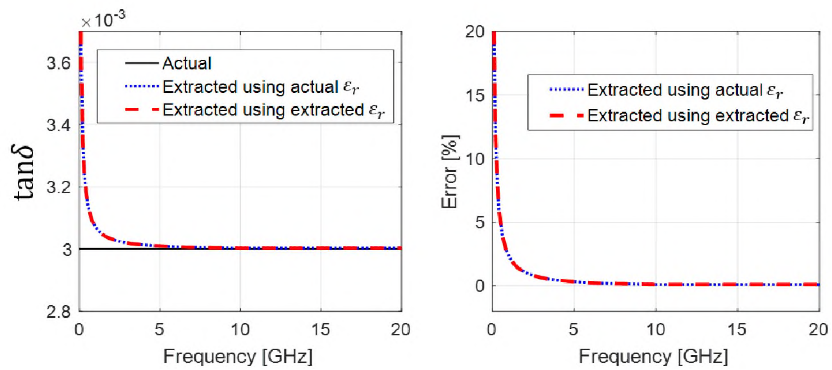

(a) (b)

Figure 5. Extracted loss tangent value using actual and extracted value of permittivity (a) and the corresponding extraction errors (b).

To find the impact of non-ideal dielectric material on the extraction procedure, the model in Figure 3 is filled with inhomogeneous dielectric with the boundary between the regions shown as a horizontal line. The S-parameters are calculated by the 2D model using different frequency-independent ε_r and tanδ for core and prepreg layers, while the extraction is carried out assuming homogeneous dielectric material. The impact of different

ε_r in prepreg and core is illustrated in Figure 6. The extracted ε_r is about 3.6 when $\varepsilon_{r,prepreg} = 3.45$ and $\varepsilon_{r,core} = 3.74$, which is approximately the mean value of $\varepsilon_{r,prepreg}$ and $\varepsilon_{r,core}$.

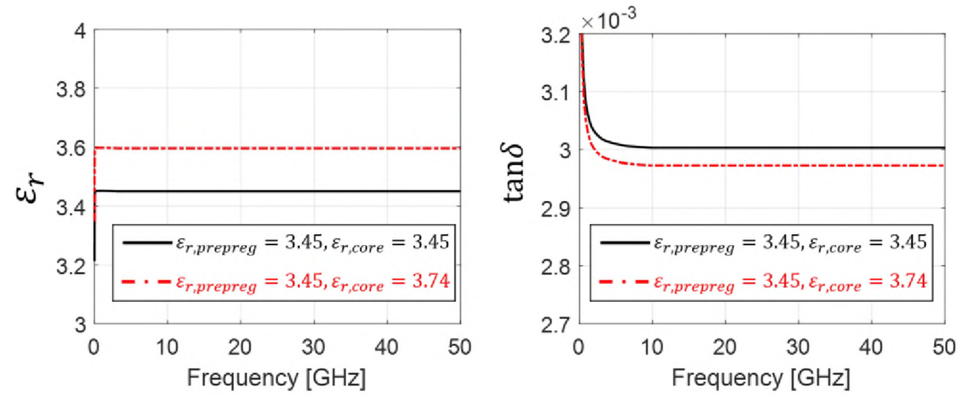

(a) (b)

Figure 6. Extracted ε_r and tanδ curves for homogeneous and slightly inhomogeneous cases. For both cases tanδ_{preg} = tanδ_{core} = 0.003; For the homogeneous case (black curve) $\varepsilon_{r,prepreg} = \varepsilon_{r,core} = 3.45$; The inhomogeneous case (red curve) is set with 10% differences between $\varepsilon_{r,prepreg}$ and $\varepsilon_{r,core}$ ($\varepsilon_{r,prepreg} = 3.45$, and $\varepsilon_{r,core} = 3.74$).

It is reasonable to treat the extracted ε_r as the effective value. The influence of a 10% difference between $\varepsilon_{r,prepreg}$ and $\varepsilon_{r,core}$ on the extracted tanδ is illustrated in Figure 6 (b). The value of extracted tanδ is less than 1% off from the actual value of the tanδ which illustrate low sensitivity of the proposed extraction method to the differences in the dielectric constant of PCB layers. The situation is different when layers have different tanδ values. To illustrate this, the ε_r of both layers was set to 3.45, while the tanδ values were different: tan$\delta_{prepreg}$ = 0.003 and tanδ_{core} = 0.0035. As Figure 7 (a) shows the impact of the tanδ difference on the extracted ε_r is negligible. However, it is not the case for tanδ.

As Figure 7 (b) shows the extracted value of $\tan\delta$ is very close to the mean value of prepreg and core $\tan\delta$, which will be very close to the effective value of $\tan\delta$ for transmission lines with an equal thickness of dielectric layers. The results presented above demonstrate that the proposed extraction method is relatively robust with respect to slight dielectric inhomogeneities in the striplines.

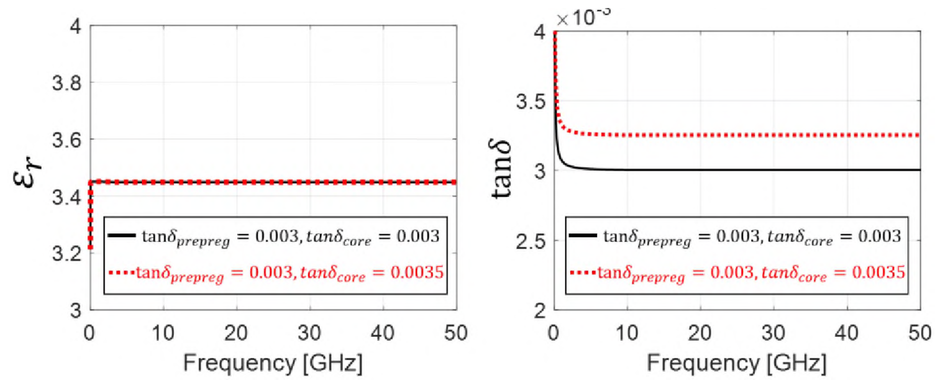

(a) (b)

Figure 7. Extracted ε_r and $\tan\delta$ curves for homogeneous and slightly inhomogeneous cases. For both cases $\varepsilon_{r,prepreg} = \varepsilon_{r,core} = 3.45$; For the homogeneous case (black curve) $\tan\delta_{prepreg} = \tan\delta_{core} = 0.003$; The inhomogeneous case (red curve) is set with $\tan\delta_{prepreg} = 0.003$, and $\tan\delta_{core} = 0.0035$.

4. LOSS TANGENT EXTRACTION USING MEASURED DATA

To test the proposed method in experiment a testing vehicle containing multiple differential lines was fabricated (Figure 8). The cross-section geometry of the coupled lines is presented in Figure 9. Two of the lines (1.3 inches and 15.8 inches, with the corresponding de-embedded length of 14.5 inches) were used for x2thru measurements. The roughness of ground planes and traces is comparable (the corresponding profiles are given in Figure 10. An example of raw and de-embedded S-parameters for the 15.8-inch transmission line are given in Figure 11 and Figure 12.

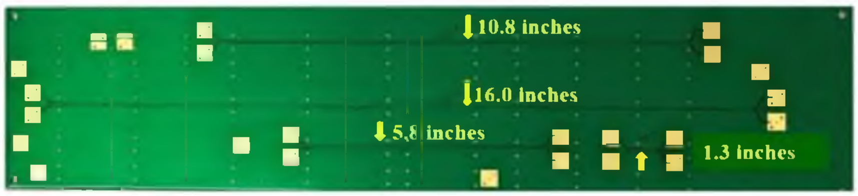

Figure 8. The testing board with several coupled striplines of different length.

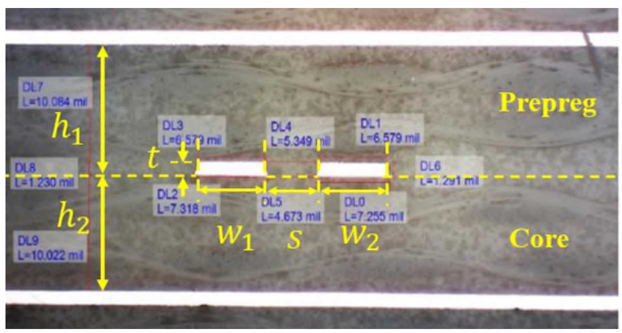

Figure 9. The cross-section of the coupled striplines. The trace width ($W_1 \approx W_2$) is 6.58 mil; edge-to-edge spacing (s) is 5.30 mil; dielectric height ($h_1 \approx h_2$) is 10.05 mil; trace thickness (t) is 1.23 mil. The yellow dashed line illustrates the boundary between prepreg and core.

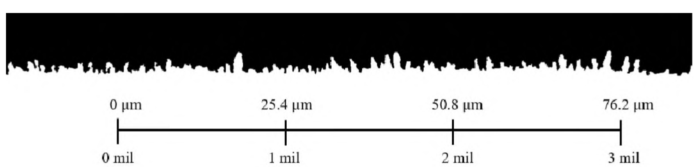

(a)

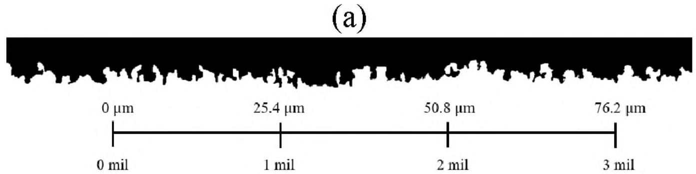

(b)

Figure 10. Profiles of ground (a) and signal (b) conductors obtained using optical microscopy. The RMS roughness levels obtained with roughness profile extraction tool [28] is 0.47µm for ground and 0.41 µm for signal conductors respectively.

The modal PUL parameters along with the parameter K calculated using the geometry information in Figure 9 in Q2D are shown in Figure 13.

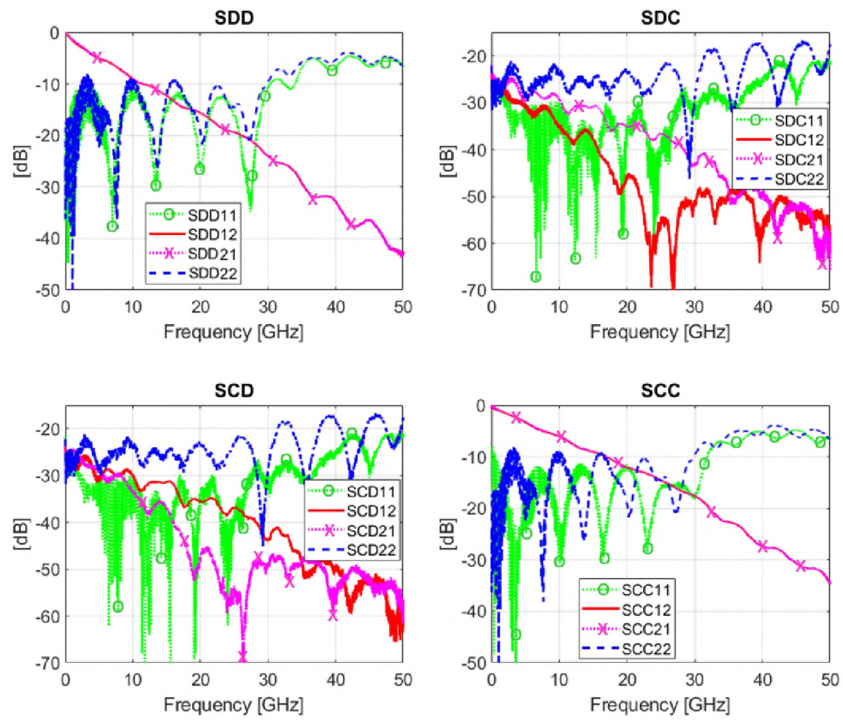

Figure 11. Raw modal S-parameters for the 15.8-inch differential transmission line. (a) differential to differential, (b) differential to common, (c) common to differential, (d) common to common.

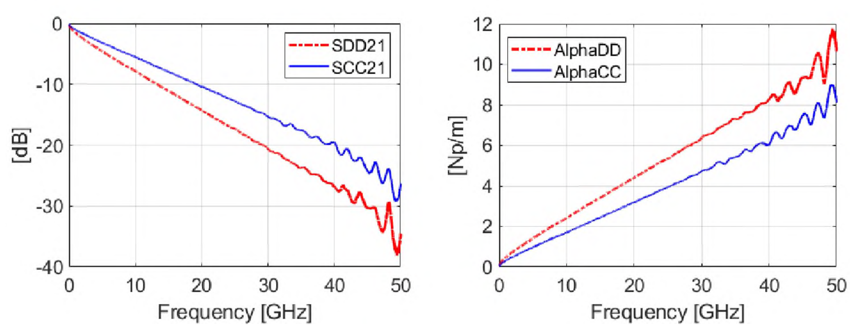

(a) (b)

Figure 12. De-embedded modal insertion loss (a) and attenuation factor (b) for the 15.8-inch line using the 1.3-inch line as a thru.

The extracted ε_r and $\tan\delta$ are shown in Figure 14. The reference $\tan\delta$ value provided by the laminate material maker is about 0.003 at 10 GHz, which is very close to the extraction result.

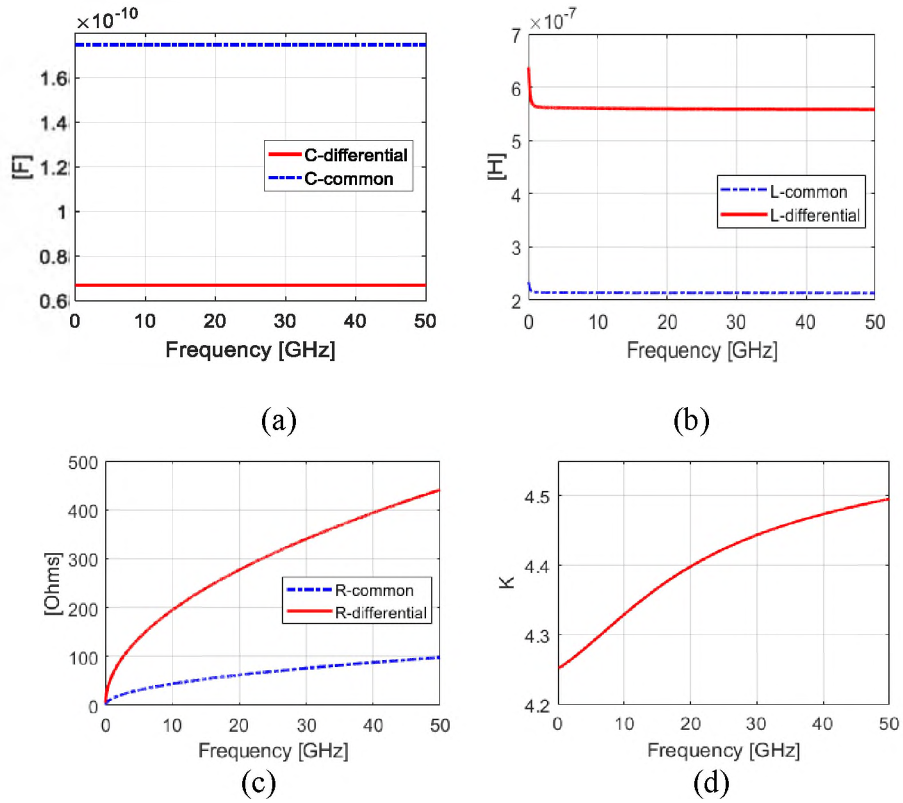

Figure 13. Components of the modal C(a), L(b), R(c) and K(d). Here, C is calculated using extracted ε_r. L and R matrices are calculated using (5). K is calculated using (9). The cross-sectional analysis is performed using Ansys Q2D.

5. ERROR MODEL FOR THE LOSS TANGENT EXTRACTION METHOD

As can be seen in Figure 14, the extracted loss tangent curve is relatively ‘clean’ from 5 to 30 GHz, however variations below and above this interval are significant. Obviously, the behavior below 5 and above 30 GHz is non-physical and requires explanation. The most obvious reason for this is simulation/measurement inaccuracies and the sensitivity of the extraction formula (26) to them (as can be seen from Section 3, inaccuracies caused by approximations in the extraction process are of much lower level).

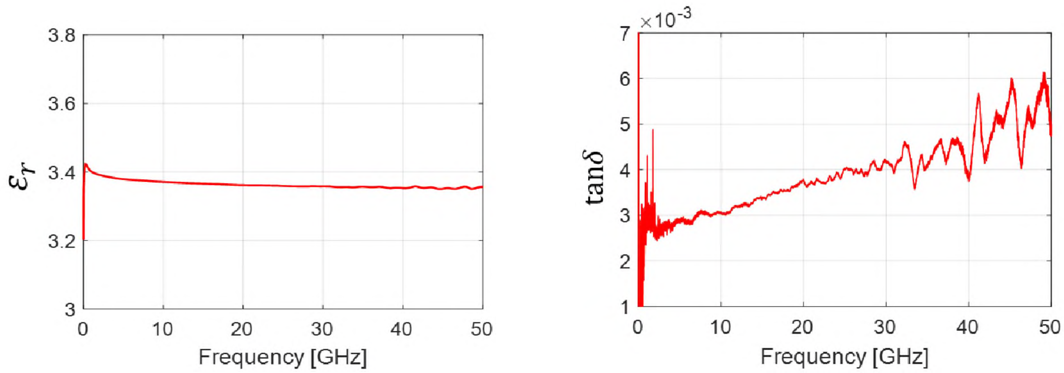

(a) (b)

Figure 14. The extracted ε_r (a) and tanδ (b) curves obtained by using the proposed method.

The proposed tanδ extraction method requires several groups of data: 1) raw S-parameters obtained by the VNA measurement; 2) de-embedded S-parameters to obtain attenuation factors; and 3) PUL inductance, capacitance and K calculated by a 2D cross-sectional solver. Therefore, three sources of errors can be identified: measurement errors, de-embedding errors, and simulation errors. Not all of these errors can be estimated accurately. For example, the simulation errors are especially difficult to determine directly, because the actual PUL parameters of the transmission lines are not accessible. Besides this the systematic (i.e. non-random) components of errors are difficult to determine because of lack of references (i.e. an independent measurement method). Because of these limitations the error analysis listed below cannot be called comprehensive, but we believe that it is still useful, because it allows to explain peculiarities of the extracted loss tangent curves and determine frequency range where the extracted data is the most accurate.

5.1 SIMULATION ERRORS

The resistance ratio K can be calculated correctly only if the metal conductors are meshed (as opposed to the boundary conditions on the surface) as demonstrated in [10], and the error strongly depends on the mesh density. Accuracy of the other simulated parameters (L and C) is also strongly dependent on the mesh. Therefore, the accuracy of the simulated parameters is estimated by mesh refinement [29].

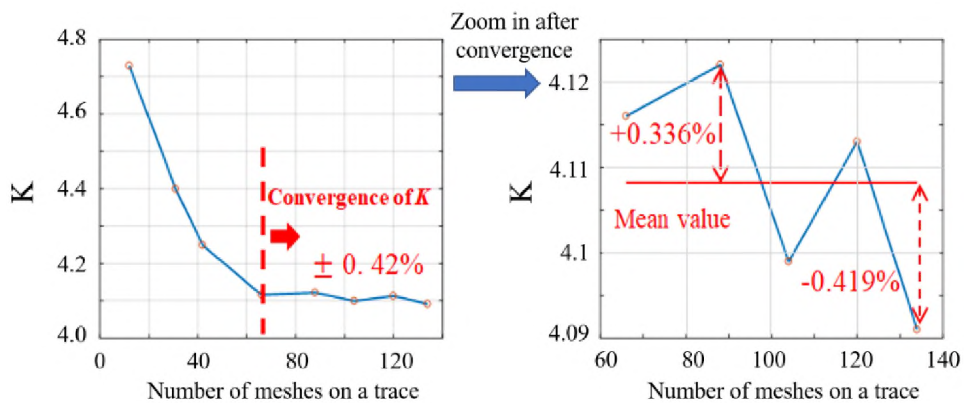

(a) (b)

Figure 15. Simulation error of the parameter K estimated by mesh refinement. (a) is with the number of meshes swept from 10 to 130. (b) is with the number of meshes swept from 65 to 135.

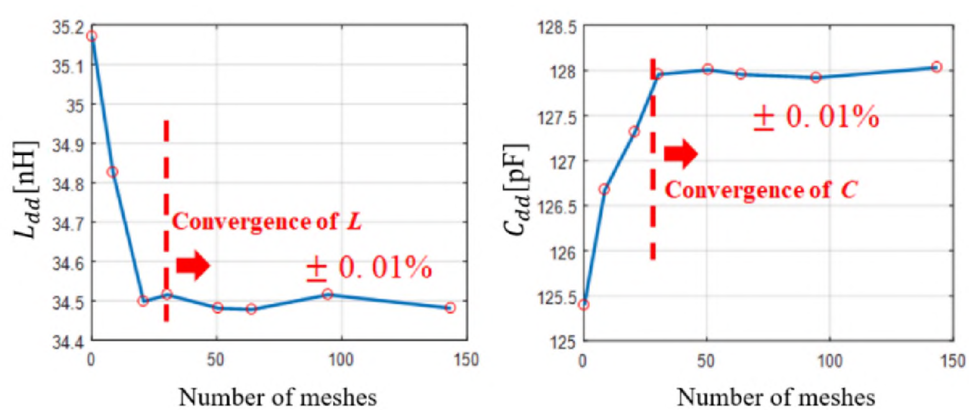

(a) (b)

Figure 16. Simulation error of L (a), and C (b) estimated by mesh refinement.

To achieve this the mesh count is gradually increased and for each mesh the parameters K, L, and C are calculated. As the mesh density increases the parameters converge to certain values. The simulation error is therefore estimated using the variations of converged K, L and C over several last iterations.

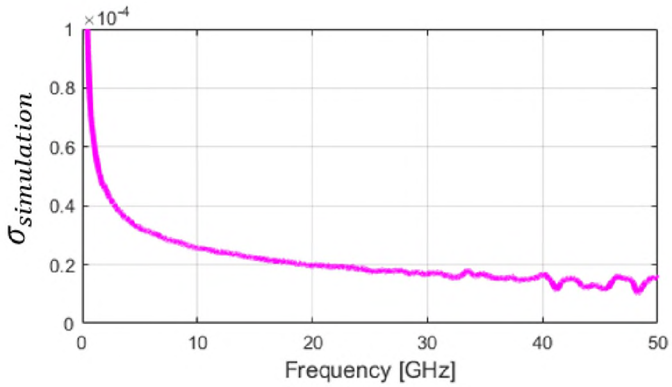

Figure 17. The estimated standard deviation of extracted $\tan\delta$ calculated using K, L and C subjected to Gaussian distribution. The actual $\tan\delta$ value is 3×10^{-3} at 10GHz.

An example of convergence curves at 5 GHz for the geometry in Figure 9 is shown in Figure 15 and 16. The variations of parameters were estimated as $\Delta K = \pm 0.4\%$, $\Delta L = \pm 0.01\%$, and $\Delta C = \pm 0.01\%$.

The influence of the simulation parameter accuracy on the accuracy of the extracted $\tan\delta$ was estimated numerically. To achieve this a statistical model for the simulated parameters is created by assuming Gaussian distribution with the mean value equal to the simulated value at the last mesh refinement step and the standard deviation equal to 1/3 of the variations determined above (such that the variations are within 99% confidence interval). 5000 random samples of the parameters were calculated, representing 5000 random combinations of the simulation parameters. For each of the combinations, the value of tanδ was calculated according to (26) and its standard deviation at each frequency was calculated (Figure 17).

As can be seen, the extracted tanδ errors are relatively large at low frequencies, and then gradually decrease with the increase of frequency. High error at low frequencies is due to poor conditioning of the system of equations (12) (indeed, at DC the difference between α_{dd} and α_{cc} is very small). As the frequency increases the conditioning of (12) improves, while the errors of the simulated parameters remain constant, leading to a decrease of the tanδ error.

5.2 ERROR DUE TO DE-EMBEDDING

All de-embedding methods require identical fixtures on Total and Thru lines (Fixture 1A = Fixture 2A; Fixture 1B = Fixture 2B, as shown in Figure 18). For the 'Eigen-value' de-embedding (also known as, 'Delta-L') [23-26] method used in this study, the symmetric design in fixtures for both Total and Thru lines (Fixture 1A = Fixture 1B = Fixture 2A = Fixture 2B) is also required.

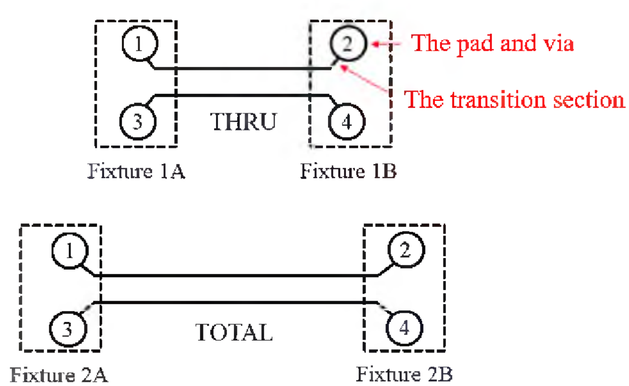

Figure 18. Total and Thru fixture definition. The fixture is composed of the connector, pad, plated-thru hole, via and transition section, etc. Manufacturing variation will cause differences between fixtures, such as the length of back-drilled stubs.

However, in reality the transitions from coaxial to stripline medium cannot be made perfectly identical due to geometrical variations and variability in the connector-pad transitions (this is evident in the TDR plots below). For the sake of the error analysis we assume that the source of de-embedding inaccuracies are the variations in the transitions from the coaxial cable to the differential stripline [30], violating identical and symmetrical assumptions formulated above.

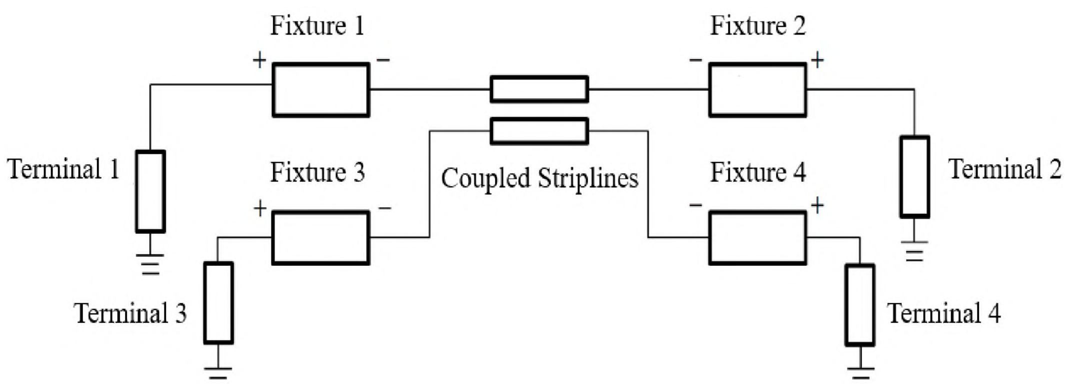

Figure 19. Overview of the Keysight ADS de-embedding model.

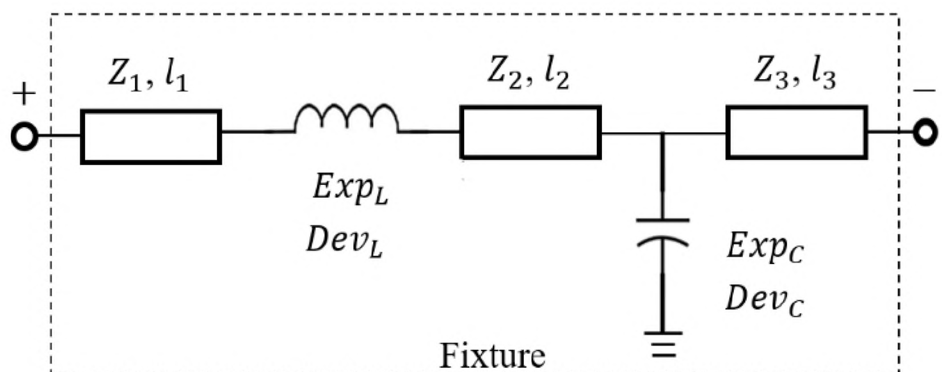

Figure 20. Circuit fixture model. For each fixture, the expectation and the standard deviation of the inductor and capacitor are tuned to achieve agreement with the measured TDR ($Exp_L = 1.75 \times 10^{-11}$ H; $Dev_L = 40\%$; $Exp_C = 4.8 \times 10^{-14}$ F; $Dev_C = 11\%$).

The error estimation strategy therefore is to estimate the variations of the transitions and then numerically propagate them through the de-embedding and extraction calculations and finally estimate the error of the extracted loss tangent.

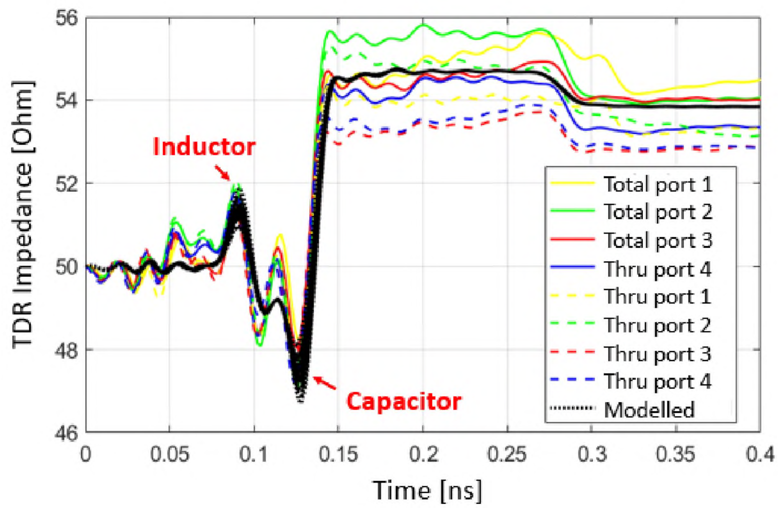

Figure 21. Measured and modeled fixture TDR responses. Modeled response contains multiple curves due to the model parameter variations.

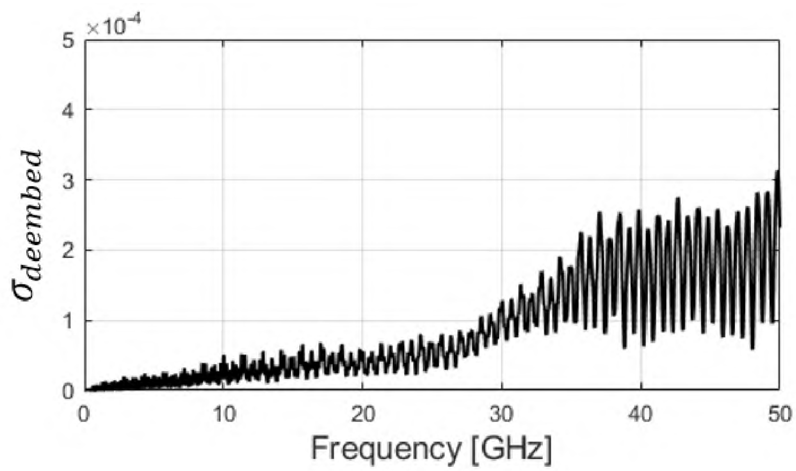

Figure 22. The standard deviation of extracted tanδ calculated using 1000 sets of de-embedded S-parameters. The Thru line length is 1.3 inch, and the Total line length is 16 inches. The actual tanδ value is 3×10^{-3} at 10GHz.

To achieve this a circuit model of the transmission lines with fixtures (transitions) was created (Figure 19 and 20). Each fixture is modeled by an excessive inductance and capacitance along with short portions of transmission lines. The values of the excessive capacitance and inductance are assumed to be normally distributed. The mean value and standard deviation of the capacitance and inductance are tuned to match the shape and the spread of the measured TDR response of the transmission lines as illustrated in Figure 21 (since two differential lines are used for each measurement, a total of 8 TDR curves are used to estimate the statistical parameters of the fixture models). Due to relatively low number of samples (8 curves), the statistics cannot be determined exactly, but a rough estimation still can be made.

After the fixture model is created a Monte-Carlo simulation is performed (with random values of excessive inductances and capacitances in all transitions) and one thousand random combinations of the Thru and Total S-parameters are created for de-embedding. The one thousand extracted $\tan\delta$ curves are then used to estimate the standard deviation of the $\tan\delta$.

The $\tan\delta$ standard deviation curve ($\sigma_{deembed}$) is presented in Figure 22. As can be seen from the plot the de-embedding error in general increases with frequency due to the increase of the fixture reflections (and hence increased influence of their variability), however at some frequencies where the de-embedding equation is relatively poorly conditioned, the sensitivity to errors is higher. In general, the error curve contains a periodic pattern, the periodicity of which depends on the electrical lengths of the thru and total standards.

5.3 VNA MEASUREMENT ERROR

The S-parameters measurement is performed using Keysight N5244A 4-PORT PNA-X Network Analyzer. The VNA calibration is performed using an electronic calibration kit N4692. With proper choice of averaging factor and intermediate frequency bandwidth, the VNA measurement noise can be reduced to quite low levels. However, frequency-dependent measurement error is still unavoidable [31]. To estimate the impact of frequency-dependent VNA measurement error to the tanδ extraction method, a statistical analysis of the measurement data is performed.

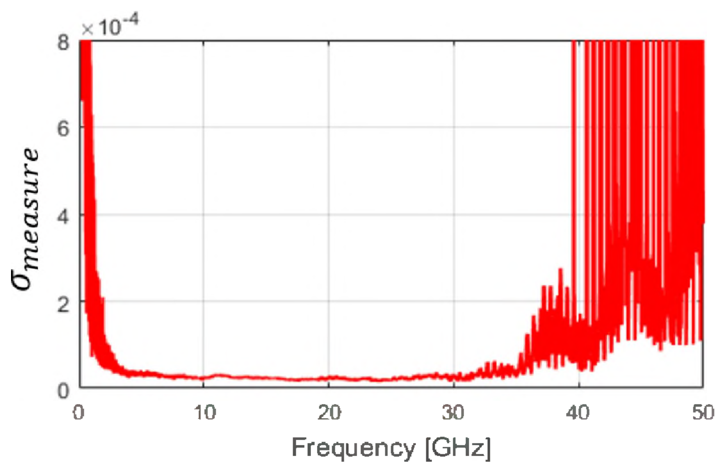

Figure 23. The standard deviation of the extracted tanδ calculated using 400 sets of VNA measured S-parameters. The actual tanδ value is 3×10^{-3} at 10 GHz.

The following procedure was used to estimate the measurement errors. After the VNA calibration, several tens of Thru and Total S-parameters are saved (without disconnecting the cables in each case). After that, several hundreds of Thru/Total s-parameter combinations are created for de-embedding and for each of them the value of tanδ is calculated. The standard deviation ($\sigma_{measure}$) of extracted tanδ curve is estimated

(Figure 23). Since the fixtures remain the same during the measurements and fixed values of the simulated parameters (L, C, and K) are used for extraction, the variability in the extracted loss tangent is due to the measurement error only.

Figure 23 shows large VNA measurement error occurs at relatively low frequency (below 1 GHz), and it decreases as frequency goes up. The minimum error appears around several gigahertz and remains low up to 35 GHz; after that is starts to grow rapidly. High error level at low frequencies can be explained by poor conditioning of the system of equations (12) (the values of α_{cc} and α_{dd} become very close to each other). At high frequencies the contribution of the measurement noise increases (simply because the transmission coefficients decrease in absolute value and become comparable to noise).

5.4 THE CONFIDENCE INTERVAL OF EXTRACTED LOSS TANGENT

The contributions of all three factors (simulation error, de-embedding error, VNA measurement error) factors estimated for the test vehicle in Figure 8 are compared in Figure 24. As can be seen, below 4 GHz the measurement and simulation errors dominate, then from 10 GHz up to 40 GHz the de-embedding error is the dominating factor, and above 40 GHz, the measurement and de-embedding errors become comparable.

Assuming that the different error sources are independent to each other, the total standard deviation of extracted tanδ is calculated using a property of a linear combination of independent random variables as:

$$\sigma_{total} = \sqrt{(\sigma_{deembed})^2 + (\sigma_{measure})^2 + (\sigma_{simu})^2} \ . \tag{35}$$

Finally, the tanδ can be modeled as a Gaussian variable:

$$\tan\delta \sim \text{Gaussian}(\tan\delta_{nominal}, \sigma_{total}) \ , \tag{36}$$

where, $\tan\delta_{nominal}$ is the extracted value of the loss tangent. The upper ($\tan\delta_{upper}$) and lower ($\tan\delta_{lower}$) bounds of extracted $\tan\delta$ confidence interval are defined using 99% confidence level with $(3 \cdot \sigma_{total})$ as:

$$\tan\delta_{upper} = \tan\delta_{nomianl} + 3 \cdot \sigma_{total}\,, \tag{37}$$

$$\tan\delta_{lower} = \tan\delta_{nomianl} - 3 \cdot \sigma_{total}\,. \tag{38}$$

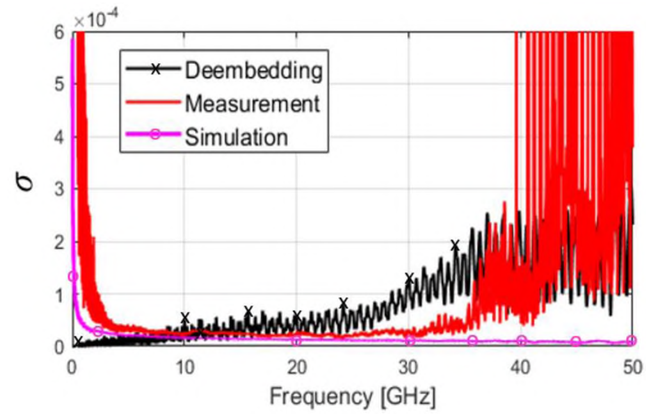

Figure 24. Contributions to the standard deviation of the extracted $\tan\delta$ due to the measurement error, de-embedding error and simulation error. The Thru line length is 1.3 inch, and the Total line length is 16 inches. The actual $\tan\delta$ value is about 3×10^{-3} at 10GHz.

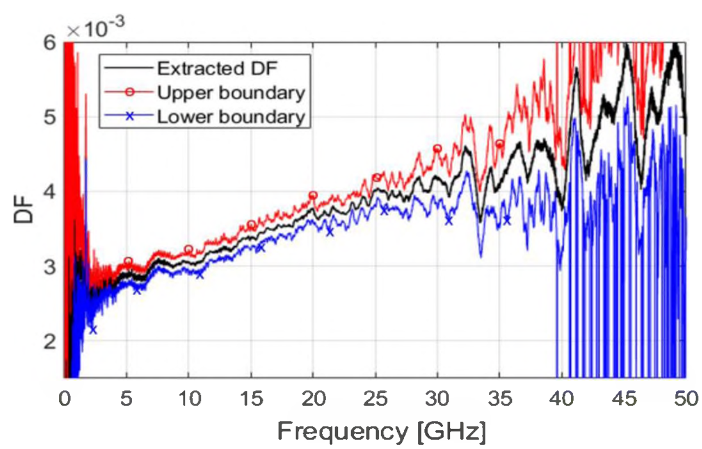

Figure 25. The extracted $\tan\delta$ curve and confidence intervals.

The extracted curve along with the confidence intervals are presented in Figure 25, and the corresponding confidence interval expressed in percent – in Figure 26. As can be seen, in the interval from 3 to 30 GHz the extracted tanδ error (99% confidence) does not exceed 10%, and on the interval from 5 to 20 GHz it is less than 6%.

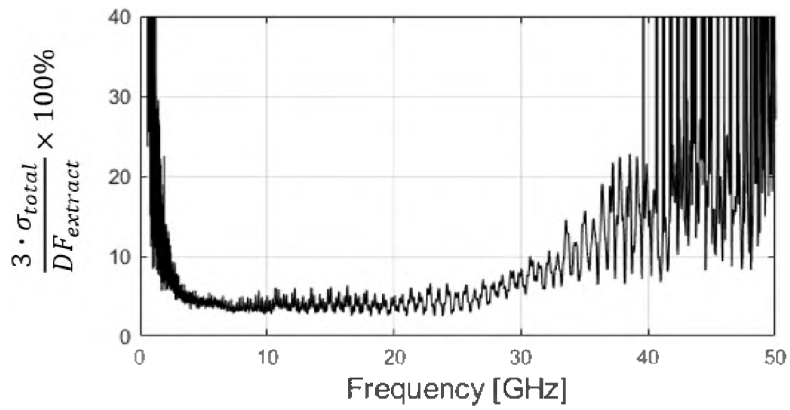

Figure 26. Estimated extraction error percentage defined as 99% confidence.

As was said above, presented error analysis in not complete and probably gives a conservative estimate of the extraction accuracy. However, it explains unphysical behavior of the extracted curve below 3 GHz (high sensitivity to errors due to poor conditioning of (12)) and variations above 30 GHz (lack of de-embedding accuracy and influence of the measurement noise).

6. CAUSAL MODEL FOR LOSSY DIELECTRICS

In Section 5 the confidence interval of extracted tanδ is calculated. Any curve within the confidence interval (or within the envelopes of the confidence interval as a worst-case estimate) may be a potential candidate for the final output extraction result. Of course, infinite number of curves satisfies this condition, but based on an *a priori* knowledge about the behavior of typical PCB dielectric materials, the class of possible approximations can be limited to slowly-changing (i.e. “smooth”) and monotonic curves. Another important consideration is the causality of the selected approximation which would allow using the model for time-domain simulations.

6.1 EXISTING DIELECTRIC MODELS

There is a number of approaches to dielectric modelling that can produce smooth casual responses. One of the most widely used of them is a Djordjevic model [11]. The complex dielectric constant according to the model is calculated as:

$$\varepsilon' = \varepsilon'_\infty + \Delta\varepsilon' \cdot (m_2 - m_1)^{-1} \cdot \ln(\omega_2/\omega - 10) \ , \tag{39}$$

$$\varepsilon'' = \varepsilon' \cdot \tan\delta = -0.5\pi \cdot \Delta\varepsilon' \cdot [(m_2 - m_1) \cdot \ln(10)]^{-1} \ , \tag{40}$$

where ε'_∞ is the value of dielectric constant at infinite frequency, and $\Delta\varepsilon'$ is the difference between the dielectric constant at DC and infinity.

Selection of numbers m_1 and m_2 determines the frequency range from $2\pi f_1 = 10^{m_1}$ to $2\pi f_2 = 10^{m_2}$ with very weak frequency dependency of ε. In practice the lower frequency is set to the kHz, and the higher frequency to the THz ranges to model weakly dispersive PCB materials. However, this low-dispersive assumption leads to a practically frequency-independent $\tan\delta$ of the model in the range $f_1 - f_2$, and does not allow modeling the extracted curves similar to one in Figure 14(b). Moving the lower frequency f_1 into the working frequency range (i.e. from kHz to GHz frequency) does allow to model the loss dispersion but at an inevitable cost of introducing the strongly frequency-dependent dielectric constant.

When the Djordjevic model is used on practice the loss dispersion is typically ignored and the Djordjevic model with very weakly dispersive ε is created by picking a single value at a certain frequency like an example in Figure 27 demonstrates (here, the value at 5 GHz was selected). For extracted tanδ such an approach will, of course, lead to underestimation of transmission line loss at higher frequencies. An alternative to the Djordjevic model is to use a multi term Debye or Lorenz approximation (an example of a double-term Debye model is presented in [32]). While these approximations can be used on practice, the most important drawback associated with this approach is a need to have multiple terms in approximations for wide frequency ranges (from hundreds of MHz to tens of GHz), leading to large number of parameters to be determined. Here we would like to propose an extension of the Djordjevic model which allows to produce wideband responses (with practically unlimited frequency bounds) having a frequency-dependent loss using just 4 parameters.

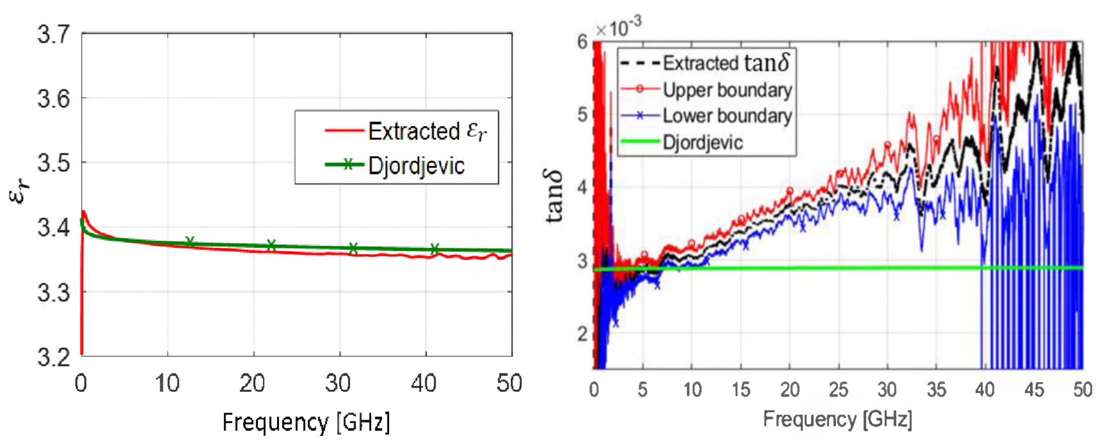

(a) (b)

Figure 27. The ε_r (a) and tanδ (b) fitted using Djordjevic model.

6.2 DJORDJEVIC MODEL WITH TWO DISPERSIVE TERMS

As an improvement allowing to model frequency-dependent dielectrics, we propose to add a second Djordjevic term to the dielectric model such that the permittivity of the dielectric is represented as:

$$\varepsilon_{tot} = \varepsilon_{d1} + \varepsilon_{d2}\,, \tag{41}$$

where both terms ε_{d1} and ε_{d2} are described by the same equations (39) and (40), but have different parameters. The term ε_{d1} is the traditional Djordjevic term with low dispersion in the frequency range of interest, and term ε_{d2} has the frequency f_1 in the GHz frequency range, low dielectric constant (which is fixed and is not a model parameter) and high loss.

The parameters of the model are therefore: 1) ε'_∞ for the ε_{d1}, 2) $\Delta\varepsilon'$ for the ε_{d1}, 3) frequency f_1 for ε_{d2}, 4) ε'_∞ or $\Delta\varepsilon'$ for ε_{d2}. The parameters are tuned (or optimized) to produce the curve that satisfies the confidence interval of the extracted tanδ (in the sense defined above) and at the same time approximates the real part of permittivity. An example approximation is presented in Figure 28.

Table 1. Two-term Djordjevic Model.

	f_1	f_2	m_1	m_2	$\Delta\varepsilon'$	ε'_∞
ε_{d1}	1 kHz	10 THz	3.80	13.80	0.12	3.21
ε_{d2}	30 GHz	10 THz	11.28	13.80	0.04	0.08

The approximation parameters are listed in Table 1. As can be seen by combining two Djordjevic it is possible to model frequency dependent dielectric loss with loss dispersion in the dielectric constant in a very wide frequency range, producing strictly monotonic curves (including all derivatives) with just 4 parameters.

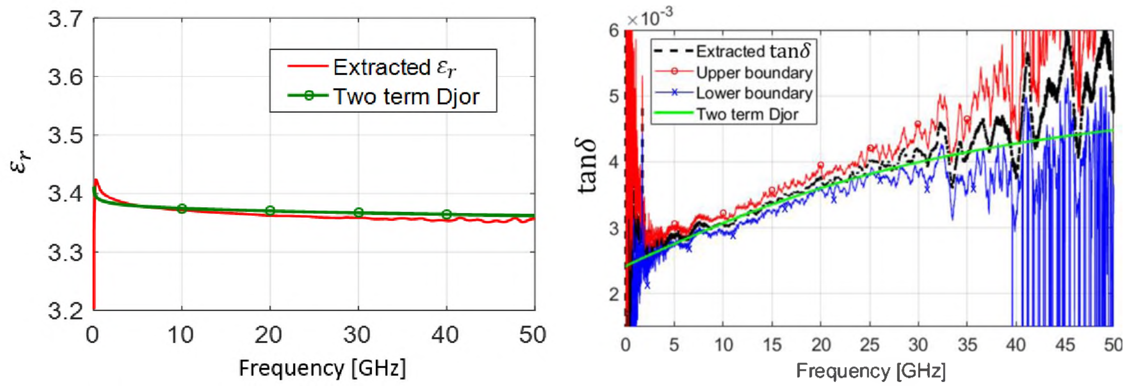

(a) (b)

Figure 28. The ε_r (a) and $\tan\delta$ (b) fitted using two-term Djordjevic model

6.3 TIME-DOMAIN VALIDATION OF THE PROPOSED MODEL

The proposed dielectric model (Figure 28) was validated by calculating eye-diagrams of the differential channels formed by a 30-inch transmission line.

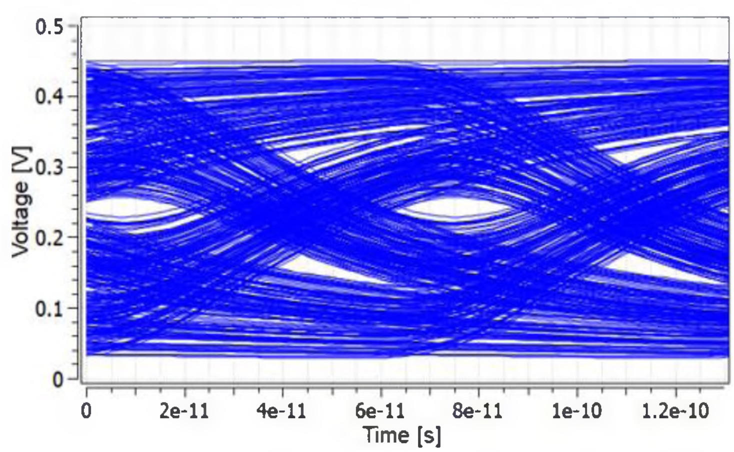

Figure 29. The eye diagram of the measurement data. The Rise/fall time is set to 5ps, and data rate is 15Gbps.

The dielectric was modeled by the two-term Djordjevic model as described above and the conductor surface roughness was modeled using the Huray model. The Huray model had the following parameters: RMS roughness $h_{rms} = 0.43\mu$m, ball size $a_{ball} = 0.63\mu$m, number of balls $N_{ball} = 25$, and the tile area $A_{tile} = 90\mu\text{m}^2$. The parameters for the roughness model were determined empirically for profiles in Figure 10.

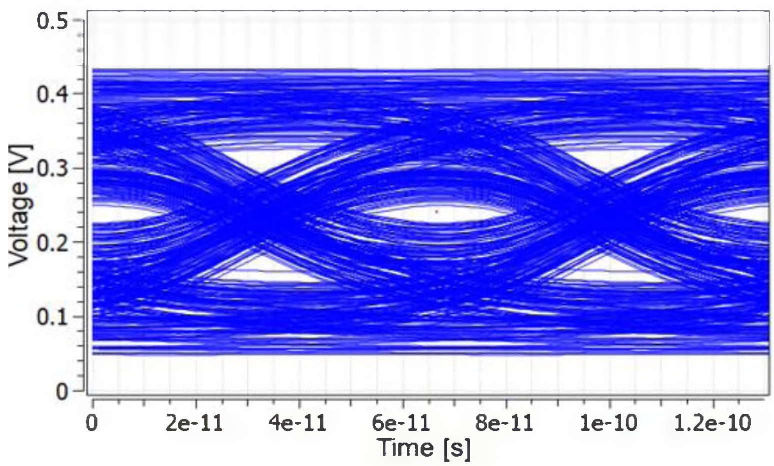

Figure 30. The modeled eye diagram of the two-term Djordjevic model.

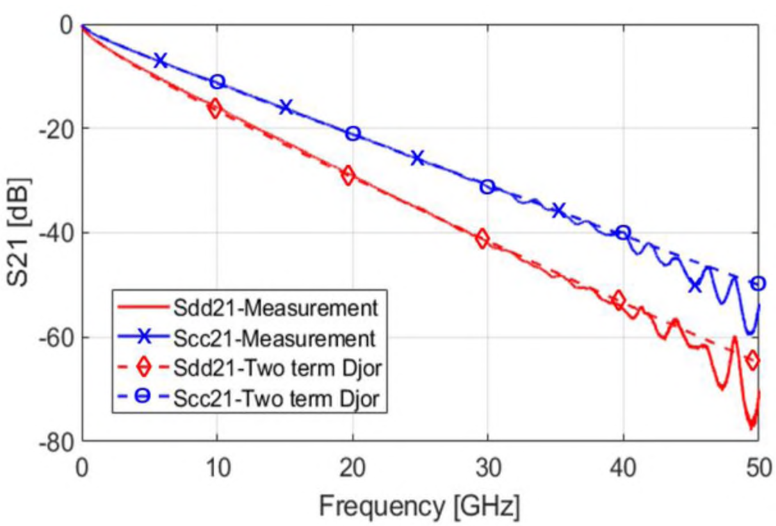

Figure 31. The modeled insertion loss of the two-term Djordjevic model.

For comparison, the models with a popular one-term Djordjevic models (i.e. practically frequency independent loss) were also created. The eye diagrams for all models in the time domain were calculated. The eye diagram calculated using the propagation constant extracted directly from the de-embedded S-parameters is also given as a reference.

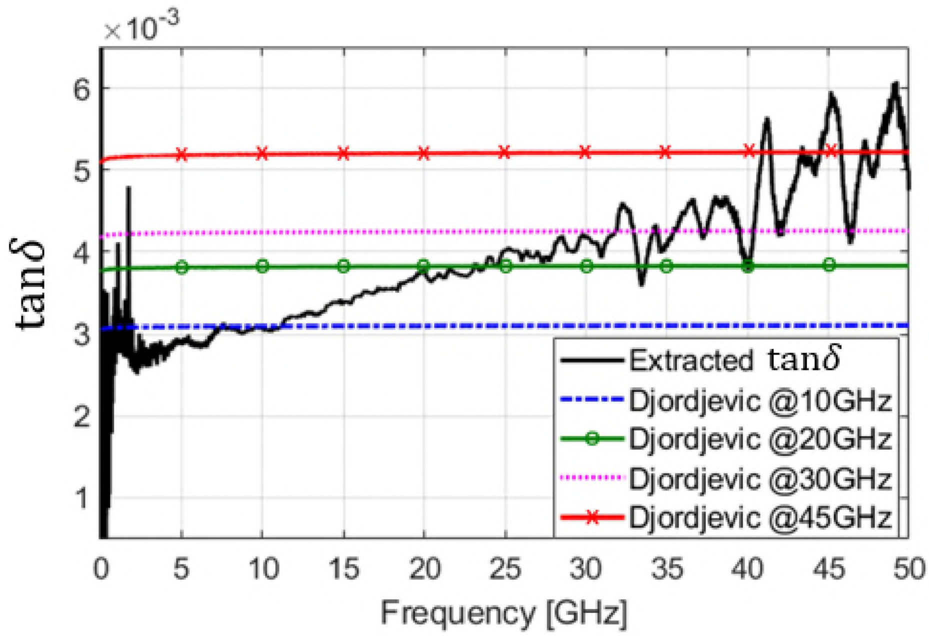

Figure 32. One-term Djordjevic models generated by selecting $\tan\delta$ values at 10/20/30/45GHz

The time domain data for measurement and the proposed two-term dielectric model using extracted $\tan\delta$ data are shown in Figure 29 and Figure 30. The corresponding frequency domain comparison is presented in Figure 31. The results show good agreement in terms of the eye-opening and frequency-domain loss.

A similar comparison for the model using a one-term Djordjevic dielectric expression is shown in Figure 33 for values of $\tan\delta$ picked at different frequencies (Figure

32). As can be seen all examples exhibit a lack of accuracy either in time or frequency domain compared to the proposed two-term model.

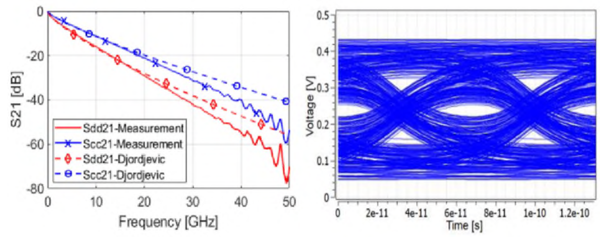

(a) One-term Djordjevic model using known tanδ at 10GHz (tanδ =0.0030)

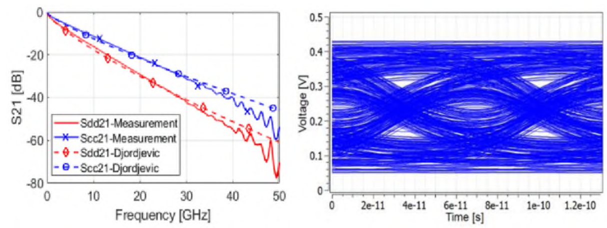

(b) One-term Djordjevic model using known tanδ at 20GHz (tanδ =0.0038)

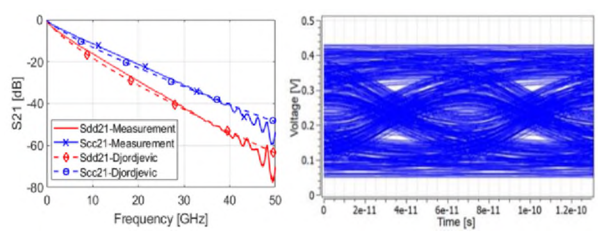

(c) One-term Djordjevic model using known tanδ at 30GHz (tanδ =0.0042)

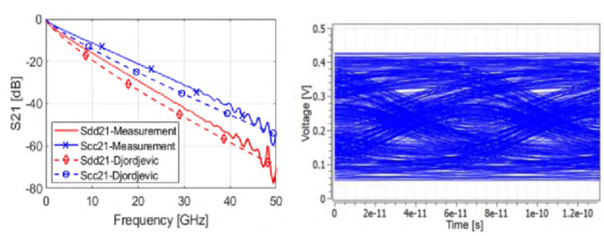

(d) One-term Djordjevic model using known tanδ at 45GHz (tanδ =0.0051)

Figure 33. Modeled insertion loss and eye diagram of the Djordjevic model with different tanδ values.

7. CONCLUSION

A new tanδ extraction method is proposed and analyzed. The method has low sensitivity to surface roughness, making extraction on low-loss materials possible (i.e. when the roughness contribution is comparable with the contribution of the dielectric loss). No *a priori* information about the behavior of the dielectric properties or attenuation constant is needed for extraction, which allows capturing arbitrary frequency-dependent behavior of the tanδ.

To estimate the accuracy of the extraction the error model taking into account errors due to de-embedding, VNA measurement and simulation is proposed. The error model explains inaccuracies in the extracted tanδ at low at high frequency and allows to estimate impact of the measurement and simulation inaccuracies on the accuracy of extraction, which can be ultimately used to optimize the design of the extraction PCB.

To model the extracted frequency-dependent dielectric loss, a two-term Djordjevic model is proposed to fit the raw extraction result. Compared to the traditional one-term Djordjevic model, the proposed approach allows to model the performance of signal-integrity simulation with improved accuracy using a small number of parameters.

REFERENCES

[1] J. Krupka, D. Cros, M. Auburg, P. Guillon, “Study of whispering gallery modes in anisotropic single-crystal dielectric resonators”, IEEE Trans. Microw. Theory Techn., vol. 42, no. 1, pp. 56–61, Jan. 1994.

[2] J. Krupka, et al., “Use of whispering-gallery modes for complex permittivity determinations of ultra-low-loss dielectric materials”, IEEE Trans. Microw. Theory Techn., vol. 47, no. 6, pp. 752–759, Jun. 1999.

[3] J. Krupka, R. N. Clarke, O. C. Rochard, A. P. Gregory, “Split post dielectric resonator technique for precise measurements of laminar dielectric specimens—Measurement uncertainties”, in Proc. 13th Int. Conf. Microw., Radar, Wireless, Wroclaw, Poland, May 22–24, 2000, pp. 305–308, vol. 1.

[4] X. Tian, Y. Zhang, J. Lim, K. Qiu, R. Brooks, J. Zhang, J. Fan, “Numerical investigation of glass-weave effects on high-speed interconnects in printed circuit board”, in Proc. IEEE Int. Symp. EMC, Raleigh, NC, USA, Aug. 4–8, 2014, pp. 475–479.

[5] A. Koul, M. Y. Koledintseva, S. Hinaga, J. L. Drewniak, “Differential extrapolation method for separating dielectric and rough conductor losses in printed circuit boards”, IEEE Trans. Electromagn. Compat., vol. 54, no. 2, pp. 421–433, Apr. 2012.

[6] S. Jin, X. Fang, B. Chen, H. Gao, X. Ye, J. Fan, “Validating the transmission-line based material property extraction procedure including surface roughness for multilayer PCBs using simulations”, in Proc. IEEE Int. Symp. EMC, Ottawa, CN, USA, Jul. 25–29, 2016, pp. 472–477.

[7] S. Jin, B. Chen, X. Fang, H. Gao, and J. Fan, “Improved ‘root-omega’ method for transmission-line based material property extraction for multi-layer PCBs”, IEEE Trans. Electromagn. Compat., vol. 59, no. 4, pp. 1356–1367, Mar. 2017.

[8] M. Y. Koledinstseva, A. V. Rakov, A. I. Koledinstseva, J. L. Drewniak, and S. Hinaga, “Improved experiment-based technique to characterize dielectric properties of printed circuit boards”, IEEE Trans. Electromagn. Compat., vol. 56, no. 6, pp. 1559–1566, Dec. 2014

[9] M. Y. Koledinstseva, T. Vincent, A. Ciccomancini, and S. Hinaga, “Method of effective roughness dielectric in a PCB: Measurement and full-wave simulation verification”, IEEE Trans. Electromagn. Compat., vol. 57, no. 4, pp. 807–814, Aug. 2015.

[10] S. Yong, Y. Liu, H. Gao, B. Chen, S. De, S. Hinaga, D. Yanagawa, J. Drewniak, V. Khilkcvich, “Dielectric Dissipation Factor (DF) Extraction Based on Differential Measurements and 2-D Cross-sectional Analysis”, in Proc. IEEE Int. Symp. EMC, Long Beach, CA, USA, 30 Jul-3, 2018, pp. 217-222.

[11] A. R. Djordjevic, R. M. Biljic, V. D. Likar-Smiljanic and T. K. Sarkar, "Wideband frequency-domain characterization of FR-4 and time-domain causality", IEEE Trans. on Electromag. Compat, Nov. 2001, pp. 662-667.

[12] X. Guo, H. Gao, G. Shen, Q. Liu, V. Khilkevich, J. Drewniak, S. De, S. Hinaga, D. Yanagawa, "Design methodology for behavioral surface roughness model", in Proc. IEEE Int. Symp. EMC, Ottawa, 2016, pp. 927-931,

[13] S. Hall, S. G. Pytel, P. G. Huray, D. Hua, A. Moonshiram, G. A. Brist, and E. Sijercic "Multigigahertz Causal Transmission Line Modeling Methodology Using a 3-D Hemispherical Surface Roughness Approach", IEEE Trans. Microw. Theory Tech., vol. 55, no. 12, Dec. 2007, pp. 2614 – 2624

[14] T. Granberg, "Handbook of Digital Techniques for High Speed Design", Upper Saddle River, NJ: Prentice Hall, 2004.

[15] C. R. Paul, "Analysis of Multiconductor Transmission Lines", 2nd Edition, John Wiley & Sons, Inc, 2008.

[16] D. M. Pozar, "Microwave Engineering". Fourth Edition, John Wiley & Sons, Inc, 2012[1]

[17] H. A. Wheeler, "Formulas for the skin effect," Proc. IRE, vol. 30, no. 9, pp. 412–424, Sep. 1942.

[18] M. E. Hellman and I. Palocz, "The effect of neighboring conductors on the currents and fields in plane parallel transmission lines," IEEE Trans. Microw. Theory Techn., vol. 17, no. 5, pp. 254–259, May 1969.

[19] S. Yong, V. Khilkevich, X-D Cai, C. Sui, B. Sen, J. Fan, "Comprehensive and Practical Way to Look at Far-End Crosstalk for Transmission Lines With Lossy Conductor and Dielectric" IEEE Trans. Electromagn. Compat., Early Access, 2019.

[20] P. G. Huray, S. Hall, S. G. Pytel, F. Oluwafemi, R. Mellitz, D. Hua, and P. Ye, "Fundamentals of a 3-D 'Snowball' Model for Surface Roughness Power Losses", proceedings of the IEEE conference on Signals and Propagation on Interconnects - May 14, 2007, Genoa, Italy.

[21] J. E. Bracken, "A Causal Huray Model for Surface Roughness", DesignCon 2012

[22] S. Hall and H. Heck, "Advanced Signal Integrity for High-Speed Digital Designs", Wiley-IEEE press, 2009.

[23] B. Chen, X. Ye, B. Samaras, J. Fan., “A novel de-embedding method suitable for transmission-line measurement”, IEEE Asia-Pacific Symposium on Electromagnetic Compatibility (APEMC), May 26-29, 2015.

[24] Q. Huang, J. Li, J. Zhou, W. Wu, Y. Qi, and J. Fan, “De-embedding method to accurately measure high-frequency impedance of an O-shape spring contact”, in Proc. Int. Symp. IEEE Electromagn.Compat., 2014, pp. 600–603.

[25] B. Chen, M. Tsiklauri, C. Wu, S. Jin, J. Fan, Xiaoning Ye, and Bill Samaras. “Analytical and numerical sensitivity analyses of fixtures de-embedding”, in Proc. Int. Symp. IEEE Electromagn.Compat, 2016, pp. 440-444

[26] B. Chen, J. He, Y. Guo, S. Pan, X. Ye, J. Fan, “Multi-Ports (2^n) 2×-Thru De-Embedding: Theory, Validation, and Mode Conversion Characterization”, IEEE Trans. Electromagn. Compat., vol. 61, no. 4, Aug 2019.

[27] G. Brist, “Design Optimization of Single-Ended and Differential Impedance PCB Transmission Lines”. Online (accessed in Oct, 2019) https://www.jlab.org/eng/eecad/pdf/053designop.pdf

[28] S. De, A. Gafarov, M. Y. Koledintseva, R. J. Stanley, J. L. Drewniak, S. Hinaga, “Semi-Automatic Copper Foil Surface Roughness Detection from PCB Microsection Images”, in Proc. Int. Symp. IEEE Electromagn.Compat, 2012, pp. 132-137.

[29] M. M. Ilic´, A. Ž Ilic, and B. M. Notaros, “Efficient large-domain 2-D FEM solution of arbitrary waveguides using p-refinement on generalized quadrilaterals”, IEEE Trans. Microwave Theory Tech., vol. 53, no. 4, pp. 1377–1383, Apr. 2005

[30] S. Yong, Y. Liu, H. Gao, S. Hinaga, S. De, D. Padilla, D. Yanagawa, J. Drewniak, V. Khilkevich, “A Practical De-embedding Error Analysis Method Based on Statistical Circuit Models of Fixtures”, in Proc. Int. Symp. IEEE Electromagn. Compat, 2019, pp. 45-50

[31] “Keysight 2-Port and 4-Port PNA-X Network Analyze”, accessed Oct, 2019. http://literature.cdn.keysight.com/litweb/pdf/N5245-90008.pdf

[32] J. Zhang, J. Drewniak, D. Pommerenke, M. Koledintseva, R. DuBroff, W. Cheng, Z. Yang, Q. Chen, A. Orlandi “Causal RLGC(f) models for transmission lines from measured S-parameters,” IEEE Trans. Electromagn. Compat., vol. 52, no. 1, pp. 189–198, Feb. 2010.

II. RESISTANCE MODELING FOR STRIPLINES WITH DIFFERENT SURFACE ROUGHNESS ON THE PLANES

ABSTRACT

To model additional conductor loss due to foil surface roughness various empirical or physical models have been brought up to provide surface roughness correction factors for the per-unit-length (PUL) resistance assuming certain roughness of foil conductors. However, for striplines on typical printed circuit board, different sides of the traces and references planes may have different surface roughness levels due to the fabrication process. Traditionally engineers may calculate surface roughness correction factors using averaged roughness level of the upper and lower sides of the trace. However, this empirical estimation may lead to inaccurate modeling results especially when the stripline is not vertically symmetrical or the differences among the roughness levels of planes are significant. In this project, a methodology is presented to calculate the resistance of a stripline with different surface roughness levels on upper and lower sides of the trace and reference planes. After separating the resistances contributed by different smooth planes, each plane's resistance is corrected independently using corresponding surface roughness correction factor. The stripline's resistance is obtained by combining the corrected resistances of different planes.

Keywords: Skin effect, surface roughness, striplines, printed circuit boards, signal integrity

1. INTRODUCTION

Conductor loss is an increasingly important factor affecting the signal integrity (SI) performance for high-speed channels. It has been quite evident that the skin-effect formulas ignoring foil surface roughness underestimate attenuation as frequency goes up to tens of gigahertz [1-3]. Various approaches [4-9] have been proposed to calculate the frequency-dependent surface roughness correction factor using the cross-sectional profile or the root-mean-square (RMS) roughness levels.

However, the previously proposed surface roughness modeling approaches assumed equal roughness on all conductor surfaces instead of modelling realistic stripline structures consisting of four rough planes (the upper and lower sides of the traces, and the upper and lower reference planes). Actually, different surface roughness levels on different planes can be commonly observed due to printed circuit boards (PCB) fabrication process. To provide better adhesion between copper and epoxy resin, various foil treatments are applied by PCB vendors to roughen up certain sides of the planes [10-13]. In addition, the electrodeposition (ED) process leads to foil with one side smoother and the other side rougher [6][13].

As the SEM image shows in Figure 1, the upper and lower sides of the trace, as well as the upper and lower reference planes have noticeable difference in terms of surface roughness levels. Traditionally SI engineers may use the averaged surface roughness levels of all planes to calculate the surface roughness correction factor, assuming different planes have similar contribution to the total resistance. However, as Section 2 will show, the averaging approach leads to results with low accuracy. A more precise modeling approach is needed.

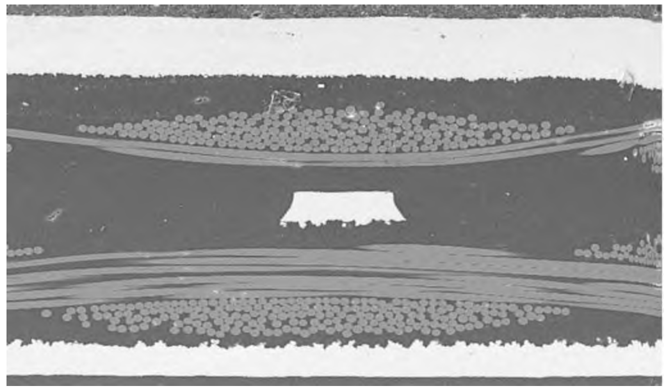

Figure 1. The SEM image of a stripline. It can be observed that different planes (upper and lower sides of the trace and the referene) on stripline have different surface roughness.

The authors will start from the analysis of the PUL resistance contributions of different smooth planes. The surface roughness correction factors determined by approaches presented in [4-9] are applied to the smooth planes' resistances accordingly. The rough single-ended or coupled stripline resistance is calculated by combining the corrected resistances of each rough plane.

2. SINGLE-ENDED STRIPLINES

2.1 CONDUCTOR LOSS OF STRIPLINES

Let us start from some basics about stripline conductor loss. The upper and lower ground planes of the stirpline have the same potential, and the signal line has different potential. The cross-section of the stripline is illustrated in Figure 2(a). As frequency goes up the AC resistance due to skin effect will cause the current distribution concentrated on the edges. In a vertically asymmetrical stripline ($h_1 \neq h_2$), the resistances of the upper (R_{h1}) and lower edges (R_{h2}) of the line will differ due to unbalanced cross-sectional area where the current is flowing. According to [14, (5-18)], R_{h1} and R_{h2} are modeled using the resistances of the trace (R_{t1}, R_{t2}) and reference plane (R_{r1}, R_{r2}) in series:

$$\begin{aligned} R_{h1} &= R_{t1} + R_{r1} \\ R_{h2} &= R_{t2} + R_{r2} \end{aligned} \tag{1}$$

According to [14, (5-19)], the total resistance of a stripline is modeled by the resistances of the upper and lower portions (R_{h1}, R_{h2}) in parallel. The total resistance of the single-ended stripline with smooth surfaces is expressed therefore as:

$$\begin{aligned} R_{se} &= R_{h1} \cdot R_{h2} \cdot (R_{h1} + R_{h2})^{-1} \\ &= (R_{t1} + R_{r1}) \cdot (R_{t2}+R_{r2})(R_{t1} + R_{r1} + R_{t2} + R_{r2})^{-1} \end{aligned} \tag{2}$$

Compared to the case with smooth foil surfaces, additional conductor loss due to absorption and scattering is introduced when rough foil surfaces are taken into account [7].

The resistance increment is usually modeled using a frequency-dependent correction factor [4-9]. Different planes with different roughness levels can be modeled by four independent surface roughness correction factors (K_{t1}, K_{t2}, K_{r1}, K_{r2} illustrated in Figure 3).

The resistances contributed by the top and bottom portions of the stripline with rough foil surfaces are expressed as:

$$\begin{aligned} R_{h1,SR} &= K_{t1} \cdot R_{t1} + K_{r1} \cdot R_{r1} \\ R_{h2,SR} &= K_{t2} \cdot R_{t2} + K_{r2} \cdot R_{r2} \end{aligned} \tag{3}$$

According to (2), the expression of the total resistance of the single-ended stripline with four rough planes is presented as (4). Thus, if the resistance contributed by different smooth planes (R_{t1}, R_{t2}, R_{r1}, R_{r2}) can be calculated, the rough stripline can be modeled using (4) with known surface roughness correction factors (K_{t1}, K_{t2}, K_{r1}, K_{r2}).

$$R_{se,SR} = R_{h1,SR} \cdot R_{h2,SR} \cdot (R_{h1,SR} + R_{h2,SR})^{-1} \tag{4}$$

$$= \frac{(K_{t1}R_{t1} + K_{r1}R_{r1})(K_{t2}R_{t2} + K_{r2}R_{r2})}{K_{t1}R_{t1} + K_{r1}R_{r1} + K_{t2}R_{t2} + K_{r2}R_{r2}}$$

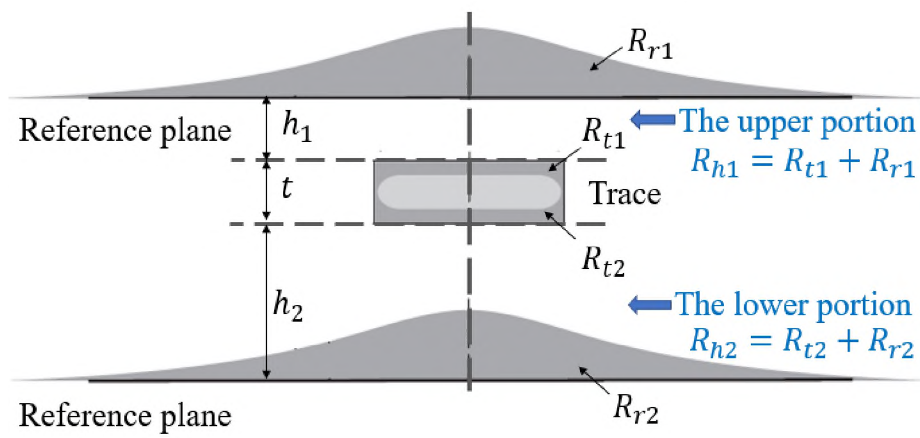

(a)

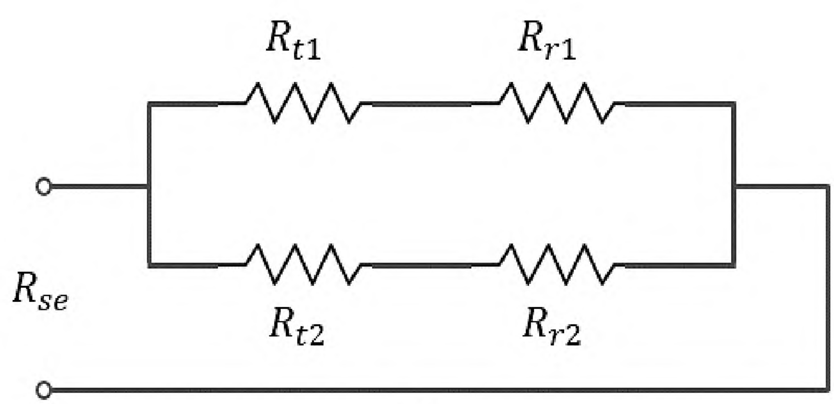

(b)

Figure 2. Current distribution in the trace and reference planes of a smooth stripline (a) and the relative equivlent resistance circuit (b). According to [14, Figure 5-8], the resistance of the upper and lower side of the trace, as well as the upper and lower reference planes are expressed as R_{t1}, R_{t2}, R_{r1} R_{r2} respectively.

However, a 2D or 3D solver only provides the total PUL resistance of the stripline (not the plane contributions). In the following subsection, an approach to calculate the resistances of four smooth planes (R_{t1}, R_{t2}, R_{r1}, R_{r2}) will be presented.

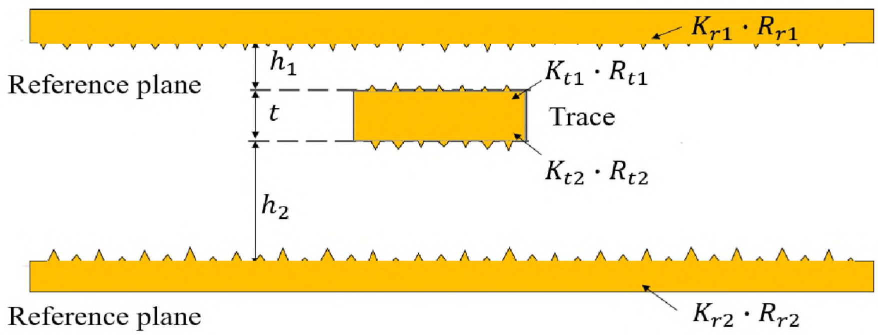

Figure 3. A stripline with four rough planes. Surfcae roughness correction factors for the upper side of the trace (K_{t1}), lower side of the trace (K_{t2}), upper reference plane (K_{r1}), lower reference plane (K_{r2}) are used to model the resistance of corresponding rough planes.

2.2 RESISTANCES CONTRIBUTED BY DIFFERENT PLANES

Since the distances between the reference planes and the trace (h_1 and h_2) are the determinant factors for the resistance [14], two additional 2D models with vertically symmetrical geometry are created to calculate the upper and lower portions' resistance (R_{h1}, R_{h2}) of the stripline. As Figure 4 illustrates, the current distribution in the upper and lower portions of these models are supposed to be the same due to the symmetry.

The resistances contributed by the upper ($R_{sy,h1}$) and lower ($R_{sy,h2}$) portions are calculated in models (a) and (b). According to (2), the upper and lower portions are in parallel. Thus, the resistances of the upper and lower portions of the stripline are calculated using Equation (5). To verify the modeling approach presented by (6), a single-ended stripline model with cross-sectional geometry shown in Figure 5 is created using Ansys

Q2D [15]. The total resistance of the stripline (R_{se}) is calculated directly by the 2D simulation for reference.

$$R_{h1} = 2R_{sy,h1}$$
$$R_{h2} = 2R_{sy,h2} \tag{5}$$

Two additional 2D models with symmetrical geometry (illustrated by Figure 6) are created to calculate the resistances of the stripline's upper and lower portion ($R_{sy,h1}$ and $R_{sy,h2}$).

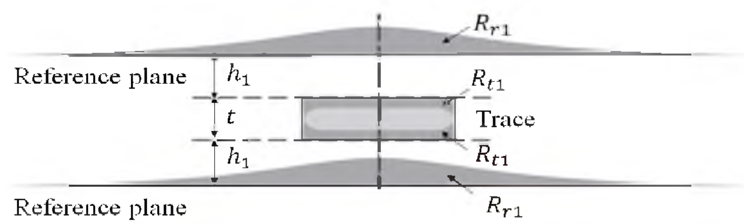

(a)

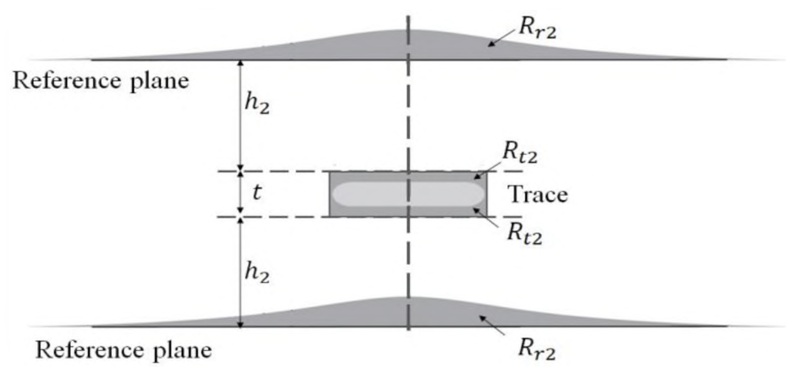

(b)

Figure 4. By introducing two additional vertically symmetrical models, the resistances of the upper (a) and lower (b) portions of the stripline are calculated.

By inserting (5) into (2), the total resistance of the stripline can be modeled as:

$$R_{se} = 2 \cdot R_{sy,h1} \cdot R_{sy,h1} \cdot \left(R_{sy,h1} + R_{sy,h2}\right)^{-1} \tag{6}$$

The comparison between directly simulated R_{se} and modeled R_{se} using (6) is performed. According to Figure 7 (b), the modeled R_{se} has a very good match (below 3% difference) with the directly simulated R_{se}.

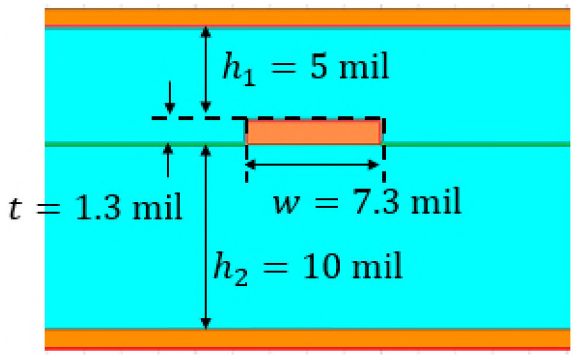

Figure 5. The cross-sectional geometry of the single-ended stripline.

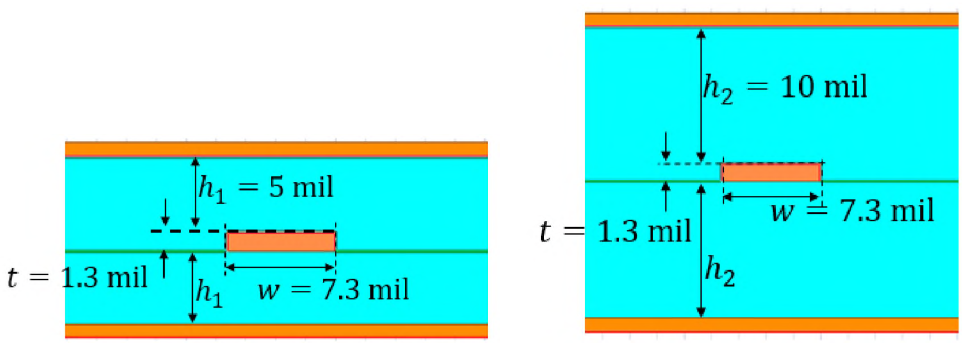

(a) (b)

Figure 6. Two additional 2D models with symmetrical geometry are introduced. Model (a) and (b) are vertically balanced with trace to reference distance equal to h_1 and h_2.

In addition to calculating the resistances of the upper and lower portions of the stripline, the contribution from the reference plane and the trace can be further separated by assigning a perfect electric conductor (PEC) to the trace or reference plane. The models are illustrated by Figure 8. The modeled R_{se} calculated by (8) has a good mach with simulated R_{se} as Figure 9 (b) shown.

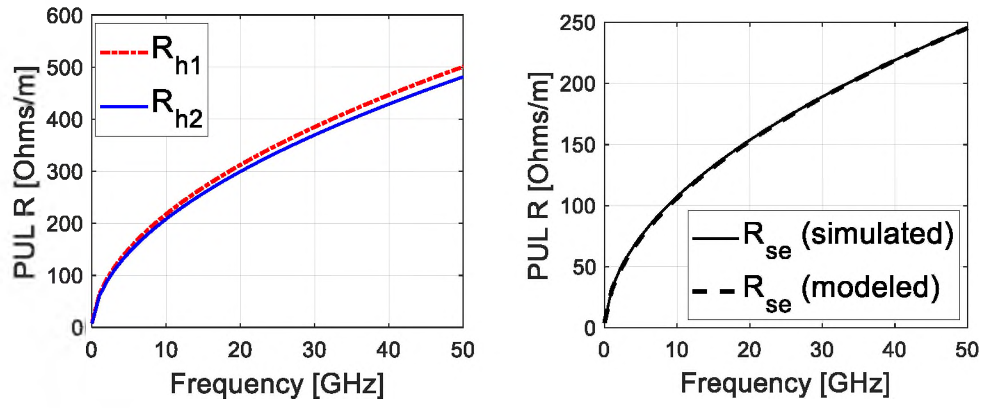

(a) (b)

Figure 7. The illustrations of R_{h1}, R_{h2} (a), and the comparision between modeled and simlated R_{se} (b). R_{h1} and R_{h2} calculated using the additional 2D models illustrated by Figure 6. The R_{se} is modeled using R_{h1} and R_{h2}.

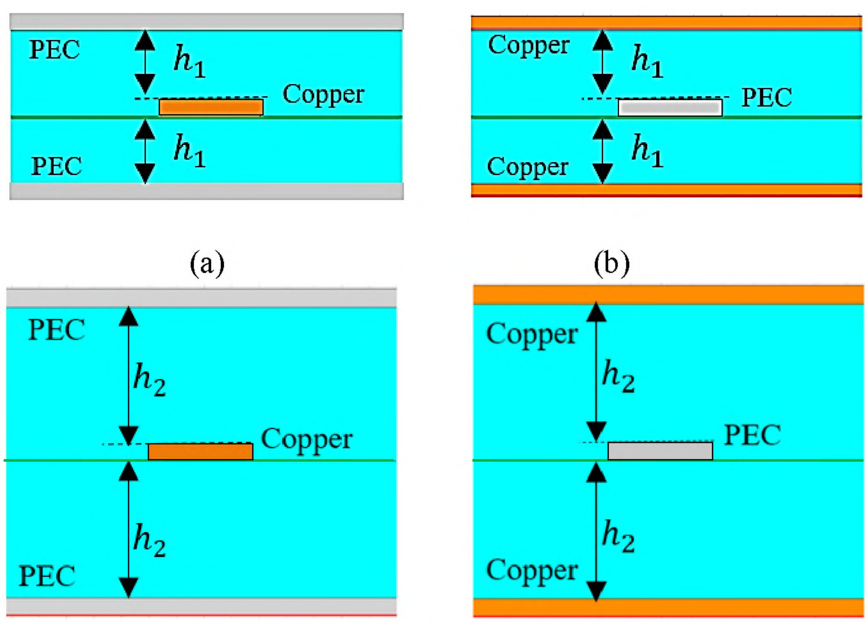

(c) (d)

Figure 8. Four additional 2D models are introduced to calculate resistacnes R_{t1} (a), R_{r1} (b), R_{t2} (c), and R_{r2} (d).

For example, to calculate the resistance of the upper side of the trace (R_{t1}) for the stripline illustrated in Figure 5, the 2D model illustrated by Figure 8 (a) is created.

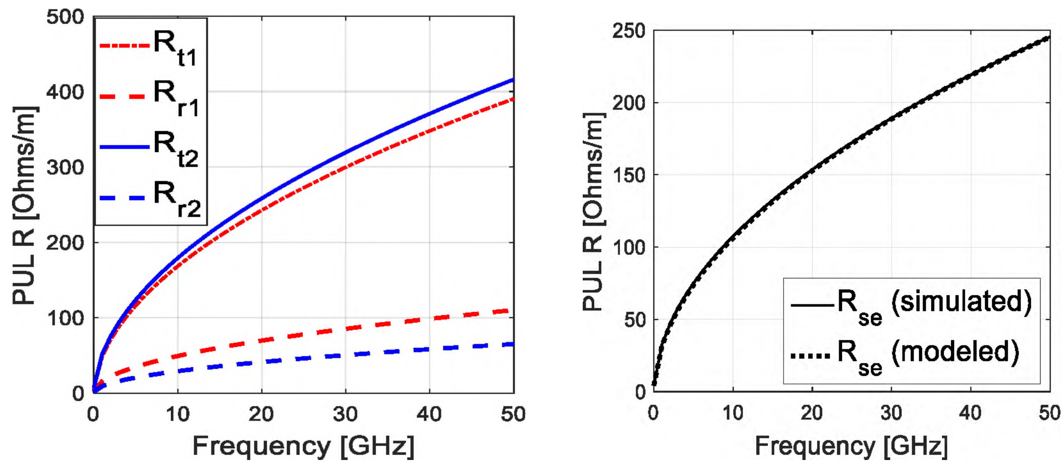

(a) (b)

Figure 9. The illustrations of R_{t1}, R_{r1}, R_{t2}, R_{r2} (a), and the comparision between the modeled and simulated single-ended resistances R_{se} (b).

By assigning PEC to the reference planes, the resistance of reference plane is excluded. $R_{sy,h1}^{PEC,R}$ is calculated by the 2D model, and it is equal to the resistance of the two symmetrical 'upper sides' of the trace in parallel. Thus, the resistances of different planes are calculated:

$$\begin{aligned} R_{t1} &= 2R_{sy,h1}^{PEC,R} \\ R_{r1} &= 2R_{sy,h1}^{PEC,T} \\ R_{t2} &= 2R_{sy,h2}^{PEC,R} \\ R_{r2} &= 2R_{sy,h2}^{PEC,T} \end{aligned} \tag{7}$$

where, $R_{sy,h1}^{PEC,R}$, $R_{sy,h1}^{PEC,T}$, $R_{sy,h2}^{PEC,R}$ and $R_{sy,h2}^{PEC,T}$ are calculated by the 2D models illustrated by Figure 8 (a-d) respectively.

By inserting (7) into (2), the resistance of the stripline can be modeled using Equation (8). To validate the modeling approach expressed by (8), using the stripline geometry in Figure 5, the resistances of four different planes are calcaulted.

$$R_{se} = \frac{2(R_{sy,h_1}^{PEC,R} + R_{sy,h_1}^{PEC,T})(R_{sy,h_2}^{PEC,R} + R_{sy,h_2}^{PEC,T})}{R_{sy,h_1}^{PEC,R} + R_{sy,h_1}^{PEC,T} + R_{sy,h_2}^{PEC,R} + R_{sy,h_2}^{PEC,T}} \tag{8}$$

2.3 VALIDATIONS

After calculating the resistances of four smooth planes (R_{t1}, R_{t2}, R_{r1}, R_{r2}), four independent surface roughness corrections factors can be easily taken into account. By inserting (7) into (4), the resistance of the stripline can be modeled as:

$$R_{se,SR} = \frac{2(K_{t1}R_{sy,h_1}^{PEC,R} + K_{r1}R_{sy,h_1}^{PEC,T})(K_{t2}R_{sy,h_2}^{PEC,R} + K_{r2}R_{sy,h_2}^{PEC,T})}{K_{t1}R_{sy,h_1}^{PEC,R} + K_{r1}R_{sy,h_1}^{PEC,T} + K_{t2}R_{sy,h_2}^{PEC,R} + K_{r2}R_{sy,h_2}^{PEC,T}} \tag{9}$$

To validate (9), using the stripline illustrated by Figure 5, three cases with rough surfaces are created using Ansys Q2D. The surface roughness is modeled using Hammerstad approach [4].

To calculate the modeled $R_{se,SR}$, the resistances contributed by different planes are determined by introducing four additional 2D models illustrated by Figure 8. The surface roughness correction factors ($K_{t1}, K_{r1}, K_{t2}, K_{r2}$) are calculated using the expression presented in Hammerstad's paper [4] (same model is used by the 2D solver).

The comparison between the modeled $R_{se,H}$ calculated using (9) and Q2D simulated $R_{se,SR}$ is shown in Figure 10. Good agreement can be achieved with the difference below 5%. The traditional modeling approach using averaged RMS roughness levels of four surfaces is presented for the third case. As can be seen, averaging roughness leads to poor agreement.

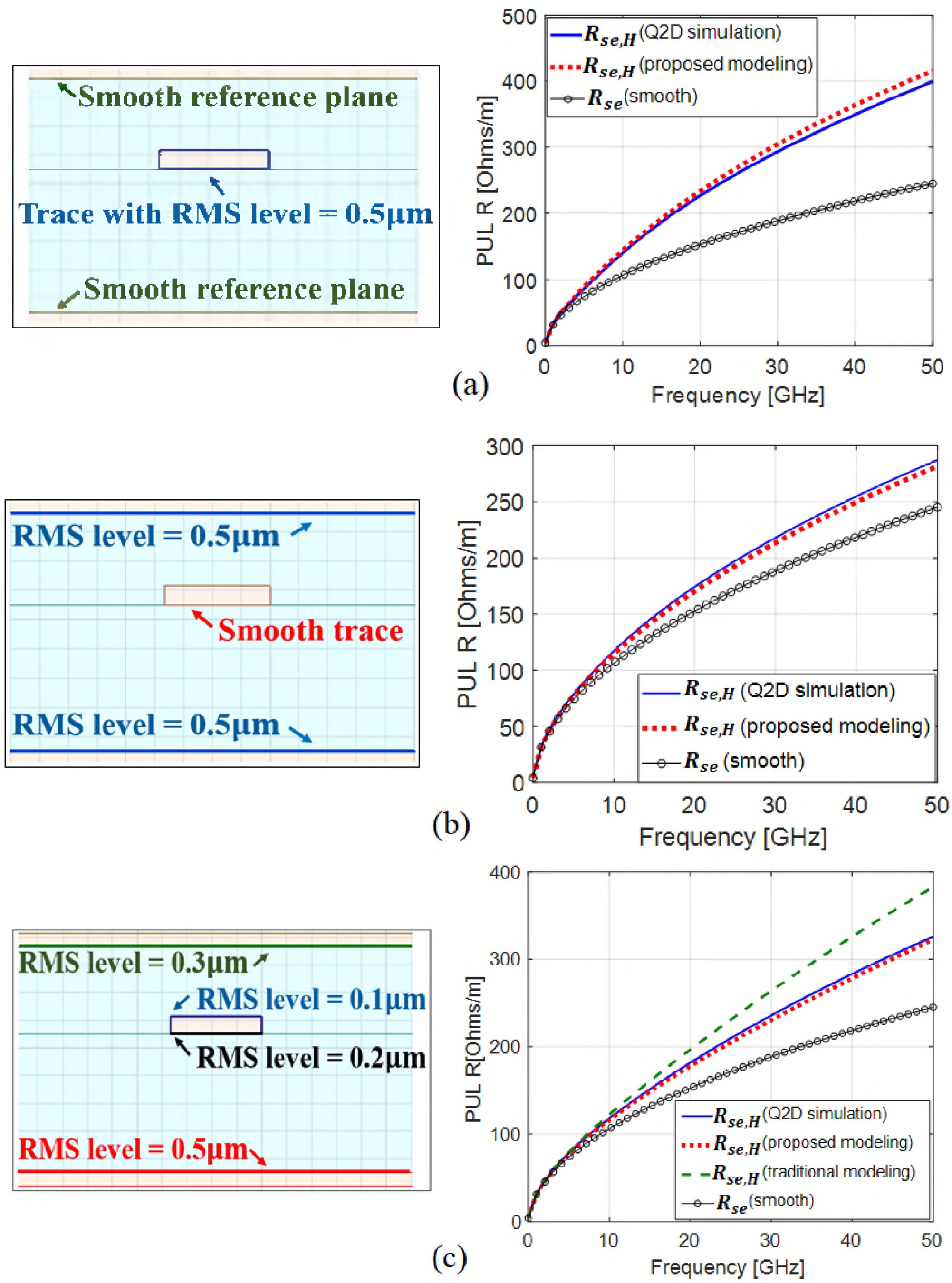

Figure 10. Three cases with rough surfaces are created. Comparison between the modeling and simulation is presented.

3. COUPLED STRIPLINES MODELING

To model the coupled stripline pair, the expressions for the single-ended stripline, (2) and (4) are extended for common and differential mode (derivation is given in the Appendix). The resistances of the stripline pair with smooth (R_m) and rough planes ($R_{m,SR}$) are expressed as:

$$R_m = \frac{2(R_{t_1,m} + R_{r_1,m})(R_{t_2,m} + R_{r_2,m})}{R_{t_1,m} + R_{r_1,m} + R_{t_2,m} + R_{r_2,m}} \tag{10}$$

$$R_{m,SR} = \frac{2(K_{t1}R_{t_1,m} + K_{r1}R_{r_1,m})(K_{t2}R_{t_2,m} + K_{r2}R_{r_2,m})}{K_{t1}R_{t_1,m} + K_{r1}R_{r_1,m} + K_{t2}R_{t_2,m} + K_{r2}R_{r_2,m}} \tag{11}$$

where, m represents the mode (common or differential). To calculate the resistances contributed by different planes, we use an idea similar to that in (7), i.e. the resistances of upper side of the trace ($R_{t1,m}$), upper reference plane ($R_{r1,m}$), lower side of the trace ($R_{t2,m}$), and lower reference plane ($R_{r2,m}$) are calculated using additional models illustrated by Figure 11. Relationship between the surface contributions and the four model resistances are given (similar to the single-ended case) by:

$$\begin{aligned} R_{t1,m} &= 2R_{sy,h1,m}^{PEC,R} \\ R_{r1,m} &= 2R_{sy,h1,m}^{PEC,T} \\ R_{t2,m} &= 2R_{sy,h2,m}^{PEC,R} \\ R_{r2,m} &= 2R_{sy,h2,m}^{PEC,T} \end{aligned} \tag{12}$$

To validate (10) the stripline pair illustrated by Figure 12 is used. The differential and common mode resistances of four planes ($R_{t1,m}, R_{r1,m}, R_{t2,m}, R_{r2,m}$) are calcaulted using four additional models illustrated by Figure 11. To validate the proposed rough surfaces modeling approach expressed by (11) on three coupled pair with different roughness on the surfaces illustrated by Figure 13, three rough cases are created.

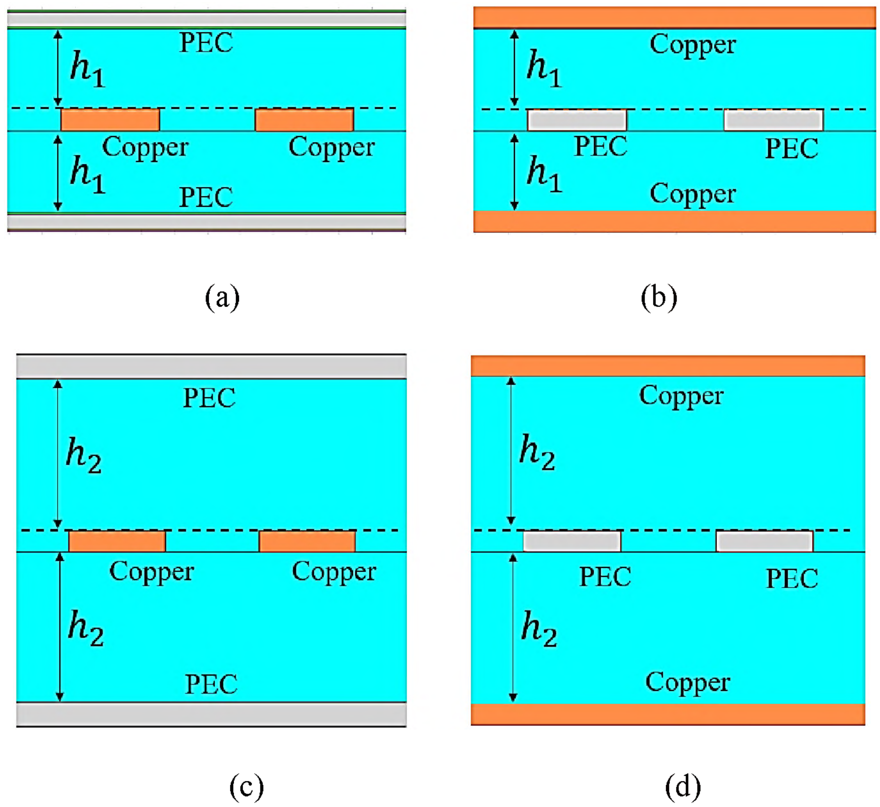

Figure 11. Four 2D models are introducted to extract resistance components. The models are created for the upper side of the trace $R_{t1,m}$ (a), upper reference plane $R_{r1,m}$ (b), lower side of the trace $R_{t2,m}$ (c), and lower reference plane $R_{r2,m}$ (d).

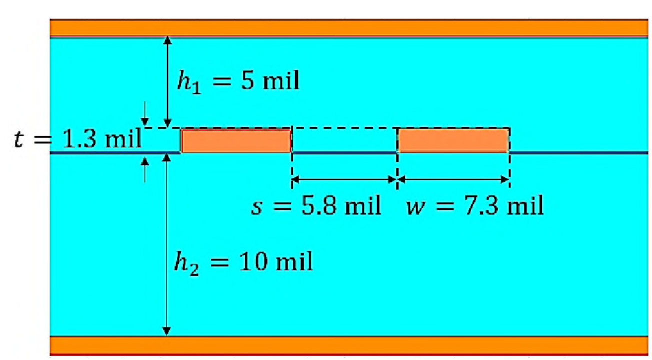

Figure 12. The cross-sectional geometry of the coupled stripline pair.

The simulated $R_{m,H}$ is calculated directly by Q2D, and modeled $R_{m,H}$ is calculated using (11) with $R_{t1,m}, R_{r1,m}, R_{t2,m}, R_{r2,m}$ obtained from (12) and $K_{t1}, K_{r1}, K_{t2}, K_{r2}$ calculated by Hammerstad model's expression.

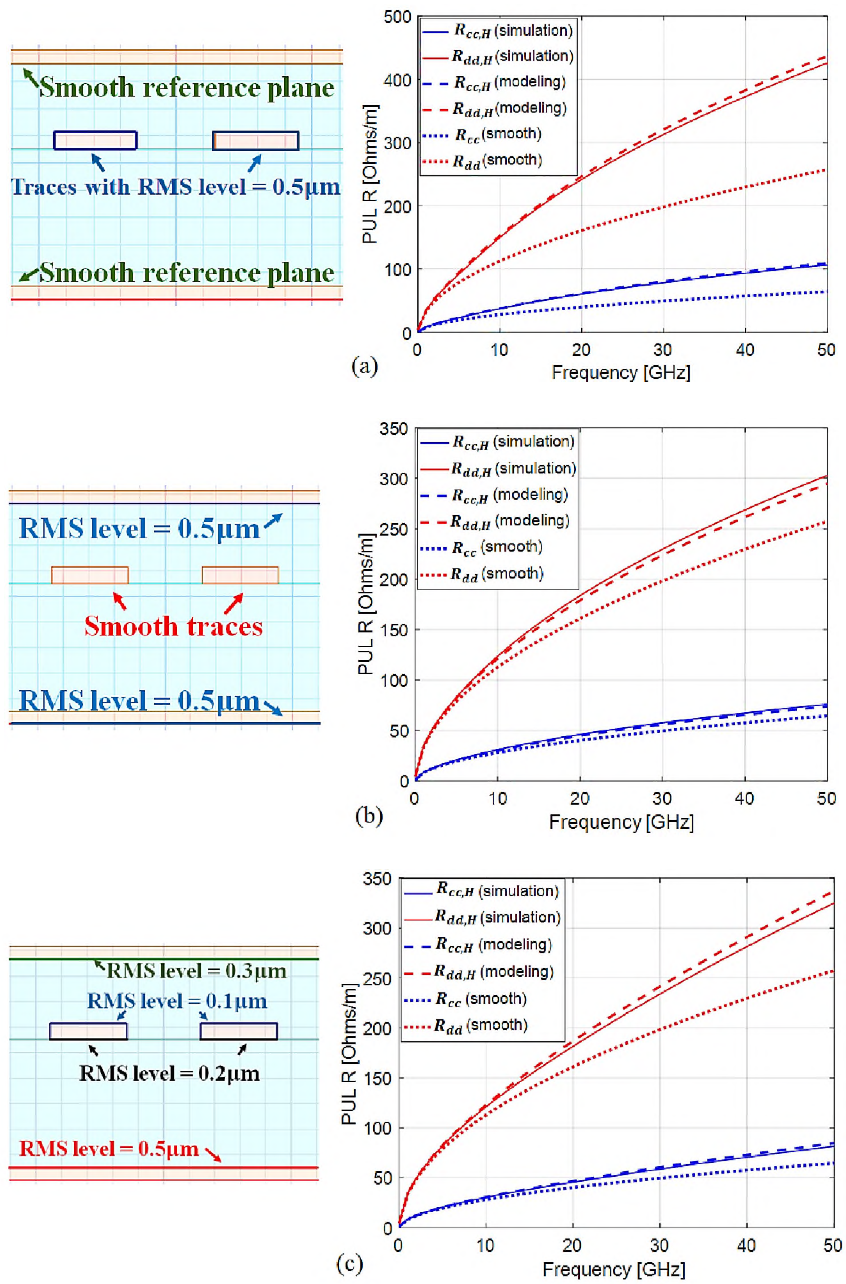

Figure 13. Three cases with rough surfaces are created. The compairiosn between the modeling and simulation is presented.

As can be seen from Figure 13 good agreement between the simulated and modelled resistances is achieved in all three cases. The validation is also performed using CST 3D models [16] presented in Figure 14 and 15. Since the dielectric substrate in the models is air, there is no dielectric loss. For practical low-loss transmission lines with $R \ll \omega L$, the attenuation factor can be calculated as: $\alpha = 0.5R\sqrt{C/L}$ [17, (2.85a)]. Thus, the attenuation factors of the 3D models with lossless dielectric material are proportional to the resistances and the surface roughness correction factors can be used to correct the attenuation factor directly.

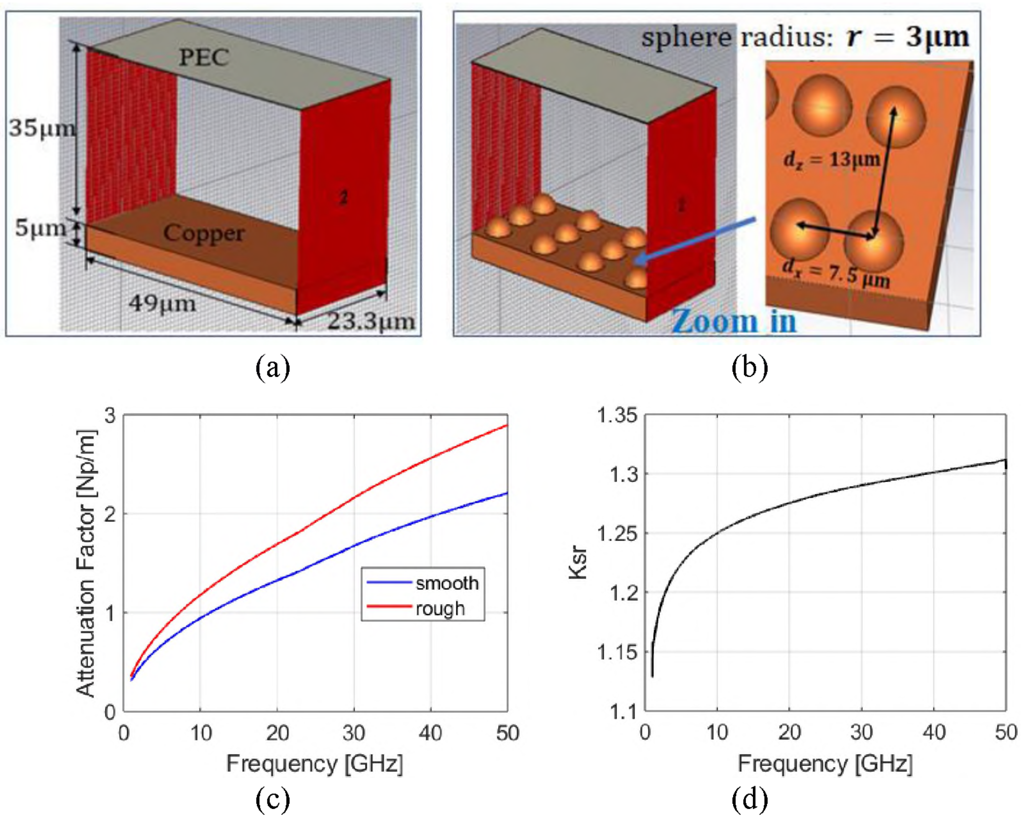

Figure 14. The striplines with rough surfaces are simulated using CST.
The 3D models with smooth (a) and rough (b) trace are created.
The attenuation factors (c) are calcualted using the simulated insertion loss.
The surface roughness correction factor (d) is the ratio of the rough
and smooth attenuation factors.

As Figure 14 and 15 illustrate, the surface roughness is modelled using the hemispheres placed on the smooth planes. The surface roughness correction factor for the rough surface is calculated using the ratio of the rough and smooth attenuation factors in the model in Figure 14. Analytical surface roughness models are not used here to avoid additional inaccuracies due to approximated correction factor. For simulation of practical PCB traces, a certain roughness model will be needed.

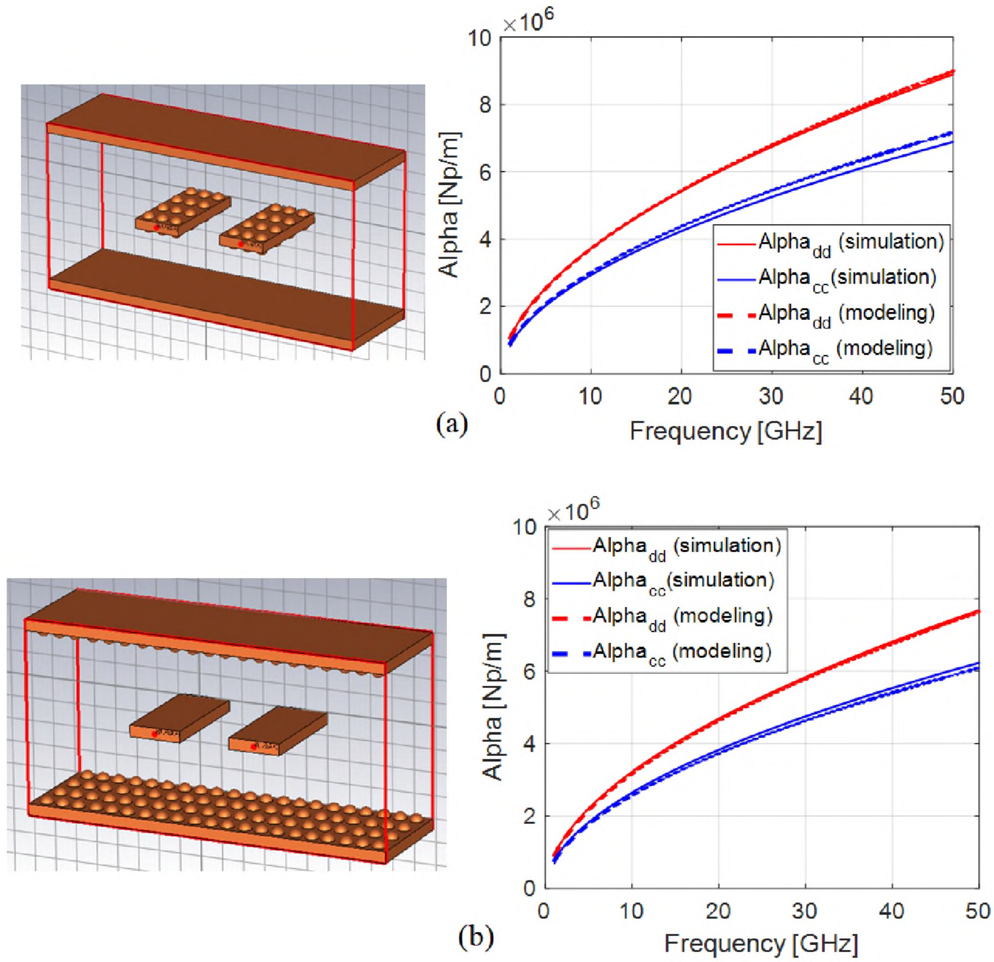

Figure 15. Compairiosn between the modeled and simulated attenuation factors. Two cases ((a) rough traces and smooth references; (b) rough references and smooth traces) with rough surfaces are created. The compairiosn between the modeled and simulated α_{cc} and α_{dd} is presented.

Two cases with rough surfaces are simulated by CST. The modeled α_m is calculated using the proposed approach by introducing four additional models. As Figure 15 shows, a good match is achieved between the simulation and the modeling results in two cases: smooth trace / rough reference planes, and rough trace / smooth reference planes.

4. CONCLUSIONS

This paper provides a more comprehensive modeling for striplines with different surface roughness on different planes compared to the traditional roughness averaging approach. The resistances contributed by the planes are calculated using four additional stripline models, and corrected by independent surface roughness correction factors accordingly. According to 2D and 3D simulation results, the total modeled resistances for single-ended and coupled striplines provide much better accuracy compared to the models with averaged roughness.

APPENDIX

The derivation of (10) for common and differential mode is shown in this section. Let us take a closer look at the current distribution of a coupled stripline pair. As Figure A-1 illustrates, the exclusive return path for the left or right trace is expressed as R_r, and the mutual return path is expressed as R_m.

When the separation between two traces (s) is infinite, there is no coupling between lines and $R_m = 0$. When the separation between two traces (s) is zero (a single ended line) no exclusive return path exists and $R_r = 0$.

The definition of PUL nodal resistance matrix (R) for balanced coupled lines is shown in (A1), and the matrix elements R_{11} and R_{21} are calculated by (A2) and (A3). As (A4) shown, matrix R can be converted to the modal (common-differential) from (R_m) by the following transformation:

$$\begin{bmatrix} V_1 \\ V_2 \end{bmatrix} = R \cdot \begin{bmatrix} I_1 \\ I_2 \end{bmatrix}, \text{where } R = \begin{bmatrix} R_{11} & R_{21} \\ R_{21} & R_{11} \end{bmatrix} \quad \text{(A1)}$$

$$\text{when } V_2 = 0,\ R_{11} = \frac{V_1}{I_1} = R_t + R_r + R_{rm} \quad \text{(A2)}$$

$$\text{when } V_1 = 0,\ R_{21} = V_2/I_1 = R_{rm} \quad \text{(A3)}$$

$$R_m = (T_v)^{-1} \cdot R \cdot T_i = \begin{bmatrix} 0.5(R_{11} + R_{21}) & 0 \\ 0 & 2(R_{11} - R_{21}) \end{bmatrix} \quad \text{(A4)}$$

$$\text{where, } T_v = \begin{bmatrix} 1 & -0.5 \\ 1 & 0.5 \end{bmatrix}; T_i = \begin{bmatrix} 0.5 & -1 \\ 0.5 & 1 \end{bmatrix}$$

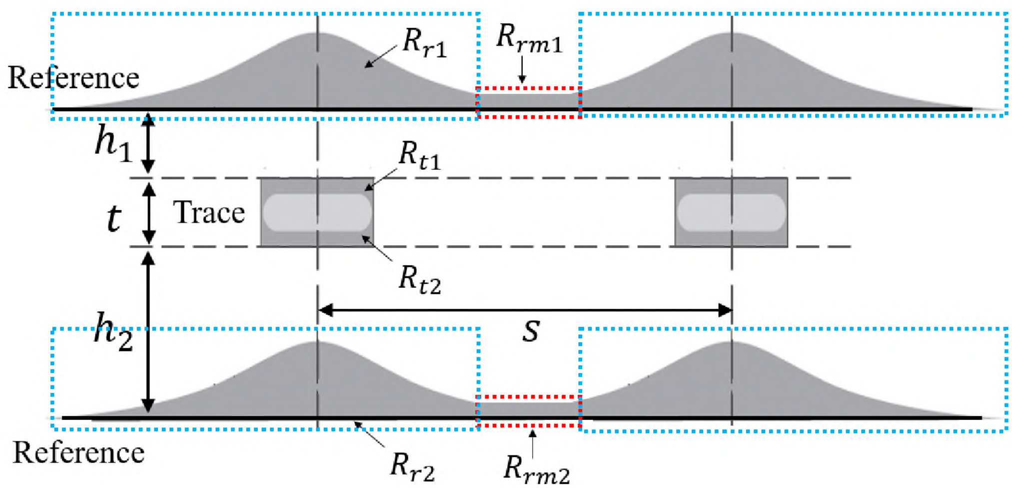

Figure A-1. Illustration of current distribution of balanced coupled striplines.

- For the differential mode, according to (A4):

$$R_{dd} = 2(R_{11} - R_{21}) = 2(R_t + R_r) \quad \text{(A5)}$$

The upper and lower portions of the stripline are in parallel. As Figure A-2(a) shown, (A5) is expanded as:

$$R_{dd} = 2[(R_{t1} + R_{r1})||(R_{t2} + R_{r2})] \quad \text{(A6)}$$

$$= 2 \cdot \frac{(R_{t1} + R_{r1}) \cdot (R_{t2} + R_{r2})}{R_{t1} + R_{r1} + R_{t2} + R_{r2}}$$

For the differential mode, the left and right portions are in series:

$$R_{t1,dd} = 2R_{t1};\ R_{r1,dd} = 2R_{r1};\ R_{t1,dd} = 2R_{t1};\ R_{t1,dd} = 2R_{t1} \quad \text{(A7)}$$

Thus, expression (A6) is converted to the same form as (10):

$$R_{dd} = 2\frac{0.5(R_{t_1,dd} + R_{r_1,dd})0.5(R_{t_2,dd} + R_{r_2,dd})}{0.5(R_{t_1,dd} + R_{r_1,dd} + R_{t_2,dd} + R_{r_2,dd})} \quad \text{(A8)}$$

$$= \frac{(R_{t_1,dd} + R_{r_1,dd})(R_{t_2,dd} + R_{r_2,dd})}{R_{t_1,dd} + R_{r_1,dd} + R_{t_2,dd} + R_{r_2,dd}}$$

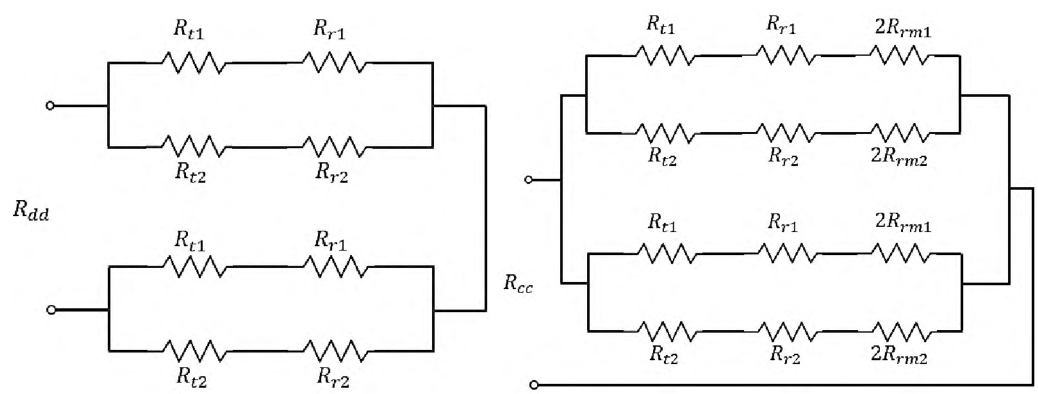

(a) (b)

Figure A-2. The equivlent stripline resistance circuit for differentail mode (a) and common mode (b).

- For the common mode, according to (A4):

$$R_{cc} = 0.5(R_{11} + R_{21}) = 0.5(R_t + R_r + 2R_{rm}) \quad \text{(A9)}$$

The upper portion and lower portion are in parallel. As Figure A-2(b) shown, (A9) is expanded as:

$$R_{cc} = 0.5[(R_{t1} + R_{r1} + 2R_{rm1})||(R_{t2} + R_{r2} + 2R_{rm2})] \quad \text{(A10)}$$

$$= 0.5 \cdot \frac{(R_{t1} + R_{r1} + 2R_{rm1}) \cdot (R_{t2} + R_{r2} + 2R_{rm2})}{R_{t1} + R_{r1} + 2R_{rm1} + R_{t2} + R_{r2} + 2R_{rm2}}$$

- For the common mode, the left and right portions are in parallel:

$$\begin{aligned} R_{t1,cc} &= 0.5R_{t1};\ R_{r1,cc} = 0.5(R_{r1} + 2R_{rm1}) \\ R_{t2,cc} &= 0.5R_{t1}; R_{r2,cc} = 0.5(R_{r2} + 2R_{rm2}) \end{aligned} \quad \text{(A11)}$$

Expression (A10) is the same form as (10):

$$R_{cc} = 0.5\frac{(2R_{t_1,cc} + 2R_{r_1,cc})(2R_{t_2,cc} + 2R_{r_2,cc})}{2(R_{t_1,cc} + R_{r_1,cc} + R_{t_2,cc} + R_{r_2,cc})} \quad \text{(A12)}$$

$$= \frac{(R_{t_1,cc} + R_{r_1,cc})(R_{t_2,cc} + R_{r_2,cc})}{R_{t_1,cc} + R_{r_1,cc} + R_{t_2,cc} + R_{r_2,cc}}$$

Thus, (10) is derived by combining (A8) and (A12).

REFERENCES

[1] X. Guo, H. Gao, G. Shen, Q. Liu, V. Khilkevich, J. Drewniak, S. De, S. Hinaga, D. Yanagawa, “Design methodology for behavioral surface roughness model”, in Proc. IEEE Int. Symp. EMC, Ottawa, 2016, pp. 927-931

[2] S. Yong, V. Khilkcvich, Y. Liu, H. Gao, S. Hinaga, S. De, D. Yanagawa, J. Drewniak, "Dielectric Loss Tangent Extraction Using Modal Measurements and 2-D Cross-Sectional Analysis for Multilayer PCBs," in IEEE Trans. Electromagn. Compat., Early Access

[3] S. Yong, Y. Liu, H. Gao, B. Chen, S. De, S. Hinaga, D. Yanagawa, J. Drewniak, V. Khilkcvich, “Dielectric Dissipation Factor (DF) Extraction Based on Differential Measurements and 2-D Cross-sectional Analysis”, in Proc. IEEE Int. Symp. EMC, Long Beach, CA, USA, 30 Jul-3, 2018, pp. 217-222.

[4] E. Hammerstad and O. Jensen, "Accurate Models for Microstrip Computer-Aided Design," in IEEE MTT-S Intl. Microwave Symposium Digest, Washington, DC, 1980.

[5] S. Hall, S. G. Pytel, P. G. Huray, D. Hua, A. Moonshiram, G. A. Brist, and E. Sijercic “Multigigahertz Causal Transmission Line Modeling Methodology Using a 3-D Hemispherical Surface Roughness Approach”, IEEE Trans. Microw. Theory Tech., vol. 55, no. 12, Dec. 2007, pp. 2614 – 2624

[6] M. B. Griesi, ‘Characterization of Electrodeposited Copper Foil Surface Roughness for Accurate Conductor Power Loss Modeling’, Scholar Commons (Master’s thesis, 2014). Retrieved from: http://scholarcommons.sc.edu/etd/2958

[7] P. G. Huray, O. Oluwafemi, J. Loyer, E. Bogatin, X. Ye, “Impact of Copper Surface Texture on Loss: A Model that Works”, DesignCon 2010

[8] Y. Chu, “Method for modeling conductor surface roughness”, US Patent#8527246.

[9] Y. Shlepnev, “Unified approach to interconnect conductor surface roughness modelling”, in 2017 IEEE 26st Conference on Electrical Performance of Electronic Packaging and Systems (EPEPS2017), San Jose, CA

[10] G. Brist, “Design Optimization of Single-Ended and Differential Impedance PCB Transmission Lines”. Retrieved from: https://www.jlab.org/eng/eecad/pdf/053designop.pdf

[11] Advanced Circuits Inc., ‘How to Build a Printed Circuit Board’, Retrieved from: https://www.4pcb.com/media/presentation-how-to-build-pcb.pdf

[12] M. Y. Koledintseva, T. Vincent, A. C. Scogna, S. Hinaga, “Method of Effective Roughness Dielectric in a PCB: Measurement and Full-Wave Simulation Verification”, IEEE Trans. Electromagn. Compat., vol.57, no.4, Aug. 2015. pp.807-814

[13] A. V. Rakov, S. De, M. Y. Koledintseva, S. Hinaga, J. L. Drewniak, R. J. Stanley, “Quantification of Conductor Surface Roughness Profiles in Printed Circuit Boards”, IEEE Trans. Electromagn. Compat., vol.57, no.2, April. 2015. pp.264-273

[14] S. Hall and H. Heck, “Advanced Signal Integrity for High-Speed Digital Designs”, Wiley-IEEE press, 2009.

[15] ANSYS, Inc., ANSYS Electronics Desktop Online Help – 2D Extractor (2018 release), Canonsburg, PA, USA, 2018

[16] CST Studio Suite 2018 Web Help. Retrieved from: www.cst.com

[17] D. M. Pozar, Microwave Engineering, 4th ed. Wiley, Hoboken, NJ, USA.

III. PREPREG AND CORE DIELECTRIC PERMITTIVITY EXTRACTION FOR FABRICATED STRIPLINES' FAR-END CROSSTALK MODELING

ABSTRACT

As data rate and density of digital high-speed systems are getting higher, far-end crosstalk (FEXT) noise becomes one of the major issues that limit signal integrity performance. It was commonly believed that FEXT would be eliminated for striplines routed in a homogeneous dielectric, but in reality FEXT can always be measured in striplines on fabricated printed circuit boards (PCB). A slightly different dielectric permittivity ($\boldsymbol{\varepsilon_r}$) of prepreg and core may be one of the major contributors to the FEXT. This paper is focusing on providing a practical FEXT modeling methodology for striplines by introducing an approach to extract $\boldsymbol{\varepsilon_r}$ of prepreg and core. Using known cross-sectional geometry and measured S-parameters of the coupled stirpline, the capacitance components in prepreg and core are separated using a 2D solver, and the $\boldsymbol{\varepsilon_r}$ of prepreg and core is determined.

Keywords: Far-end Crosstalk (FEXT), Stripline, Dielectric material, Transmission-line theory.

1. INTRODUCTION

As digital systems are moving in the direction of faster data transmission rate and higher density of circuits, the problem of the far-end crosstalk (FEXT) becomes one of the major limiting factors for signal integrity performance [1-3].

The concept of FEXT due to inhomogeneous dielectric material was presented in [4-8] using microstrip line as the device under test (DUT), and the analytical crosstalk estimation formulas were derived by modal analysis. By modeling FEXT using the superposition of received even and odd mode signals on the victim line [8, Figure 4-30], it was determined that the difference in phase velocities of even and odd mode signals caused by inhomogeneous dielectric material is the root cause of FEXT. Namely, if the odd and even components of the signal arrive at the receiver end at different times the 180-degree phase shift between them is no longer present and FEXT is generated.

Inhomogeneous dielectric material is almost unavoidable in fabricated multi-layer PCB due to the different glass fiber weave/content in prepreg and core, prepreg melting during lamination, epoxy resin properties tolerances, etc. [9-12]. Engineers may measure noticeable FEXT on striplines, and meet difficulties in FEXT modeling due to the unknown dielectric permittivity of prepreg and core.

Recently, several dielectric material properties extraction methods [13-16] and FEXT models [17-19] for fabricated striplines were proposed, however all of them assumed a perfectly homogeneous dielectric material. In one of the models a new concept called FEXT-due-to-lossy-conductors was proposed, which can be one of the major FEXT contributors in high-speed striplines. As [18] shown, the proximity effect due to lossy conductors causes different per-unit-length resistances, and hence attenuations for even and odd modes, leading to FEXT due to superposition of the received even and odd mode signals with different rise times.However, as far as the authors know, there has been no published approaches for the characterization of the FEXT due to inhomogeneous dielectric material in striplines. As the examples shown in Section 4 of the article demonstrate, obvious discrepancy can be observed by comparing the measurement and modeled FEXT assuming homogeneous dielectric material.

In this article, an approach is proposed to extract the relative permittivity ε_r of prepreg and core using measured S-parameters and known cross-sectional geometry of coupled striplines. Improved modeling results will be presented by comparing measurements with modelling results obtained using the extracted dielectric parameters. As a part of the paper organization, in Section 2, the transmission line theory and analytical expressions of FEXT is shown, and the impact of inhomogeneous dielectric material on FEXT is presented using simulation. By analyzing the electric field of striplines, the simulation results are explained by a qualitative theory describing the polarity of FEXT. In Section 3, the algorithm of the prepreg and core permittivity extraction is introduced. Section 4 provides the validations by comparing the measurement data with the results of modelling using the extracted ε_r.

2. FEXT ON THE STRIPLINE WITH AN INHOMOGENEOUS DIELECTRIC

2.1 FEXT MODELING BASED ON MODAL ANALYSIS

Before describing the extraction method, we would like to define the necessary parameters. In this article, the idea of describing FEXT based on modal analysis is adopted [8]. For a pair of coupled striplines, after the aggressor signal is separated into even and odd modes, the FEXT is generated during the time interval between the arrival of the odd-mode signal and the arrival of the even-mode signal.

In other words, after the propagation of l meters, the FEXT is the superposition of the received even and odd model signals $(v_{even}(t,l), v_{odd}(t,l))$ on the victim line [8, Figure 4-30].

$$v_{fext}(t,l) = v_{even}(t,l) + v_{odd}(t,l) \tag{1}$$

Suppose that only the FEXT due to inhomogeneous dielectric exists (all other FEXT sources are neglected). Under the lossless transmission line assumption, (1) can be expressed using a function of modal phase velocities to predict the peak value of FEXT [18, Equ.3]:

$$v_{fext} = \frac{1}{2} \cdot \frac{l}{t_r} \cdot \left(\frac{1}{v_{p,odd}} - \frac{1}{v_{p,even}} \right) \cdot v_I \tag{2}$$

where v_I is the amplitude of the aggressor signal that has a rise time of t_r. The odd and even phase velocities ($v_{p,odd}$, $v_{p,even}$) can be expressed using the per-unit length (PUL) modal inductance (L_m) and capacitance (C_m):

$$v_{p,m} = (L_m C_m)^{-0.5} \tag{3}$$

here, m represents even or odd mode. L_m and C_m can be obtained by the modal transformation of the nodal inductance ($\boldsymbol{L}$) and capacitance ($\boldsymbol{C}$) matrices of a three-conductor model with symmetrical signal traces [20] [21] using Equation (4) and (5).

For the homogeneous and lossless case, the FEXT is zero due to the same phase velocity for even and odd mode signals ($v_{p,odd} = v_{p,even}$), which can be proven by using an important identity for homogeneous media $\boldsymbol{LC} = \boldsymbol{CL} = \mu\varepsilon \boldsymbol{I}_n$ [20, Equ.(3.37)].

The polarity of FEXT peak voltage can be explained by the modal analysis. Firstly, for striplines with an inhomogeneous dielectric material, the modal velocities are not equal ($v_{p,odd} \neq v_{p,even}$).

$$(\boldsymbol{T}_v)^{-1} \cdot \boldsymbol{L} \cdot \boldsymbol{T}_i = \begin{bmatrix} L_{11} + L_{21} & 0 \\ 0 & L_{11} - L_{21} \end{bmatrix} = \begin{bmatrix} L_{even} & 0 \\ 0 & L_{odd} \end{bmatrix} \quad (4)$$

$$(\boldsymbol{T}_i)^{-1} \cdot \boldsymbol{C} \cdot \boldsymbol{T}_v = \begin{bmatrix} C_{11} - |C_{21}| & 0 \\ 0 & C_{11} + |C_{21}| \end{bmatrix} = \begin{bmatrix} C_{even} & 0 \\ 0 & C_{odd} \end{bmatrix} \quad (5)$$

where, $\boldsymbol{L} = \begin{bmatrix} L_{11} & L_{21} \\ L_{21} & L_{11} \end{bmatrix}$ and $\boldsymbol{C} = \begin{bmatrix} C_{11} & -|C_{21}| \\ -|C_{21}| & C_{11} \end{bmatrix}$ (6)

$$\boldsymbol{T}_v = \boldsymbol{T}_i = \begin{bmatrix} 2^{-0.5} & -2^{-0.5} \\ 2^{-0.5} & 2^{-0.5} \end{bmatrix} \quad (7)$$

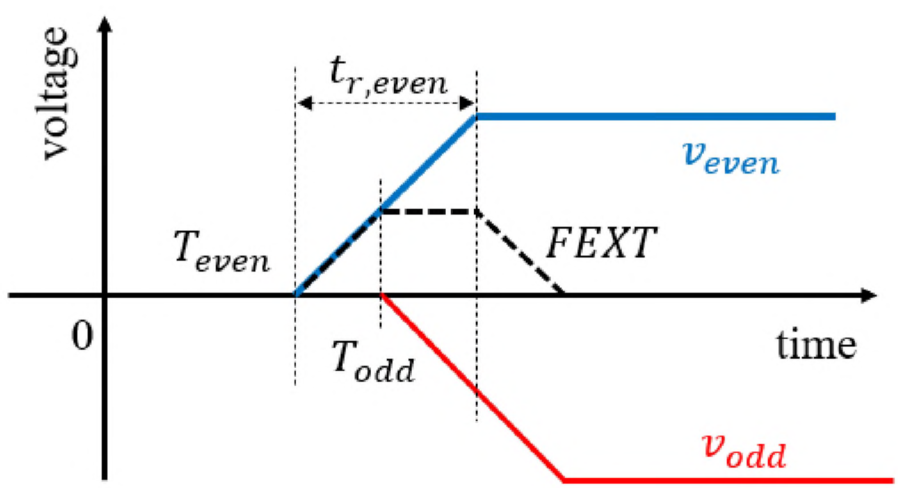

Figure 1. Illustration of FEXT when $v_{p,even} > v_{p,odd}$. v_{even} and v_{odd} stand for even and odd mode signals at the receiver end, respectively.

As Figure 1 illustrates, for the positive aggressor signal, if the even mode signal has a faster phase velocity and arrives at the receiver end earlier, the FEXT peak is positive. On the contrary, if the odd mode signal propagates faster, the FEXT peak is negative.

2.2 THE IMPACT OF THE INHOMOGENEOUS DIELECTRIC ON THE TOTAL FEXT OF STRIPLINES

The velocities $v_{p,odd}$ and $v_{p,even}$ of a pair of coupled striplines are determined by the cross-section geometry and material parameters, therefore the prepreg and core dielectric permittivity ($\varepsilon_{r,pg}$, $\varepsilon_{r,co}$) plays an important role.

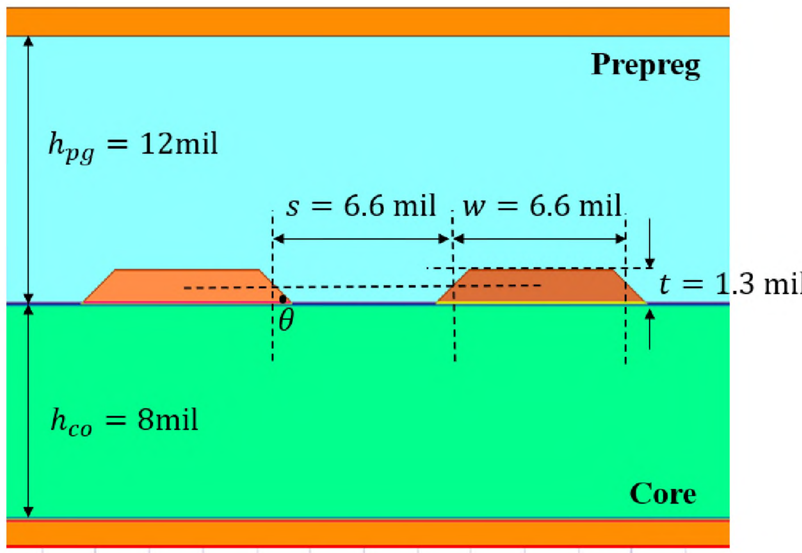

Figure 2. Cross-section geometry of two coupled symmetrical stripline traces. The upper blue block represents prepreg, and the lower green block stands for core. The etching angle θ is 45 degree.

To demonstrate FEXT's sensitivity to the prepreg and core inhomogeneity, several simulations are performed using Ansys 2D extractor [22]. We use the coupled striplines with cross-section geometry illustrated in Figure 2. The thickness of prepreg is larger than the thickness of core (h_{pg} = 12mil > h_{co} = 8mil). The line length is 10 inches, and the rise time of the aggressor signal is t_r = 35ps. The dissipation factor (tanδ) in prepreg and core is equal to 0.003. All ports are matched. As Table 1 shows, the dielectric constant in core ($\varepsilon_{r,co}$) is set to 3.4, and the dielectric constant in prepreg ($\varepsilon_{r,pg}$) is swept from 3.5 to

3.3 to investigate the impact of dielectric material inhomogeneity. The variation is approximately 10%, which is very likely to be expected for fabricated striplines [9].

Table 1. Simulation results of the striplines with copper traces and reference planes.

	#1	#2	#3	#4	#5
$\varepsilon_{r,pg}$	3.5	3.45	3.4	3.35	3.3
$\varepsilon_{r,co}$	3.3	3.35	3.4	3.45	3.5
FEXT peak value [mV]	33.3	19.9	7.3	-7.8	-21.5

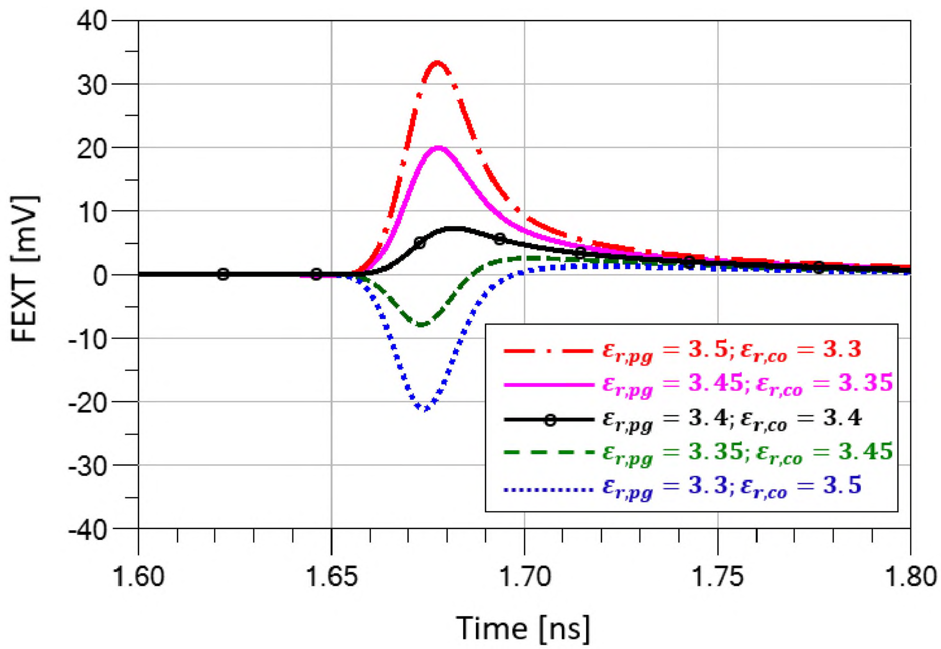

Figure 3. Comparison between the cases with swept $\varepsilon_{r,pg}$ and $\varepsilon_{r,co}$.
The striplines are with copper traces and reference planes.
The conductivity of the conductors equals to 5.8e7 S/m.

The simulation results are shown in Table 1 and Figure 3. We observe that the impact from FEXT due to inhomogeneous dielectric material is noticeable. For this case with prepreg thicker than core ($h_{pg} = 12\text{mil} > h_{co} = 8\text{mil}$), when for $\varepsilon_{r,pg} > \varepsilon_{r,co}$, the FEXT 'bump' is increased by the inhomogeneous dielectric. When $\varepsilon_{r,pg} < \varepsilon_{r,co}$, the 'dip' is introduced. As the difference between $\varepsilon_{r,pg}$ and $\varepsilon_{r,co}$ increases, the 'bump' and the 'dip' grow significantly.

The simulation data shows the necessity of obtaining $\varepsilon_{r,pg}$ and $\varepsilon_{r,co}$ to achieve accurate FEXT modeling for coupled striplines. The assumption of homogeneous dielectric can even lead to the modeled FEXT with the wrong polarity (the $\varepsilon_{r,pg}$ and $\varepsilon_{r,co}$ extraction approach will be presented in Section 3). In the following subsection, a qualitative theory is brought up to explain the simulation results which engineers can use to roughly predict the polarity of FEXT using the information of dielectric material thickness (h_{pg}, h_{co}) and permittivity ($\varepsilon_{r,pg}$, $\varepsilon_{r,co}$).

2.3 THE POLARITY OF FEXT DUE TO INHOMOGENEOUS DIELECTRIC

According to [18], when the dielectric material is homogeneous (case#3 in Figure 3 and Table 2, with $\varepsilon_{r,pg} = \varepsilon_{r,co}$), the FEXT with positive polarity can be explained because of FEXT due to lossy conductors. However, the relationship between the permittivity of prepreg and core and the polarity of FEXT needs further investigation.

To straightforwardly demonstrate FEXT due to inhomogeneous dielectric, another set of simulation is performed. The impact of FEXT due to lossy conductors is totally excluded by introducing perfect electric conductor (PEC). Compared to the simulation shown in Section 2-B, all the settings are the same except that traces and reference planes are modelled as perfect electric conductor (PEC). The results are shown in Figure 4 and Table 2. For the homogeneous dielectric case (*3), FEXT is equal to zero since FEXT due to lossy conductors is excluded. For the inhomogeneous cases (*1, *2, *4, and *5), the noticeable 'dip' and 'bump' are exclusively due to dielectric inhomogeneity.

Table 2. Simulation results of the striplines with PEC traces and reference planes.

	*1	*2	*3	*4	*5
$\varepsilon_{r,pg}$	3.5	3.45	3.4	3.35	3.3
$\varepsilon_{r,co}$	3.3	3.35	3.4	3.45	3.5
FEXT peak value [mV]	36.5	17.7	0	-18.5	-36.3

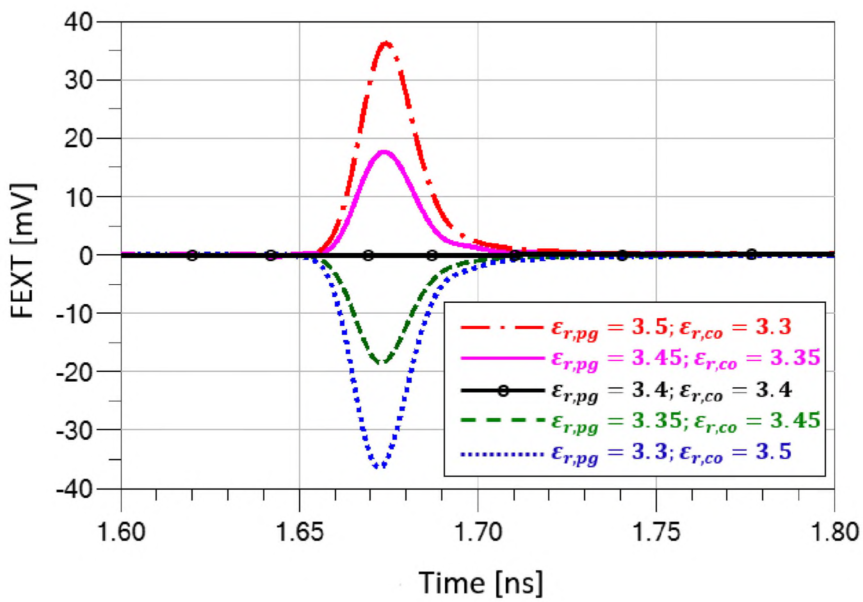

Figure 4. Comparison between the cases with swept $\varepsilon_{r,pg}$ and $\varepsilon_{r,co}$.
The striplines are with PEC traces and reference planes.

To provide explanations to the simulation results, first let's take a look at the expression of FEXT due to inhomogeneous dielectric shown in (2). To describe the differences between $v_{p,even}$ and $v_{p,odd}$, a variable Δ_{LC} is defined:

$$\Delta_{LC} = L_{odd}C_{odd} - L_{even}C_{even} = 2(L_{11}|C_{21}| - C_{11}L_{21}) \tag{8}$$

The sign of Δ_{LC} determines the polarity of FEXT according to (2) and (3). Indeed:

- If $\Delta_{LC} > 0$: $v_{p,odd} < v_{p,even}$ and FEXT is positive.
- If $\Delta_{LC} < 0$: $v_{p,odd} > v_{p,even}$ and FEXT is negative.

To determine the influence of prepreg and core on Δ_{LC}, we use the idea presented in [23] and analyze the capacitance components. According to Figure 5 [23, Figure 2], there are four categories of the per-unit-length capacitances in striplines:

1) C_f: fringe capacitance on the outer side of the trace, contributed by the prepreg ($C_{f,pg}$) and core ($C_{f,co}$) regions.
2) C_p: parallel plate capacitance of the trace, contributed by the prepreg ($C_{p,pg}$) and core ($C_{p,co}$) regions.
3) C_{fg}: fringe capacitance near the gap between traces, contributed by the prepreg ($C_{fg,pg}$) and core ($C_{fg,co}$) regions.
4) C_g: mutual capacitance across the gap, contributed by the prepreg ($C_{g,pg}$) and core ($C_{g,co}$) regions.

The total capacitance in the prepreg ($C_{t,pg}$) is expressed using the capacitance components with subscript '*pg*':

$$\begin{aligned} C_{t,pg} &= C_{f,pg} + C_{p,pg} + C_{fg,pg} + C_{g,pg} \\ &= \varepsilon_{r,pg} \cdot \left(C^a_{f,pg} + C^a_{p,pg} + C^a_{fg,pg} + C^a_{g,pg}\right) \\ &= \varepsilon_{r,pg} \cdot \left(C^a_{self,pg} + C^a_{g,pg}\right) \\ &= \varepsilon_{r,pg} \cdot C^a_{t,pg} \end{aligned} \qquad (9.a)$$

where, $C^a_{self,pg} = C^a_{f,pg} + C^a_{p,pg} + C^a_{fg,pg}$. This capacitance can be estimated using the scaling of the capacitances in the air-filled line (denoted by the superscript '*a*') by the permittivity of the dielectric media [23]. Similarly, the total capacitance in the core ($C_{t,co}$) is expressed:

$$\begin{aligned} C_{t,co} &= C_{f,co} + C_{p,co} + C_{fg,co} + C_{g,co} \\ &= \varepsilon_{r,co} \cdot \left(C^a_{f,co} + C^a_{p,co} + C^a_{fg,co} + C^a_{g,co}\right) \\ &= \varepsilon_{r,co} \cdot \left(C^a_{self,co} + C^a_{g,co}\right) \\ &= \varepsilon_{r,co} \cdot C^a_{t,co} \end{aligned} \tag{9.b}$$

where, $C^a_{self,co} = C^a_{f,co} + C^a_{p,co} + C^a_{fg,co}$.

Thus, the self-capacitance in the nodal capacitance matrix can be expressed as:

$$\begin{aligned} C_{11} &= C_{t,pg} + C_{t,co} \\ &= \varepsilon_{r,pg} \cdot \left(C^a_{self,pg} + C^a_{g,pg}\right) + \varepsilon_{r,co} \cdot \left(C^a_{self,co} + C^a_{g,co}\right) \\ &= \varepsilon_{r,pg} \cdot C^a_{t,pg} + \varepsilon_{r,co} \cdot C^a_{t,co} \end{aligned} \tag{10}$$

The mutual-capacitance in the nodal capacitance matrix:

$$|C_{21}| = C_{g,pg} + C_{g,co} = \varepsilon_{r,pg} \cdot C^a_{g,pg} + \varepsilon_{r,co} \cdot C^a_{g,co} \tag{11}$$

According to [23, Equ.14] [24, Equ. 14], the self-inductance and mutual-inductance can be estimated using capacitances of the air-filled line as:

$$L_{11}[nH/cm] \approx \frac{10C^a_{11}}{9\Delta C^a} = \frac{10(C^a_{t,pg} + C^a_{t,co})[pF/cm]}{9\Delta C^a[(pF/cm)^2]} \tag{12}$$

$$L_{21}[nH/cm] \approx \frac{10|C^a_{21}|}{9\Delta C^a} = \frac{10(C^a_{g,pg} + C^a_{g,co})[pF/cm]}{9\Delta C^a[(pF/cm)^2]} \tag{13}$$

where $\Delta C^a = (C^a_{11})^2 - (C^a_{21})^2$. For typical edge-coupled striplines $\Delta C^a > 0$. Next, let's calculate Δ_{LC} defined by (7) using the L and C given by (10)-(13):

$$\Delta_{LC} = \frac{10}{9\Delta C^a}(\varepsilon_{r,pg} - \varepsilon_{r,co})(C^a_{t,pg}C^a_{g,co} - C^a_{t,co}C^a_{g,pg}) \tag{14}$$

According to [25, Equ (6), Figure 3, Figure 5], reducing dielectric layer thickness leads to an increase in total capacitance when the ratio of trace spacing to dielectric thickness is within the range from 0.02 to 1.5. Assuming this condition is true we get:

$$\begin{aligned} C_{t,pg}^{a} > C_{t,co}^{a}, \text{when } h_{pg} < h_{co} \\ C_{t,pg}^{a} < C_{t,co}^{a}, \text{when } h_{pg} > h_{co} \end{aligned} \tag{15}$$

In addition, according to [25, Figure 4] and [26, Equ. 5], reducing dielectric thickness leads to a reduction in mutual-capacitance when the ratio of trace spacing to dielectric thickness is within the range from 0.02 to 1.5, therefore

$$\begin{aligned} C_{g,pg}^{a} < C_{g,co}^{a}, \text{when } h_{pg} < h_{co} \\ C_{g,pg}^{a} > C_{g,co}^{a}, \text{when } h_{pg} > h_{co} \end{aligned} \tag{16}$$

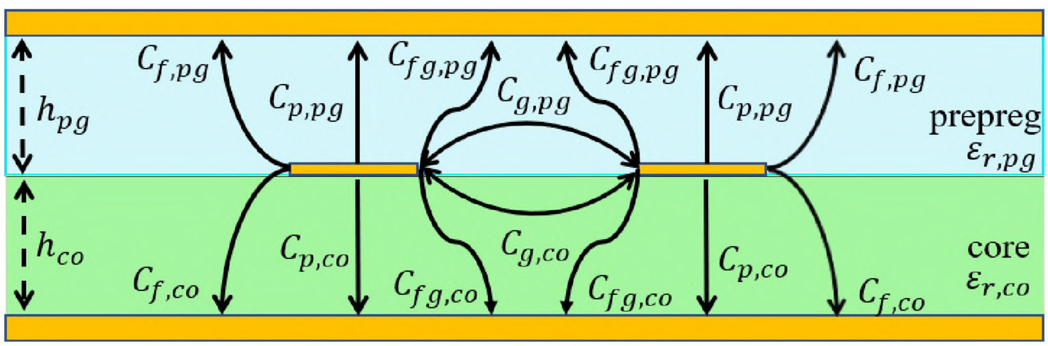

Figure 5. Illustration of the capacitance components for the coupled striplines [23]. The prepreg and core dielectric heights are h_{pg} and h_{co}. The dielectric constant in prepreg and core are $\varepsilon_{r,pg}$ and $\varepsilon_{r,co}$.

According to (15) and (16), the third term in (14) subjects to the following conditions:

$$\begin{aligned} C_{t,pg}^{a} \cdot C_{g,co}^{a} - C_{g,pg}^{a} \cdot C_{t,co}^{a} > 0, \quad \text{when } h_{pg} < h_{co} \\ C_{t,pg}^{a} \cdot C_{g,co}^{a} - C_{g,pg}^{a} \cdot C_{t,co}^{a} < 0, \quad \text{when } h_{pg} > h_{co} \end{aligned} \tag{17}$$

This rule-of-thumb has a good correlation to the simulation data shown in Table 1-2 and Figure 3-4. The prediction is generally good when the differences between h_{pg} and h_{co}, as well as $\varepsilon_{r,pg}$ and $\varepsilon_{r,co}$ are large enough.

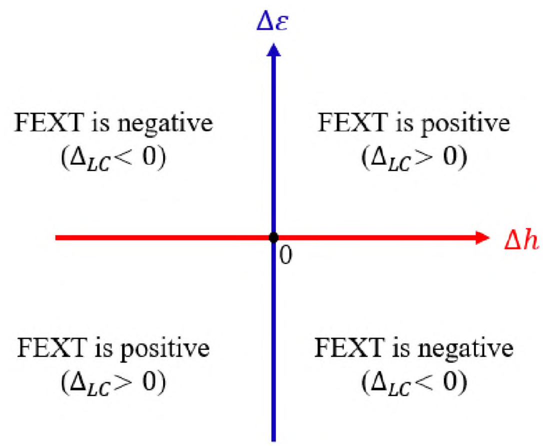

Figure 6. The polarity of FEXT-due-to-inhomogeneous-dielectric can be estimated using dielectric height and permittivity. Here, $\Delta h = h_{pg} - h_{co}$ and $\Delta\varepsilon = \varepsilon_{r,pg} - \varepsilon_{r,co}$

Thus, by taking both (17) and (14) into account, the polarity of FEXT can be roughly estimated using Figure 6:

- When the thicker dielectric layer has a lower permittivity, FEXT is negative.
- When the thicker dielectric layer has a higher permittivity, FEXT is positive.

3. PREPREG AND CORE DIELECTRIC PERMITTIVITY EXTRACTION

3.1 THE EXTRACTION METHODOLOGY

Using the qualitative theory in Figure 6, engineers can estimate the polarity of FEXT on striplines using cross-sectional geometry and nominal dielectric material information. However, as the simulation results in Table 1 and Figure 3-4 demonstrate, FEXT is very sensitive to the difference in core and prepreg permittivities, and the nominal values of $\varepsilon_{r,pg}$ and $\varepsilon_{r,co}$ may not be known with enough precision to achieve accurate modeling of FEXT considering that the PCB fabrication process may impact the dielectric properties. In this section, the authors will introduce the core and prepreg permittivity extraction methodology using measured S-parameters and known cross-sectional geometry of a pair of coupled striplines.

For a pair of coupled striplines, suppose the propagation constants of the common and differential modes are known (measured):

$$\gamma_{\{cc,dd\}} = \alpha_{\{cc,dd\}} + \beta_{\{cc,dd\}} \tag{18}$$

Here, the real part of the propagation constant is the attenuation factor ($\alpha_{\{cc,dd\}}$), while the imaginary part is the phase constant ($\beta_{\{cc,dd\}}$).

The phase constant can be obtained from measured de-embedded transmission coefficient as:

$$\beta_{\{cc,dd\}} = \left|\arg S_{\{cc,dd\}21}\right|/l \tag{19}$$

The propagation constants are related to the PUL parameters of the modes as:

$$\gamma_{\{cc,dd\}} = \sqrt{\left(R_{\{cc,dd\}} + j\omega L_{\{cc,dd\}}\right)\left(G_{\{cc,dd\}} + j\omega C_{\{cc,dd\}}\right)} \tag{20}$$

Since all practical lines are low-loss, that is $R \ll \omega L$ and $G \ll \omega C$, (20) can be approximated using the Taylor series expansion, and the phase can be estimated [27, (2-85b)] as:

$$\beta_{\{cc,dd\}} \approx \omega \cdot \sqrt{L_{\{cc,dd\}} \cdot C_{\{cc,dd\}}} \tag{21}$$

Thus, the modal capacitances can be obtained by using the measured phase constant $\beta_{\{cc,dd\}}$ and the modal per-unit-length inductance $L_{\{cc,dd\}}$ calculated using a 2D solver for the air-filled line (this assumes that the inductance is not affected by the dielectric):

$$\begin{aligned} C_{cc} &= (\beta_{cc}/\omega)^2 \cdot {L_{cc}}^{-1} \\ C_{dd} &= (\beta_{dd}/\omega)^2 \cdot {L_{dd}}^{-1} \end{aligned} \tag{22}$$

According to the common and differential modal definition given in [20] [21]:

$$C_{cc} = 2 \cdot C_{even} = 2(C_{11} - |C_{21}|) \tag{23.a}$$

$$C_{dd} = 0.5 \cdot C_{odd} = 0.5(C_{11} + |C_{21}|) \tag{23.b}$$

By inserting (10) and (12) into (23), the relationship between $C_{cc,dd}$ and the permittivity of prepreg and core is expressed as:

$$C_{cc} = 2\left(\varepsilon_{r,pg} \cdot C^a_{self,pg} + \varepsilon_{r,co} \cdot C^a_{self,co}\right) \tag{24.a}$$

$$C_{dd} = 0.5\left[\varepsilon_{r,pg}\left(C^a_{self,pg} + 2 \cdot |C^a_{g,pg}|\right) + \varepsilon_{r,co}\left(C^a_{self,co} + 2 \cdot |C^a_{g,co}|\right)\right] \tag{24.b}$$

By solving the system of equations (24.a) and (24.b), the permittivity of prepreg and core can be obtained:

$$\varepsilon_{r,co} = \frac{0.5 \cdot C_{cc} \cdot (C^a_{self,pg} + 2|C^a_{g,pg}|) - 2 \cdot C_{dd} \cdot C^a_{self,pg}}{C^a_{self,co}(C^a_{self,pg} + 2|C^a_{g,pg}|) - C^a_{self,pg}(C^a_{self,co} + 2|C^a_{g,co}|)} \tag{25.a}$$

$$\varepsilon_{r,pg} = \frac{0.5 \cdot C_{cc} \cdot (C^a_{self,co} + 2|C^a_{g,co}|) - 2 \cdot C_{dd} \cdot C^a_{self,co}}{C^a_{self,pg}(C^a_{self,co} + 2|C^a_{g,co}|) - C^a_{self,co}(C^a_{self,pg} + 2|C^a_{g,pg}|)} \tag{25.b}$$

Here, with the measured phase (19), the modal capacitances C_{cc} and C_{dd} can be obtained using (22). Thus, if the capacitance components $C^a_{g,pg}$, $C^a_{self,pg}$, $C^a_{g,co}$, $C^a_{self,co}$ are calculated, the permittivity of prepreg and core will be available as (25) shows. In addition, (25) proves that $\varepsilon_{r,co}$ and $\varepsilon_{r,pg}$ are the unique solutions of known measured phase and cross-sectional geometry information.

In order to use (25) on practice, the capacitance components in core and prepreg regions need to be calculated. To achieve this two additional 2D models with air dielectric material are created using known cross-sectional geometry. As Figure 7 (a) illustrates, the additional model-A is created using the exact geometry of the coupled striplines. The self and mutual capacitances (C_{11}^{A}, $|C_{21}^{A}|$) of this model are calculated by the 2D solver. By setting $\varepsilon_{r,pg} = \varepsilon_{r,co} = 1$, (10) and (11) are modified to describe $C_{11}^{A}$and $|C_{21}^{A}|$:

$$C_{11}^{A} = C_{self,pg}^{a} + C_{self,co}^{a} + C_{g,pg}^{a} + C_{g,co}^{a} \quad (26)$$

$$|C_{21}^{A}| = C_{g,pg}^{a} + C_{g,co}^{a} \quad (27)$$

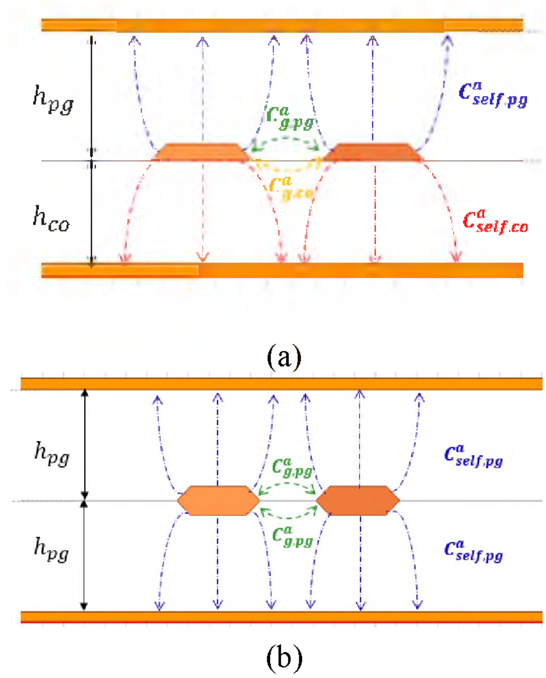

Figure 7. Two additional 2D air-filled models proposed for the capacitance calculation. Model-A (a) is repeating the actual geometry, and model-B (b) is a vertically mirrored prepreg layer.

As Figure 7(b) shows, the additional model-B is vertically balanced, with the geometry of prepreg flipped down to substitute the lower portion of the original transmission line. The capacitances in the upper portion and lower portion are the same due to symmetry. On the other hand, since the top part of both models are identical, we can reasonably assume that the $C_{g,pg}^{a}$ is equal for both models as well.

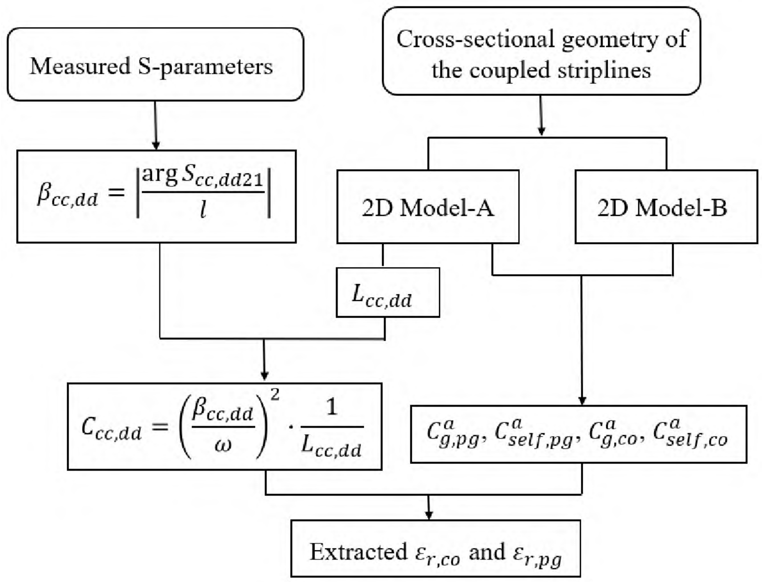

Figure 8. The flow chart of the proposed $\varepsilon_{r,pg}$ and $\varepsilon_{r,co}$ extraction method

Thus, by replacing the $C_{g,co}^{a}$ with$C_{g,pg}^{a}$in (26) and (27), the capacitance components of model-B can be expressed as:

$$C_{11}^{\mathrm{B}} = 2 \cdot C_{self,pg}^{a} + 2 \cdot C_{g,pg}^{a} \tag{28}$$

$$\left|C_{21}^{\mathrm{B}}\right| = 2 \cdot C_{g,pg}^{a} \tag{29}$$

$$C_{g,pg}^{a} = 0.5 \cdot \left|C_{21}^{\mathrm{B}}\right| \tag{30}$$

$$C_{self,pg}^{a} = 0.5 \cdot (C_{11}^{\mathrm{B}} - \left|C_{21}^{\mathrm{B}}\right|) \tag{31}$$

$$C_{g,co}^{a} = \left|C_{21}^{\mathrm{A}}\right| - 0.5 \cdot \left|C_{21}^{\mathrm{B}}\right| \tag{32}$$

$$C_{self,co}^{a} = C_{11}^{\mathrm{A}} - \left|C_{21}^{\mathrm{A}}\right| - 0.5 \cdot \left(C_{11}^{\mathrm{B}} - \left|C_{21}^{\mathrm{B}}\right|\right) \tag{33}$$

After solving (26-29), the capacitance components needed for the permittivity extraction become available. By inserting (30-33) and (22) into (25), the permittivity of prepreg and core can be extracted. The flow chart of the extraction is shown in Figure 8.

3.2 THE VALIDATION IN SIMULATION

To illustrate the feasibility of the proposed method it is first applied to a simulated transmission line. The accuracy of $\varepsilon_{r,pg}$ and $\varepsilon_{r,co}$ extraction is investigated.

A 2-D model of the coupled stripline with the cross-sectional dimensions indicated in Figure 2 is created. Both core and prepreg are modeled according to Djordjevic model [28] with the following parameters at 1 GHz, $\varepsilon_{r,pg} = 3.4$, $\tan\delta_{pg} = 0.006$, $\varepsilon_{r,co} = 3.6$, $\tan\delta_{co} = 0.006$. The modal transmission coefficients S_{cc21} and S_{dd21} are calculated by using Ansys 2D extractor, and the obtained modal attenuation and phase constants (the latter is normalized by the frequency to reveal the nonlinear dependency of the phase on the frequency) are shown in Figure 9.

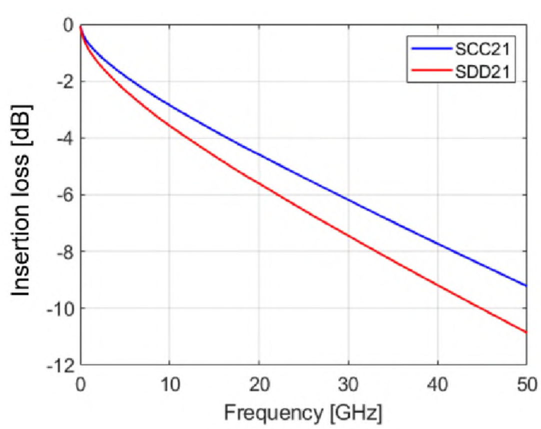

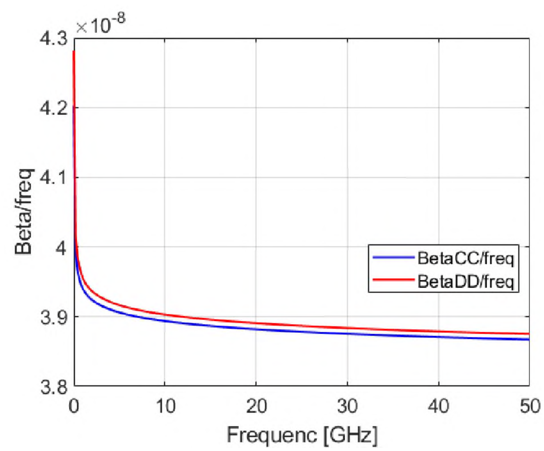

(a) (b)

Figure 9. The simulated insertion loss (a) and phase (b) of the coupled stripline. To present the frequency-dependency of phase, $\beta_{\{cc,dd\}}/f$ is presented.

The core and prepreg permittivity extractions are performed according to Figure 8 and the comparisons between the actual and extracted $\varepsilon_{r,pg}$ and $\varepsilon_{r,co}$ are shown in Figure 10. The relative error is below 2% for frequencies above 0.1 GHz. Even though the error goes up to about 10% at frequencies below 0.01 GHz due to reduced difference between β_{cc} and β_{dd} when the simulation accuracy becomes a major limiting factor, we would like to conclude that the proposed algorithm has acceptable accuracy for the bandwidth from at least 0.1 GHz to 50 GHz.

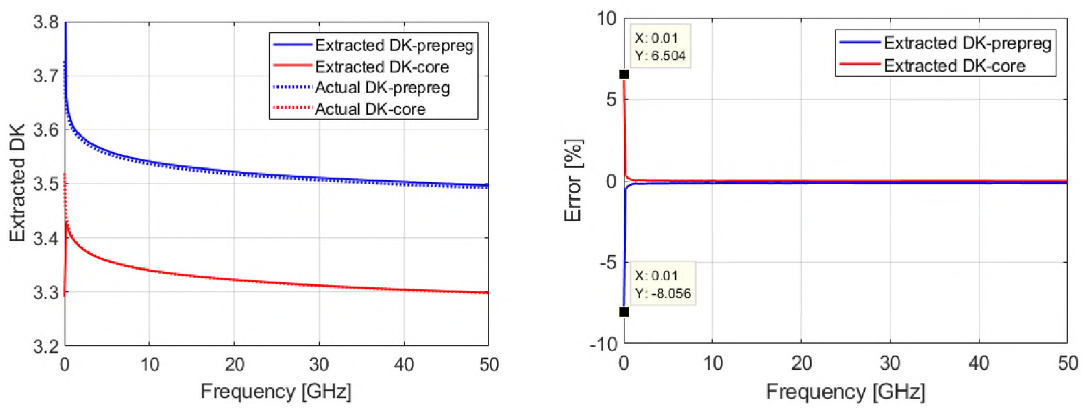

(a) (b)

Figure 10. Comparison between the actual and extracted $\varepsilon_{r,pg}$ and $\varepsilon_{r,co}$ (a). The relative extraction error is also provided (b).

4. TESTS BASED ON FABRICATED PCB

To test the proposed method, a validation board containing multiple lines was fabricated. The cables are connected to the PCB using high-precision surface mount SMA connectors. Two of the lines (1.3 inches and 15.98 inches) were used for 2x-Thru measurements [29-32]. The S-parameters measurement is performed using Keysight

N5244A 4-port Network Analyzer. The VNA calibration is performed using an electronic calibration kit N4692 up to 50GHz. The cross-section geometry of the coupled lines is presented in Figure 11. The de-embedded attenuation and phase constants are given in Fig 12.

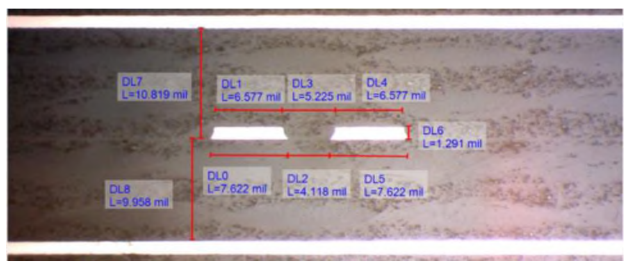

Figure 11. Cross-section of the coupled striplines.

The extracted $\varepsilon_{r,pg}$ and $\varepsilon_{r,co}$ are shown in Figure 13 plotted using solid curves. Since the extraction results are directly influenced by inaccuracies in the input parameters, slight variations can be observed in the extracted curves due to VNA measurement inaccuracies, de-embedding deficiencies [13], etc.

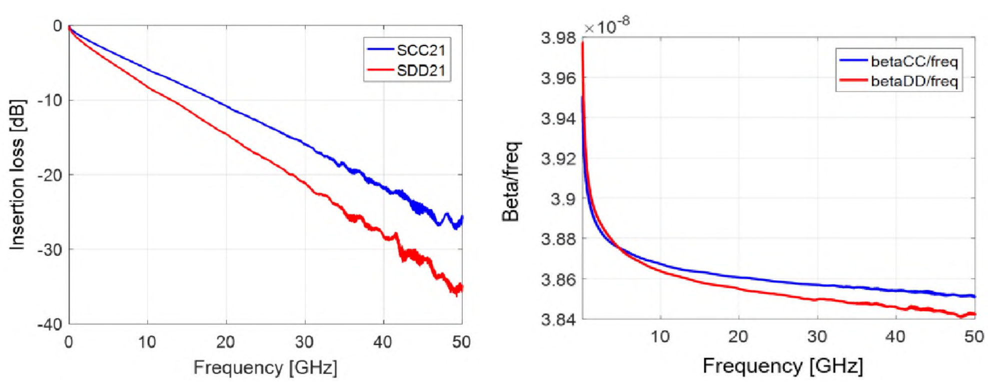

(a) (b)

Figure 12. The measured insertion loss (a) and phase (b) of the coupled stripline.

To enforce the causality of extracted $\varepsilon_{r,pg}$ and $\varepsilon_{r,co}$, which would allow using the extraction results for time-domain simulations, the Djordjevic model is used to fit the initially extracted $\varepsilon_{r,pg}$ and $\varepsilon_{r,co}$. Using the extracted $\tan\delta$ and surface roughness parameters determined for the same line in [13], a model of the transmission line with the approximated core and prepreg parameters was created and used to calculate the FEXT signal in the time domain. The comparison between modeled and measured FEXT is shown in Figure 14. The incident signal on the aggressor line has the magnitude of 1 V and the rise time of 70 ps.

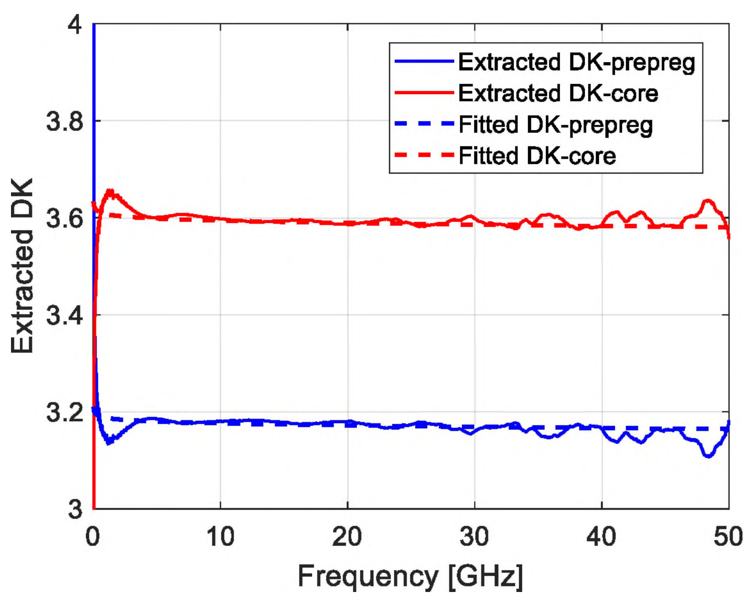

Figure 13. The initially extracted and fitted $\varepsilon_{r,pg}$ and $\varepsilon_{r,co}$. The values at 20 GHz are used to create the Djordjevic model.

For reference, a model using the effective permittivity ($\varepsilon_{r,eff} = 3.4$ @1GHz) extracted assuming a homogeneous dielectric material [13] is also used for FEXT modeling (blue dashed curve in Figure 14). By comparing the result of FEXT modeling using the homogeneous model to the measured signal it becomes obvious that the homogeneous model fails to reproduce a dip at 1.6 ns. Whereas by modeling FEXT using extracted $\varepsilon_{r,pg}$ and $\varepsilon_{r,co}$, the FEXT due to inhomogeneous dielectric material can be captured, and the dip at 1.6 ns is properly reproduced. The peak at 1.65 ns is explained by the FEXT due to the proximity effect of lossy conductor [18], and it is the major contributor to the total FEXT.

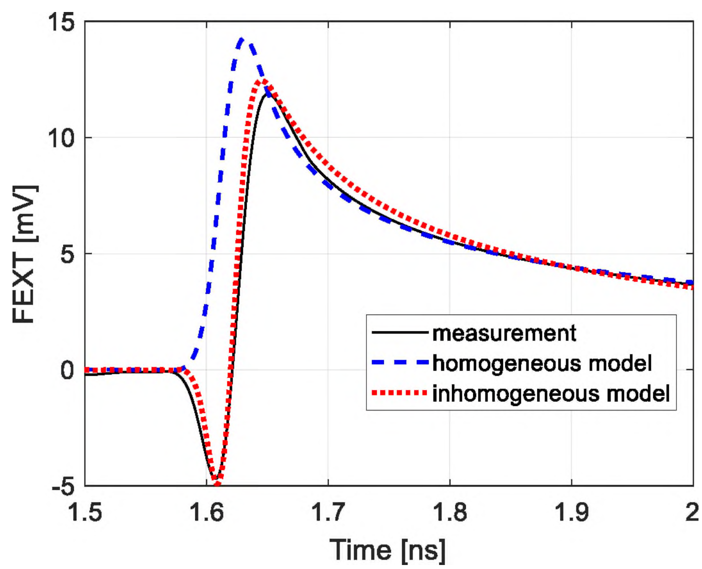

Figure 14. The comparison of the time-domain FEXT between measurement and Q2D models created using extracted $\varepsilon_{r,pg}$ and $\varepsilon_{r,co}$. The modeling using extracted $\varepsilon_{r,eff}$ assuming homogeneous dielectric material is also provided for the reference.

5. CONCLUSIONS

It was demonstrated that FEXT is very sensitive to the inhomogeneous dielectric material of striplines. Even though the mechanism of FEXT due to inhomogeneous dielectric was revealed previously for microstrip lines, there has been no methodology to analyze the inhomogeneous dielectric material of fabricated striplines.

To estimate the polarity of FEXT due to inhomogeneous dielectric material, a rule of thumb is proposed using the geometry and material information of coupled striplines. By analyzing the capacitance components in prepreg and core, a new dielectric permittivity extraction approach is proposed to characterize $\varepsilon_{r,pg}$ and $\varepsilon_{r,co}$. According to the tests based on fabricated PCB, using the extracted $\varepsilon_{r,pg}$ and $\varepsilon_{r,co}$, improved accuracy of FEXT modeling can be achieved compared to the modeling assuming homogeneous dielectric material. In the end, to provide a better overview of FEXT contributors on striplines, Table 3 is provided. Using the techniques shown in [18][19] and this article, each FEXT contributors can be characterized.

Table 3. FEXT contributors for striplines.

FEXT Contributors	Properties
Inhomogeneous dielectric material	Caused by the difference in modal components' propagation delay. The FEXT polarity is determined by geometry and inhomogeneous dielectric material.
Proximity of lossy conductors [18]	Caused by the difference in modal attenuation. The FEXT polarity is positive.
Mismatched terminals [19]	Caused by the reflection and backward coupling at the terminals. The noise is wider in time domain compared to the other two contributors.

REFERENCES

[1] B. Chen, M. Ouyang, S. Yong, Y. Wang, Y. Bai, Y. Zhou, J. Fan, "Differential integrated crosstalk noise (ICN) reduction among multiple differential BGA and Via pairs by using design of experiments (DoE) method," in Proc. IEEE Int. Symp. EMC, Washington, DC, 2017, pp. 112-117

[2] B. Chen, S. Pan, J. Wang, S. Yong, M. Ouyang and J. Fan, "Differential Crosstalk Mitigation in the Pin Field Area of SerDes Channel With Trace Routing Guidance," IEEE Trans. Electromagn Compat, vol. 61, no. 4, pp. 1385-1394, Aug. 2019.

[3] B. Chen et al., "Differential Integrated Crosstalk Noise (ICN) Mitigation in the Pin Field Area of SerDes Channel," Proc. IEEE Int. Symp. EMC, Long Beach, CA, 2018, pp. 533-537

[4] J. Eric Bracken, "Improved Formulas for Crosstalk Coefficients", DesignCon 2016

[5] C. R. Paul, "Literal solutions for time domain crosstalk on lossless transmission lines," IEEE Trans. Electromagn. Compat., vol. 34, no. 4, pp. 433–444, Nov. 1992.

[6] D. B. Jarvis, "The Effects of Interconnections on High-Speed Logic Circuits," IEEE Trans. on Electronic Computers, vol. EC-12, no. 5, pp. 476-487, 1963.

[7] W. Jiang, X-D. Cai, B. Sen, G. Wang, "Equation-Based Solutions to Coupled, Asymmetrical, Lossy, and Nonuniform Microstrip Lines for Tab-Routing Applications", IEEE Trans. Electromagn Compat, vol. 61, no. 2, pp. 548-557, April. 2019

[8] S. H. Hall, H. L. Heck, Advanced Signal Integrity for High-Speed Digital Designs. A John Wiley &. Sons, INC., 2009

[9] G. Brist, 'Design Optimization of Single-Ended and Differential Impedance PCB Transmission Lines', Intel Corp., accessed April, 2019. https://www.jlab.org/eng/eecad/pdf/053designop.pdf

[10] X. Tian, Y. Zhang, J. Lim, K. Qiu, R. Brooks, J. Zhang, J. Fan, "Numerical investigation of glass-weave effects on high-speed interconnects in printed circuit board", in Proc. IEEE Int. Symp. EMC, Raleigh, NC, USA, Aug. 4–8, 2014, pp. 475–479.

[11] D. Nozadze, A. Koul, K. Nalla, M. Sapozhnikov, V. Khilkevich, 'Effect of time delay skew on differential insertion loss in weak and strong coupled PCB traces', in Proc. of IEEE Conference on EPEPS, Oct. 15-18, 2017, San Jose, CA

[12] J. He, S. Yong, Z. Kiguradze, A. Chada, B. Mutnury and J. Drewniak, "The Effect of the Parallel-Plate Mode on Striplines in Inhomogeneous Dielectric Media," 2020 IEEE International Symposium on Electromagnetic Compatibility & Signal/Power Integrity (EMCSI), Reno, NV, USA, 2020, pp. 352-356

[13] S. Yong et al., "Dielectric Loss Tangent Extraction Using Modal Measurements and 2-D Cross-Sectional Analysis for Multilayer PCBs," IEEE Trans. Electromagn. Compat, vol. 62, no. 4, pp. 1278-1292, Aug. 2020

[14] S. Yong et al., "Dielectric Dissipation Factor (DF) Extraction Based on Differential Measurements and 2-D Cross-sectional Analysis," 2018 IEEE Symposium on Electromagnetic Compatibility, Signal Integrity and Power Integrity (EMC, SI & PI), Long Beach, CA, 2018, pp. 217-222, doi: 10.1109/EMCSI.2018.8495386.

[15] S. Jin, B. Chen, X. Fang, H. Gao, and J. Fan, "Improved 'root-omega' method for transmission-line based material property extraction for multi-layer PCBs", IEEE Trans. Electromagn. Compat., vol. 59, no. 4, pp. 1356–1367, Mar. 2017

[16] S. Yong et al., "Dielectric Material and Foil Surface Roughness Properties Extraction Based on Single-ended Measurements and Phase Constant (β) Fitting," 2020 IEEE International Symposium on Electromagnetic Compatibility & Signal/Power Integrity (EMCSI), Reno, NV, USA, 2020, pp. 346-351

[17] K. Scharff, H. Brüns and C. Schuster, "Efficient Crosstalk Analysis of Differential Links on Printed Circuit Boards Up to 100 GHz," in IEEE Transactions on Electromagnetic Compatibility, vol. 61, no. 6, pp. 1849-1859, Dec. 2019

[18] S. Yong, V. Khilkevich, X. Cai, C. Sui, B. Sen and J. Fan, "Comprehensive and Practical Way to Look at Far-End Crosstalk for Transmission Lines With Lossy Conductor and Dielectric," IEEE Trans. Electromagn. Compat., vol. 62, no. 2, pp. 510-520, April 2020

[19] S. Yong, K. Cai, B. Sen, J. Fan, V. Khilkevich, and C. Sui, "A comprehensive and practical way to look at crosstalk for transmission lines with mismatched terminals," in Proc. IEEE Int. Symp. Electromagn. Compat., Long Beach, CA, USA, 2018, pp. 538–543.

[20] C. R. Paul. Analysis of Multiconductor Transmission Lines, Second Edition, John Wiley &. Sons, Inc., 2008

[21] T. Granberg, Handbook of Digital Techniques for High Speed Design, Prentice Hall PTR, 2004.

[22] ANSYS, Inc., ANSYS Electronics Desktop Online Help – 2D Extractor (2019 release), Canonsburg, PA, USA, 2019

[23] S. S. Bedair, 'Characteristics of Some Asymmetrical Coupled Transmission Lines', IEEE Transactions on Microwave Theory and Techniques, Vol.32, No.1, 1984

[24] S. S. Bedair and I. Wolff, "Fast and accurate analytic formulas for calculating the parameters of a general broadside-coupled coplanar waveguide for (M)MIC applications," in IEEE Transactions on Microwave Theory and Techniques, vol. 37, no. 5, pp. 843-850, May 1989, doi: 10.1109/22.17450.

[25] W. J. Getsinger, "Coupled Rectangular Bars Between Parallel Plates," in IRE Transactions on Microwave Theory and Techniques, vol. 10, no. 1, pp. 65-72, January 1962

[26] S. M. Perlow, "Analysis of Edge-Coupled Shielded Strip and Slabline Structures," in IEEE Transactions on Microwave Theory and Techniques, vol. 35, no. 5, pp. 522-529, May 1987

[27] D. M. Pozar, Microwave Engineering, 4th ed. John Wiley & Sons, Inc. 2012

[28] A. R. Djordjevic, R. M. Biljic, V. D. Likar-Smiljanic, and T. K. Sarkar, "Wideband frequency-domain characterization of FR-4 and time-domain causality," IEEE Trans. Electromag. Compat, vol. 43, no. 4, pp. 662–667, Nov. 2001.

[29] Q. Huang, J. Li,1. Zhou, W. Wu, Y. Qi, and 1. Fan, "De-embedding method to accurately meas ure high-frequen cy impedance ofan O-shape spring contact", in Prac. Int. Symp. IEEE Electromagn.Campat., 2014, pp. 600-603.

[30] Y. Liu et al., "S-Parameter De-Embedding Error Estimation Based on the Statistical Circuit Models of Fixtures," in IEEE Transactions on Electromagnetic Compatibility, vol. 62, no. 4, pp. 1459-1467, Aug. 2020

[31] S. Yong et al., "A practical de-embedding error analysis method based on statistical circuit models of fixtures," in Proc. IEEE Int. Symp. Electromagn. Compat., Signal Power Integrity, New Orleans, LA, USA, 2019, pp. 45–50.

[32] B. Chen, J. He, Y. Guo, S. Pan, X. Ye, J. Fan, "Multi-Ports (2^n) 2x-Thru De-Embedding: Theory, Validation, and Mode Conversion Characterization", IEEE Trans. Electramagn. Compat., vol. 6 1, no. 4, Aug 2019.

SECTION

2. CONCLUSIONS

This dissertation presented several high-speed channel modeling techniques to achieve accurate description in dielectric complex permittivity, foil surface roughness, and FEXT waveform. The dielectric permittivity and loss tangent extraction has week sensitivity to foil surface roughness making extraction on low-loss dielectric material possible. The proposed surface roughness modeling approach can handle the striplines with different surface roughness on different planes. Using the proposed prepreg and core permittivity extraction approach, improved FEXT modeling can be achieved compared to the traditional stripline model with homognenous dielectric material. Tests and validations based on measurement data are provided to present the feasibility of the proposed techniques.

BIBLIOGRAPHY

[1] B. Pu, J. Fan and W. Nah, "Immunity Enhancement of the Power Distribution Network in Integrated Circuits With Coplanar Meander Lines in Package," in *IEEE Transactions on Electromagnetic Compatibility*, vol. 62, no. 5, pp. 2238-2246, Oct. 2020

[2] B. Pu, K. H. Kim, S. Kim and W. Nah, "Modeling and Parameter Extraction of Coplanar Symmetrical Meander Lines," in *IEEE Transactions on Electromagnetic Compatibility*, vol. 57, no. 3, pp. 375-383, June 2015

[3] B. Zhao, Z. Chen, D. Becker, "Impacts of Anisotropic Permittivity on PCB Trace and Via Modeling", 2018 *IEEE 27th Conference on Electrical Performance of Electronic Packaging and Systems (EPEPS)*, San Jose, CA, USA, Oct. 14-17, 2018, pp. 39-41.

[4] B. Zhao, S. Pan, and J. Fan. "Green's Functions in Lossy Multi-Layer Dielectrics for 3D IC/Packaging Applications." In *2018 IEEE International Conference on Computational Electromagnetics (ICCEM)*, Chengdu, China, Mar. 26-28, 2018, pp. 1-3.

[5] Y. Liu, J. Li, S. Yong, R. He and V. Khilkevich, "Scanning of random fields using blind source separation," 2019 IEEE International Symposium on Electromagnetic Compatibility, Signal & Power Integrity (EMC+SIPI), New Orleans, LA, USA, 2019, pp. 235-240

[6] J. He, S. Yong, Z. Kiguradze, A. Chada, B. Mutnury and J. Drewniak, "The Effect of the Parallel-Plate Mode on Striplines in Inhomogeneous Dielectric Media," *2020 IEEE International Symposium on Electromagnetic Compatibility & Signal/Power Integrity (EMCSI)*, Reno, NV, USA, 2020, pp. 352-356

[7] S. Yong, Y. Liu, H. Gao, B. Chen, S. De, S. Hinaga, D. Yanagawa, J. Drewniak, V. Khilkcvich, "Dielectric Dissipation Factor (DF) Extraction Based on Differential Measurements and 2 -D Cross - sectional Analysis", in *Proc. IEEE Int. Symp. EMC*, Long Beach, CA, USA, 30 Jul-3Aug, 2018. pp. 217-222.

[8] S. Yong, V. Khilkevich, S. Penugonda, X-D. Cai, Q. Gao, B. Sen, H. Gao, D. Yanagawa, D. Padilla, S. Hinaga, J. Drewniak, J. Fan, "Dielectric Material and Foil Surface Roughness Properties Extraction Based on Single-ended Measurements and Phase Constant (β) Fitting", in *Proc. IEEE Int. Symp. EMC*, 2020

[9] S. Penugonda, S. Yong, K. Cai, B. Sen, J. Fan, "Generic Modeling of Via-Stripline Structures in Multi-Layer Board for High Speed Applications" in Proc. *IEEE Int. Symp. EMC*, New Orleans, LA, USA, 22-26 July, 2019. pp. 321-326

[10] S. Penugonda, S. Yong, A. Gao, K. Cai, B. Sen and J. Fan, "Generic Modeling of Differential Striplines Using Machine Learning Based Regression Analysis," *2020 IEEE International Symposium on Electromagnetic Compatibility & Signal/Power Integrity (EMCSI)*, Reno, NV, USA, 2020, pp. 226-230

[11] S. Yong, V. Khilkcvich, Y. Liu, H. Gao, S. Hinaga, S. De, D. Padilla, D. Yanagawa, J. Drewniak, "Dielectric Loss Tangent Extraction Using Modal Measurements and 2-D Cross-sectional Analysis for Multilayer PCBs", *IEEE Transactions on Electromagnetic Compatibility*, 2020, vol. 62, no. 4, pp. 1278-1292, Aug 2020

[12] Y. Liu, S. Yong, H. Gao, S. Hinaga, D. Padilla, D. Yanagawa, J. Drewniak, V. Khilkevich, "S-Parameter De-Embedding Error Estimation Based on the Statistical Circuit Models of Fixtures", *IEEE Transactions on Electromagnetic Compatibility*, vol. 62, no. 4, pp. 1459-1467, Aug 2020

[13] S. Yong, Y. Liu, H. Gao, S. Hinaga, S. De, D. Padilla, D. Yanagawa, J. Drewniak, V. Khilkevich, "A Practical De-embedding Error Analysis Method Based on Statistical Circuit Models of Fixtures", in *Proc. IEEE Int. Symp. EMC, New Orleans*, LA, USA, 22-26 July, 2019. pp. 45-50.

[14] B. Chen et al., "Differential S-Parameter De-embedding for 8-Port Network," *2018 IEEE Symposium on Electromagnetic Compatibility, Signal Integrity and Power Integrity (EMC, SI & PI),* Long Beach, CA, 2018, pp. 52-56

[15] S. Yong et al., "A Cross-sectional Profile Based Model for Stripline Conductor Surface Roughness," *2020 IEEE International Symposium on Electromagnetic Compatibility & Signal/Power Integrity (EMCSI)*, Reno, NV, USA, 2020, pp. 334-339

[16] S. Yong et al., "Resistance Modeling for Striplines with Different Surface Roughness on the Planes," *2020 IEEE International Symposium on Electromagnetic Compatibility & Signal/Power Integrity (EMCSI)*, Reno, NV, USA, 2020, pp. 340-345

[17] Y. Guo, D. Kim, J. He, S. Yong, X. Ye, J. Fan, "Limitations of First-Order Surface Impedance Boundary Condition and Its Effect on 2D Simulations for PCB Transmission Lines" in *Proc. IEEE Int. Symp. EMC*, 2020

[18] X. Sun et al., "Causality Analyzing for Transmission Line with Surface Roughness," *2019 IEEE International Symposium on Electromagnetic Compatibility, Signal & Power Integrity (EMC+SIPI)*, New Orleans, LA, USA, 2019, pp. 516-521

[19] S. Yong, et al., "Passive Intermodulation Source Localization Based on Emission Source Microscopy", *IEEE Transactions on Electromagnetic Compatibility*, vol. 62, no. 1, pp. 266-271, Feb. 2020

[20] J. Li, J. Zhou, S. Yong, Y. Liu and V. Khilkevich, "Automatic sparse ESM scan using Gaussian process regression," *2020 IEEE International Symposium on Electromagnetic Compatibility & Signal/Power Integrity (EMCSI)*, Reno, NV, USA, 2020, pp. 671-675

[21] R. He, X. Yang, S. Yong, V. Khilkevich, D. Pommerenke, H. Aichele, M. Boettcher, P. Hillenbrand, A. Klaedtke, "Modeling Strategy for EMI filters", *IEEE Transactions on Electromagnetic Compatibility*, vol. 62, no. 4, pp. 1572-1581, Aug 2020

[22] R. He, S. A. Walunj, S. Yong, V. Khilkevich, D. Pommerenke, H. Aichele, M. Boettcher, P. Hillenbrand, A. Klaedtke, "Modelling Strategy for Film Capacitors in EMI Filters" in *Proc. IEEE Int. Symp. EMC*, New Orleans, LA, USA, 22-26 July, 2019. pp.259-265

[23] B. Chen, S. Pan, J. Wang, S. Yong, M. Ouyang, Y. S. Cao, Y. Wang, H. Deng, J. Fan "Differential Far-end and Near-end Crosstalk Mitigation in the Pin Field Area of SerDes Channel with Trace Routing Guidance", *IEEE Transactions on Electromagnetic Compatibility*, vol. 61, no. 4, pp. 1385-1394, Aug. 2019

[24] S. Yong, K. Cai, B. Sen, J. Fan, V. Khilkevich, C. Sui, "A Comprehensive and Practical Way to Look at Crosstalk for Transmission Lines with Mismatched Terminals", in *Proc. IEEE Int. Symp. EMC*, Long Beach, CA, USA, 30 Jul-3Aug, 2018. pp. 538- 543.

[25] B. Chen, M. Ouyang, S. Yong, Y. Wang, Y. Bai, Y. Zhou, J. Fan, "Integrated Crosstalk Noise (ICN) Analysis among Multiple Differential BGA and Via Pairs by Using Design of Experiments (DoE) Method," in *Proc. IEEE Int. Symp. EMC*, Washington, DC, USA, Aug. 7-11, 2017. pp. 112-117.

[26] S. Yong, V. Khilkevich, K. Cai, C. Sui, B. Sen, J. Fan, "Comprehensive and Practical Way to Look at Far-End Crosstalk for Transmission Lines with Lossy Conductor and Dielectric", *IEEE Transactions on Electromagnetic Compatibility*, vol. 62, no. 2, pp. 510-520, April 2020

[27] S. Yong, S. Penugonda, Q. Gao, X-D. Cai, B. Sen, Bo Pu, X. Ye, V. Khilkevich, D. Kim, J. Fan, 'Prepreg And Core Dielectric Permittivity (εr) Extraction for Fabricated Striplines' Far-end Crosstalk Modeling', *IEEE Transactions on Electromagnetic Compatibility*, to be submitted

[28] S. Yong, Y. Liu, Y. Guo, J. He, V. Khilkevich, A. Luoh, V. Kunda, A. Sutono, X. Ye, D. Kim, J. Fan, 'A Comprehensive Stripeline Far-end Crosstalk Modeling Approach Based on Delta-L and Extended Unterminated Line (EUL) Crosstalk Measurement', IEEE Transactions on Electromagnetic Compatibility, to be submitted

[29] Y. Liu, S. Yong, Y. Guo, J. He, D. Kim, L. Liu, X. Ye, J. Fan, ‘Far-End Crosstalk Analysis for Stripline with Inhomogeneous Dielectric Layers (IDL)’, in *Proc. IEEE Int. Symp. EMC* 2021, to be submitted

[30] Y. Guo, S. Yong, Y. Liu, J. He, B. Pu, X. Ye, A. Sutono, V. Kunda, A. Luoh, J. Fan, D. Kim, ‘Far-End Crosstalk Control Strategy for High-volume High-Speed PCB Manufacturing: the Concept of Critical Resin Content Percent’, in *Proc. IEEE Int. Symp. EMC 2021*, to be submitted

VITA

Shaohui Yong was born in Harbin, Heilongjiang, China. He received his B.S. degree in Electrical Engineering from Beijing Jiaotong University, Beijing, China, in 2013. He joined the EMC Laboratory at Missouri University of Science and Technology (formerly, University of Missouri–Rolla), in 2015, and received his Ph. D. degree in Electrical Engineering in December 2020. His research interests included signal integrity in high-speed digital systems, electromagnetic interference, electromagnetic simulation and measurement techniques.

After the completion of his Ph. D degree program, he joined Inphi Corporation as an Electrical Engineer. Shaohui Yong received the best paper nominations from 2020 IEEE EMC & SIPI Symposium. He is also a reviewer for IEEE TRANSACTIONS ON ELECTROMAGNETIC COMPATIBILITY, IEEE MICROWAVE AND WIRELESS COMPONENTS LETTERS, and IEEE ACCES